Characterisation of the bacteriostatic and bactericidal mode of action of antibacterial proteins and compounds using Laser Scanning Confocal Microscopy

DOMINIC JONATHAN BLACK

Characterisation of the bacteriostatic and bactericidal mode of action of antibacterial proteins and compounds using Laser Scanning Confocal Microscopy

Dominic J Black

Thesis submitted for the degree of Doctor of Philosophy

Department of Chemistry
Durham University

2023

Abstract

Antibiotic resistance is an expanding global health concern requiring new and innovative approaches to prevent and treat bacterial infections. Bacteriophages and their products are one possible solution to combat these drug-resistant pathogens. The genomes of various bacteriophages have been mined for novel activities and are a rich source of proteins that have evolved to disrupt bacteria. A diverse family of such proteins, known as Kil proteins, are encoded by several *Escherichia coli* bacteriophages and appear to target the cell division apparatus, notably FtsZ which is essential for bacterial cell division. In this thesis I demonstrate that a group of structurally dissimilar Kil proteins when expressed in *E. coli* induce cell filamentation and promote cell killing. All these proteins are small in size and could be developed as peptide inhibitors that target FtsZ and other components of cell division. This thesis also examines the effect of metal chelating agents on bacterial growth and viability. Chelators are well known inhibitors of bacterial growth, but their antibacterial mechanism of action is poorly characterised. Here, a number of compounds were probed for their impact on bacterial cell morphology and potential for disrupting membrane integrity, redox chemistry and membrane potential. The results reveal that there is no single mechanism of action shared by these metal chelators but does reveal specific effects that provide fresh insights into different mechanisms of bacterial growth inhibition in addition to metal deprivation. All the proteins and compounds studied show potential as novel antibacterial agents that could be employed to treat bacterial infections.

Table of Contents

Abstract ***2***

List of Figures ***7***

List of Tables ***12***

Abbreviations ***13***

Additional Publications ***15***

Declaration ***16***

Copyright ***16***

Acknowledgements ***17***

1. Introduction ***18***

1.1. Antibiotic resistance **18**

1.2. Bacteriophages **20**

1.3. Metals and Chelants **22**

1.3.1. Metals in Microbiology 22

1.3.2. Chelating Agents 24

1.3.3. Chelants Used in the Work 25

1.3.4 EDTA 27

1.3.5. DTPMP 28

1.3.6. CHA 28

1.3.7. FA 29

1.3.8. TRO 30

1.3.9. HNK 31

1.4. Optical Microscopy **32**

1.4.1. Fluorescence Microscopy 32

1.4.2. Laser Scanning Confocal Microscopy 34

2. Materials and Methods 37

2.1. Bacteria, plasmids and chelants. 37

2.1.1. Bacterial strains 37

2.1.2. Plasmids 38

2.1.3. Chelants 39

2.2. Media 40

2.3. Bacterial culture preparation 40

2.4. Plasmid transformation 41

2.5. Bacterial viability assays 42

2.6. Plasmid subcloning 43

2.7. Fluorescent stains 43

2.8. Absorption, excitation, and emission spectroscopy 45

2.9. Microscopy 45

2.9.1. Live/Dead staining microscopy of bacteria exposed to chelants 45

2.9.2. Microscopy of plasmid transformed strains 47

2.9.3. Microscopy of λ lysogens 48

2.9.4. Size measurements and morphology of *S. aureus* mutant strains 49

2.9.5. Image analysis 50

2.10. Fluorescence Plate Reader Assays 51

2.10.1. Reactive oxygen species assay 51

2.10.2. Outer membrane integrity assay 52

3. Effects of chelants on the bacterial cell envelope 53

3.1. Introduction 53

3.1.1. Structure of the bacteria cell envelope 53

3.1.2. Assessing Outer Membrane Damage – Using NPN 55

3.1.3. Inner membrane damage – Live/Dead staining 57

3.2. Effect of EDTA on the bacterial cell envelope 60

3.3. Effect of DTPMP on the bacterial cell envelope 66

3.4. Effect of CHA on the bacterial cell envelope 71

3.5. Effect of FA on the bacterial cell envelope 77

3.6. Effect of TRO on the bacterial cell envelope 81

3.7. Effect of HNK on the bacterial cell envelope 87

3.8 Conclusions and Future Work 91

4. Effects of Chelants on the Bacterial Intracellular Redox Environment 93

4.1. Reactive Oxygen Species in Bacteria 93

4.2. Reactive Oxygen Species Detection 95

4.3. Microscopical Validation 97

4.4. Results and Discussion 100

4.4.1. Effect of EDTA on the Redox Environment inside Bacteria 101

4.4.2. Effect of DTPMP on the Redox Environment inside Bacteria 102

4.4.3. Effect of CHA on the Redox Environment inside Bacteria 104

4.4.4. Effect of FA on the Redox Environment inside Bacteria 106

4.4.5. Effect of TRO on the Redox Environment inside Bacteria 107

4.4.6. Effect of HNK on the Redox Environment inside Bacteria 108

5. Morphology of S. aureus mutants 110

5.1. Introduction 110

5.2. Isolated mutant strains 111

5.3. *S. aureus* mutant morphology analysis using LSCM 114

5.4. Discussion 126

5.4.1. Changes in cell size 126

5.4.2. Changes in cell aggregation 127

6. Secondary Lytic Bacteriophage Proteins as Antibacterial Agents 129

6.1. Bacterial Cell Division 129

6.2. Kil proteins 134

6.3. Results and Discussion 138

6.3.1. Viability assays 138

6.3.2. Effect of Bacteriophage Protein Overexpression on Bacterial Cell Morphology 140

6.3.3. Effect of FtsZ Overexpression on Bacterial Cell Morphology 140

6.3.4. Effect of Bacteriophage Mu Kil Overexpression on Bacterial Cell Morphology 144

6.3.5. Effect of Bacteriophage Rac Kil Overexpression on Bacterial Cell Morphology 146

6.3.6. Effect of Prophage Qin DicB Overexpression on Bacterial Cell Morphology 148

6.3.6. Effect of Prophage Qin YdfD Overexpression on Bacterial Cell Morphology 150

6.3.7. Effect of Bacteriophage Proteins on DNA Distribution Throughout the Cell 152

7. Ultra-high resolution 3D printing - micropatterning coverslips 160

7.1. Introduction 160

7.2. Optical Setup 165

7.3. Printing Methodology 170

7.4. Validation 172

7.5. Construction of CFP and YFP fusion plasmids 178

7.6. Conclusions and Future Work 179

8. Conclusions 181

9. References 184

List of Figures

Figure 1.1: Mechanisms by which bacteria can develop resistance to antibiotics.

Figure 1.2: The structure of a typical bacteriophage T4.

Figure 1.3: Jablonski diagram showing energy transitions during fluorescence.

Figure 1.4: Excitation and emission spectra of fluorescein in ethanol.

Figure 1.5: Schematic of a typical LSCM.

Figure 3.1: Structure of Gram-positive and Gram-negative bacterial cell envelopes.

Figure 3.2: Structure of NPN.

Figure 3.3: Emission spectrum of NPN in water and octanol.

Figure 3.4: Outer membrane integrity assay protocol timeline.

Figure 3.5: Structure of SYTO 9 and Propidium Iodide.

Figure 3.6: Excitation and emission spectra of SYTO 9 and Propidium Iodide in water with added DNA.

Figure 3.7: Inner membrane integrity assay protocol timeline.

Figure 3.8: Effect of EDTA exposure on the bacterial cell envelope.

Figure 3.9: Live/Dead staining of *E. coli* exposed to EDTA.

Figure 3.10: Live/Dead staining of *S. marcescens* exposed to EDTA.

Figure 3.11: Live/Dead staining of *S. aureus* exposed to EDTA.

Figure 3.12: Effect of DTPMP exposure on the bacterial cell envelope.

Figure 3.13: Live/Dead staining of *E. coli* exposed to DTPMP.

Figure 3.14: Live/Dead staining of *S. marcescens* exposed to DTPMP.

Figure 3.15: Live/Dead staining of *S. aureus* exposed to DTPMP.

Figure 3.16: The effect of CHA exposure on the bacterial cell envelope.

Figure 3.17: Live/Dead staining of *E. coli* exposed to CHA.

Figure 3.18: Box and whisker plot of the length of *E. coli* cells when exposed to increasing concentrations of CHA.

Figure 3.19: Live/Dead staining of *S. marcescens* exposed to CHA.

Figure 3.20: Live/Dead staining of *S. aureus* exposed to CHA.

Figure 3.21: The effect of FA exposure on the bacterial cell envelope.

Figure 3.22: Live/Dead staining of *E. coli* exposed to FA.

Figure 3.23: Live/Dead staining of *S. marcescens* exposed to FA.

Figure 3.24: Live/Dead staining of *S. aureus* exposed to FA.

Figure 3.25: The effect of TRO exposure on the bacterial cell envelope.

Figure 3.26: Live/Dead staining of *E. coli* exposed to TRO.

Figure 3.27: Box and whisker plot of the length of *E. coli* cells when exposed to increasing concentrations of TRO.

Figure 3.28: Live/Dead staining of *S. marcescens* exposed to TRO.

Figure 3.29: Live/Dead staining of *S. aureus* exposed to TRO.

Figure 3.30: The effect of HNK exposure on the bacterial cell envelope.

Figure 3.31: Live/Dead staining of *E. coli* exposed to HNK.

Figure 3.32: Live/Dead staining of *S. marcescens* exposed to HNK.

Figure 3.33: Live/Dead staining of *S. aureus* exposed to HNK.

Figure 4.1: Structure of DCFH-DA, DCFH and DCF and the steps involved to exhibit fluorescence when exposed to ROS inside cells.

Figure 4.2: Excitation and emission spectra of 2',7'-dichlorofluorescein in ethanol.

Figure 4.3: Reactive oxygen species detection assay protocol timeline.

Figure 4.4: Microscope images of control experiments of DCFH-DA as a ROS probe in *E. coli*.

Figure 4.5: Intensity profile plot of DCFH-DA assay control experiments.

Figure 4.6: Effect of EDTA exposure on the redox environment inside cells.

Figure 4.7: Effect of DTPMP exposure on the redox environment inside cells.

Figure 4.8: Effect of CHA exposure on the redox environment inside cells.

Figure 4.9: Effect of FA exposure on the redox environment inside cells.

Figure 4.10: Effect of TRO exposure on the redox environment inside cells.

Figure 4.11: Effect of HNK exposure on the redox environment inside cells.

Figure 5.1: Mutations present in the eight chelant resistant mutant *S. aureus* strains.

Figure 5.2: Excitation and emission spectra of Hoechst 33342 in water.

Figure 5.3: Wild type *S. aureus* stained with Hoechst 33342.

Figure 5.4: *S. aureus* mutant strains obtained from exposure to EDTA stained with Hoechst 33342.

Figure 5.5: *S. aureus* mutant strains obtained from exposure to DTPMP stained with Hoechst 33342.

Figure 5.6: Box and whisker plot of size measurements of *S. aureus* mutant strains.

Figure 5.7: Tile scan images of *S. aureus* wild type and mutant strains obtained from exposure to DTPMP stained with Hoechst 33342.

Figure 5.8: Tile scan images of *S. aureus* wild type and mutant strains obtained from exposure to EDTA stained with Hoechst 33342.

Figure 5.9: Standardised micrometer.

Figure 5.10: Intensity plot of top pixel row of micrometer.

Figure 6.1: Crystal structures of FtsZ.

Figure 6.2: Formation of the FtsZ dividing ring by polymerisation of FtsZ monomers into filaments and subsequent bundles.

Figure 6.3: Treadmilling action of the FtsZ ring to constrict the cell and form the new septum from peptidoglycan.

Figure 6.4: Predicted structures of bacteriophage secondary lytic proteins.

Figure 6.5: Viability assays of transformed *E. coli* BL21-AI.

Figure 6.7: Live/Dead staining of *E. coli* BL21-AI transformed with pET plasmids.

Figure 6.8: Live/Dead staining of *E. coli* BL21-AI transformed with pET16b-FtsZ.

Figure 6.9: Live/Dead staining of *E. coli* BL21-AI transformed with pET16b-Mu Kil.

Figure 6.10: Live/Dead staining of *E. coli* BL21-AI transformed with pET16b-Rac Kil.

Figure 6.11: Live/Dead staining of *E. coli* BL21-AI transformed with pET16b-Qin DicB.

Figure 6.12: Live/Dead staining of *E. coli* BL21-AI transformed with pET16b-Qin YdfD.

Figure 6.13: DNA distribution throughout static and dividing *E. coli* BL21-AI cells.

Figure 6.14: DNA distribution throughout pathogenic *E. coli* BL21-AI cells overexpressing phage Rac Kil.

Figure 6.15: DNA distribution throughout pathogenic *E. coli* BL21-AI cells overexpressing prophage Qin DicB.

Figure 6.16: DNA distribution throughout pathogenic *E. coli* BL21-AI cells overexpressing prophage Qin YdfD.

Figure 7.1: The spectral principle of FRET.

Figure 7.2: Jablonski diagram of FRET.

Figure 7.3: The effect of bacterial orientation on the quality of image produced.

Figure 7.4: Left, principle of selective curing of UV curable resin using spatially patterned light.

Figure 7.5: Pre microscope optical setup of printing setup.

Figure 7.6: Internal microscope setup for printing apparatus.

Figure 7.7: Photograph of printing apparatus with fibre on the left and microscope on the right.

Figure 7.8: SLM used to generate patterned light.

Figure 7.9: Principle of operation of the SLM to generate patterned light.

Figure 7.10: Images projected for micropatterning coverslips, and transmission microscopy of the resulting scaffolds generated.

Figure 7.11: Excitation and emission spectra of Rhodamine 6G in ethanol.

Figure 7.12: Printed scaffold with Rhodamine 6G included in the resin.

Figure 7.13: Printed scaffold with Rhodamine 6G added to LB media.

Figure 7.14: Printed scaffold with Rhodamine 6G added to resin and DAPI-stained E. coli BL21-AI added.

Figure 7.15: 3D projection of DAPI stained *E. coli* BL21-AI impregnated into printed scaffold.

List of Tables

Table 1.1: Chemical structure of all chelants used in this work.

Table 2.1: Bacterial strains used in this study.

Table 2.2: Bacterial plasmids used in this study.

Table 2.3: Chelating agents used in this study.

Table 2.4: Fluorescent stains used in this study.

Table 5.1: Chelant resistant mutant strains of S. aureus and the conditions used to generate them.

Table 5.2: Statistical data from size measurements of S. aureus mutant strains.

Table 5.3: Determination of pixel size of the microscope system.

Table 6.1: Amino acid sequence of FtsZ and lytic phage proteins.

Table 6.2: Plasmids used to transform BL21-AI E. coli into phage protein expressing strains and control strains with no genes inserted and endogenous ftsZ inserted.

Abbreviations

Ap	Ampicilin
CFP	Cyan Fluorescent Protein
CHA	N-hydroxyoctanamide
CL	Collimating Lens
CryoTEM	Transmission electron cryomicroscopy
DAPI	2-(4-Amidinophenyl)-1H-indole-6-carboxamidine
DCF	2',7'-Dichlorofluorescein
DCFH	2',7'-Dichlorofluorescin
DCFH-DA	2',7'-Dichlorofluorescin diacetate
$DiOC_2(3)$	3,3'-Diethyloxacarbocyanine
DTPMP	[bis[2-[bis(phosphonomethyl) amino]ethyl]amino] methylphosphonic acid
EDTA	2-[2-[bis(carboxymethyl) amino]ethyl-(carboxymethyl) amino]acetic acid
FA	5-butylpyridine-2-carboxylic acid
FnBPA	Fibronectin-binding Protein A
FRET	Förster Resonance Energy Transfer
GFP	Green Fluorescent Protein
H_2O_2	Hydrogen Peroxide
HeNe	Helium-Neon
HNK	2-hydroxy-6-propan-2-ylcyclohepta-2,4,6-trien-1-one

Hoechst 33342	2-(4-ethoxyphenyl)-6-[6-(4-methylpiperazin-1-yl)-1H-benzimidazol-2-yl]-1H-benzimidazole;trihydrochloride
HyD	Hybrid Detector
IPTG	Isopropyl β-d-1-thiogalactopyranoside
kb	kilobases
Km	Kanamycin
LB	Lysogeny Broth
LP	Linear Polariser
LSCM	Laser Scanning Confocal Microscopy
MIC	Minimum Inhibitory Concentration
PBS	Phosphate Buffered Saline
PI	Propidium Iodide
PMT	Photomultiplier Tube
ROS	Reactive Oxygen Species
SLM	Spatial Light Modulator
TEM	Transmission Electron Microscopy
TL	Tube Lens
TRO	2-hydroxycyclohepta-2,4,6-trien-1-one
wt	Wild Type
YFP	Yellow Fluorescent Protein

Additional Publications

Additional experimental data was collected over the course of this PhD which was not included in this thesis as the topics were unrelated. This additional work was incorporated in the following publications:

1. Smith, P. O., Black D. J., Pal, R., Avó, J., Dias, F. B., Linthwaite, V. L., Cann, M. J. & Pållson L.-O. Applying TADF Emitters in Bioimaging and Sensing—A Novel Approach Using Liposomes for Encapsulation and Cellular Uptake. *Front Chem* **9**, (2021).
2. De Rosa, D. F., Stachelek, P., Black, D. J. & Pal, R. Rapid handheld time-resolved circularly polarised luminescence photography camera for life and material sciences. *Nat Commun* **14**, 1537 (2023).

Results either wholly or partially derived from this thesis are incorporated in the following manuscripts being prepared for submission:

1. Enhanced tolerance of metal sequestering agents by reconfiguration of the Staphylococcus aureus cell wall.
2. Antibacterial mode of action of metal sequestering agents against Gram-negative and Gram-positive bacteria.
3. Different antibacterial mechanisms of tropolone and hinokitiol against Gram-negative and Gram-positive bacteria.
4. Biocompatible printing of microstructures to control alignment of bacteria using 3D structured illumination microscopy.

Declaration

The work described herein was undertaken at the Department of Chemistry, Durham University, between April 2019 and December 2022. All of the work is my own, except where specifically stated otherwise. No part has previously been submitted for a degree at this or any other university.

Copyright

Acknowledgements

This work would not have been possible without the immense support of my two supervisors Professor Robert Pal and Dr Gary Sharples. I couldn't have asked for more supportive supervisors and I will forever be indebted to you both. And to Rob, thank you for giving me the opportunity to work with (and annoy) you for another three years.

Thank you to all the members of the Sharples and Pal group, and especially to the people who have had the pleasure of sharing an office with me throughout my time here: Kathleen, Tom, Davide, Lewis, Patrycja, Artemijs and countless fourth years, it's been an honour to serve with you!

Even though you've never understood anything I've been talking about, thank you to my family for encouraging and supporting me through my PhD. Mam, Dad, Grandma, Grandad, Gran, Grandad, David, Melissa, John, Debbie, Susan, Alice, Zoe, Jonathan and Paul, I will continue to annoy you all talking about science.

Last but certainly not least I could not have got through this without the person who has constantly supported me through the highs and lows of this chapter of my life, my darling husband, Thomas. You, along with Roxy have been my rock and I couldn't have done this without you!

1. Introduction

1.1. Antibiotic resistance

Prior to the introduction of antibiotics, an infection could often prove fatal or lead to serious illness. In the 1940s the use of penicillin[1] and streptomycin[2] became widespread in medicine and a bacterial infection was no longer regarded as a potential death sentence but was a treatable medical condition. However, as antibiotics were deployed more commonly, bacteria began to evolve resistance mechanisms, which could be rapidly disseminated among bacterial populations. Strains of pathogenic bacteria now exist which are resistant to a wide range of antibiotics meaning an infection caused by these bacteria can be challenging to treat. In 2015 over 670,000 deaths in the EU and EEA (European Economic Area) were caused by antibiotic resistant infections.[3] This problem is only expected to get worse as more antibiotics are used and bacteria continue to develop resistance. Although new antibiotics are being discovered, there have been no new classes of antibiotics discovered since the 1960s[4] and it is likely that if a bacterium develops resistance to one antibiotic it will eventually develop resistance to every antibiotic in its class.

Current research to find new antibiotics is focussing on sources that haven't been looked at before with a hope of finding new classes of antibiotics to keep a step ahead of antibiotic resistance.[5] The two areas this thesis will focus on are bacteriophages which are viruses that can infect bacteria and chelants which are metal binding compounds which have been shown to have both bactericidal and bacteriostatic effects.

Bacteria can evolve resistance to antibiotics through a range of mechanisms. Mutation can arise by mistakes made during the DNA replication that frequently modify the gene products targeted by the antibiotic to prevent inhibition. Figure 1.1 illustrates the various mechanisms by which a bacterium may develop resistance to an antibiotic.[6] They could upregulate production of an enzyme that degrades the antibiotic, use alternate enzymes to the antibiotic target enzyme which accomplishes the same outcome so the antibiotic won't affect the bacteria anymore or the bacteria can reduce the amount of antibiotic in the cytoplasm by removing it from the cell or stopping it enter through the membrane into the cell. This is not an active process where bacteria actively seek resistance to antibiotics but is a passive process which only occurs when a beneficial mutation occurs. The resistant bacteria will pass on the resistance to daughter cells or they can pass the gene on as well.[7]

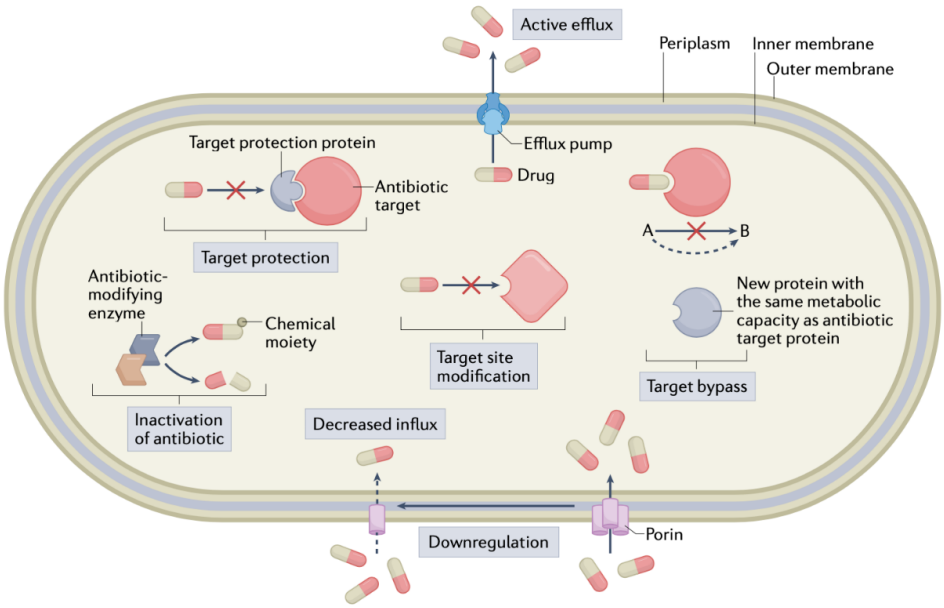

Figure 1.1: Mechanisms by which bacteria can develop resistance to antibiotics.[6]

1.2. Bacteriophages

Bacteriophages, frequently abbreviated to phages, are viruses which infect and reproduce inside bacteria or archaea by injecting their genetic material into the cytoplasm of the cell in a similar way that viruses that infect eukaryotic cells do. As viruses, they cannot reproduce on their own and must hijack the reproductive capabilities of a living organism, in this case bacteria or archaea. They are comprised of either a DNA or RNA genome encapsulated in proteins. They usually have additional protein apparatus which facilitate entry into the bacteria.[8] Figure 1.2 shows the atomic level structure and a schematic of a typical bacteriophage, T4.[9]

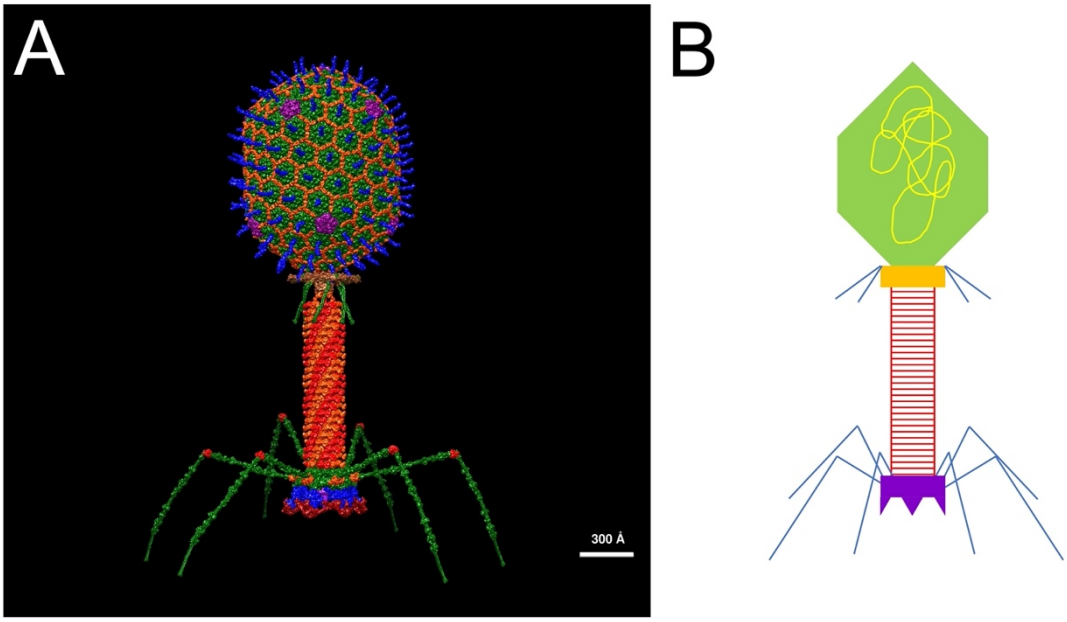

Figure 1.2: The structure of a typical bacteriophage T4. A, atomic resolution structure of Escherichia virus T4.[9] *B, schematic of T4 where green: head, yellow: genome, orange: collar, red: tail, purple: base plate, blue: tail fibres.*

Bacteriophages are the most genetically diverse lifeforms on the planet, they are found anywhere that bacteria or archaea are found. Their genome can vary hugely,

ranging from the smallest of any lifeform, 4 genes,[10] to hundreds of genes in the largest known with a genome length of 735 kb.[11] Nineteen families are currently recognized by the International Committee on Taxonomy of Viruses that infect bacteria and archaea. Of these, only two have RNA genomes, and only five families are surrounded by an envelope. Of the viral families with DNA genomes, only two have single-stranded genomes. Eight of the viral families with DNA genomes have circular genomes, while nine have linear genomes. Nine families infect bacteria only, nine infect archaea only, and one (Tectiviridae) infects both bacteria and archaea.[12] They are most abundant in seawater where it is estimated that 70% of marine bacteria are infected with a bacteriophage.[13]

Bacteriophages reproduce by either a lytic or lysogenic cycle, with some phages being capable of both reproduction methods. For phages which reproduce via the lytic cycle the infected bacterium breaks open, lyses, once the phage has been replicated. The phage injects its genetic material into the cell, hijacks the reproduction apparatus of the bacterium and replicates itself many times then causes the cell to lyse. Some lytic phages can delay lysis if the concentration of phages outside the cell is high until the concentration has lowered to increase the chance of the new phages finding a new host to infect.[14]

Phages which reproduce via the lysogenic cycle do not lyse the cell immediately following reproduction. The viral DNA can integrate into the bacterial genome and become a prophage. The phage DNA is then replicated with the bacterial chromosome causing no harm to the bacterium. This allows the prophage to be copied into many cells as each daughter cell formed from the original infected cell

will contain the phage DNA. The prophage remains dormant until the condition of the bacterium deteriorates, for instance if the concentration of available nutrients drops or the cell is damaged. The prophage then becomes active and starts to reproduce making new virions which lyse the cell once a critical concertation of virions inside the cell is reached.[14]

The proteomes of many different phages are poorly characterised, even in the most intensively researched phages. Many proteins encoded by these genomes have yet to be assigned a function, notably those involved in manipulation of the host metabolism. Some may be relics of genetic rearrangements which are non-functional, although frequently new functionalities can emerge from the fusion of different domains. Regardless, bacteriophages through evolutionary history have become adept at manipulating and killing their bacterial hosts and therefore provide a rich source of products that have antibacterial properties.

1.3. Metals and Chelants

1.3.1. Metals in Microbiology

Metals are required by all forms of life in varying quantities, from trace levels to significantly higher concentrations, and have to be maintained at appropriate levels to avoid insufficiency or the toxic consequences of excess.[15] Transition metal ions are essential as cofactors for metalloenzymes carrying out the core cellular and metabolic functions, including respiration, energy generation and growth.[16] About one-third of all proteins and half of all enzymes utilise a metal ion as a cofactor[17] so

both eukaryotes and prokaryotes have developed methods for uptake and storage of metal ions. Metalloproteins are a class of proteins that require a metal ion to function correctly, and they include metalloenzymes, storage proteins, and transcription factors. The first-row late d-block transition metals, including manganese (Mn), iron (Fe), cobalt (Co), nickel (Ni), copper (Cu) and zinc (Zn), are specific cofactors found within active sites of metalloenzymes. These cations can activate substrates, due to their Lewis acidity.[18] The metal can coordinate to the substrate and pull electron density away from the ligand, inducing polarisation. The electrostatic properties of transition metals allow them to stabilize substrates or reaction intermediates by facilitating redox reactions.[19] These metals, except Zn, have unfilled d-orbitals and thus are redox active, allowing them to lose or gain electrons easily, switching oxidation states. Redox active metal ions can be directly involved in the reaction or involved in electron transfer to and from the active site. This contributes to their catalytic properties and toxicity.[19] Zn is the most common non-redox transition metal used in structural and catalytic roles. Approximately 80% of enzymes consist of the Zn-containing proteins within archaea and bacteria and 4-8% of proteins encoded in genomes of bacteria and archaea are Zn(II) binding proteins.[18]

The ability to take part in redox reactions, a defining trait of transition metal elements, can also cause harm to organisms. Metals of the same oxidation state can be incorporated into metalloproteins rendering them non-functional.[20] Similarly the redox potential of transition metal elements can cause unwanted reactions to occur. For example, the Fenton reaction[21] causes significant damage to the cell if the concentration of iron becomes too high. Iron in its soluble ferrous form, Fe(II), can

interact with peroxide to form hydroxyl radicals.[22] These radicals are strong oxidisers and can damage every component of a cell including its structural proteins, DNA and lipids. It is therefore essential that metal concentrations are managed appropriately and that metalloproteins can obtain the correct metal from a limited and tightly restricted pool. Organisms must be able to regulate their intracellular metal levels to fulfil physiological needs without coming to harm through toxic metal overload.

1.3.2. Chelating Agents

Chelating agents are molecules that have two or more donor atoms which can simultaneously form coordinate bonds with a single central metal ion to form a stable complex. Chelants bind with a greater affinity compared to monodentate ligands such as water, halogens, and other inorganic ligands such as ammonia. They have greater binding constants, K_b, and stability constants, β, due to the chelate effect which occurs due to a reduction in the Gibbs' free energy, G, for the metal binding to a chelant compared with other ligands. Binding of a chelating ligand increases entropy through the release of monodentate ligands through ligand exchange. This reduces G which makes chelation more favourable thermodynamically as shown in Equation 1.1. Equation 2.1 relates the equilibrium constant to Gibbs free energy to the binding constant of a ligand. As ΔG is more negative for the binding of a ligand, K_b will be greater for that reaction so more chelant will be bound than monodentate ligands.

$$\Delta G = \Delta H - T\Delta S \qquad \text{Equation 1.1}$$

$$\Delta G = -RTlnK_b \qquad \text{Equation 1.2}$$

Hence, if enough chelant is available, the majority of metal ions will be bound to chelants rather than monodentate ligands such as water, as metal ions are when in aqueous solution.

Chelating agents are used commercially to inhibit bacterial growth in various industries such as in healthcare, cleaning products and cosmetics. The antibacterial mechanisms of action are only partially understood.[23] The most likely mechanism is via the formation of metal ion complexes that starve bacteria of these essential micronutrients, thus inhibiting growth. These metal-binding compounds can work on their own or synergistically with antibiotics improving their efficacy.[24] They can also potentiate some antibiotics, even against strains that are otherwise antibiotic resistant. Mechanisms of antibiotic drugs include interference with cell wall synthesis, disruption of bacterial membrane structure, inhibition of synthesis of proteins and nucleic acids and inhibition of metabolic pathways[25] and the mechanism of action of chelants may mirror some of these. The modes of action of the majority chelating agents in bacterial growth inhibition and their selectivity in metal deprivation *in cellulo* remain ill-defined.

1.3.3. Chelants Used in the Work

Table 1.1 shows the structure of the chelants studied in this work, details of the full chemical name and CAS number of each chelant can be found in the Materials and Methods section.

Chelant	Structure
EDTA	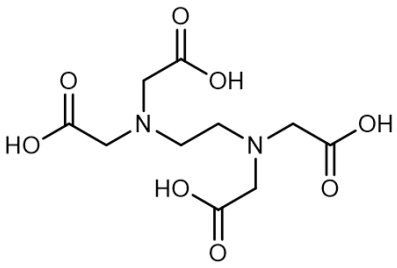
DTPMP	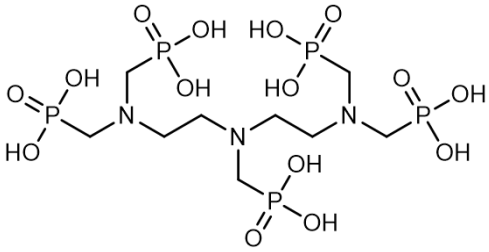
CHA	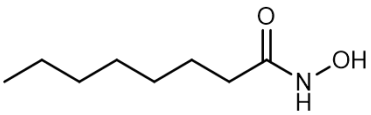
Fusaric acid (FA)	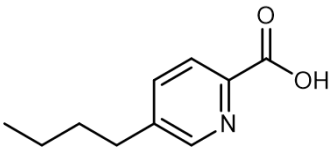
Tropolone (TRO)	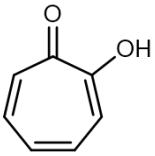
Hinokitiol (HNK)	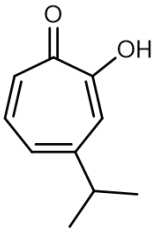

Table 1.1: Chemical structure of all chelants used in this work.

1.3.4 EDTA

EDTA is a synthetic chelator which can bind to a broad range of metals.[26] It is a hexadentate ligand which is able to form octahedral complexes with metal ions via four carboxylate and two tertiary amine groups. This aminocarboxylate is used widely in chelation therapy to prevent heavy metal poisoning, cosmetics, cleaning products and also food products as a preservative. Previous work has suggested that EDTA exerts its antimicrobial effect by inducing membrane permeabilisation through sequestration of Ca(II) and Mg(II),[27] although the precise metals involved have not been identified. Cell envelope cations likely form electrostatic cross-links between the negatively charged sugar groups present on lipopolysaccharides and are thus essential for the integrity of the bacterial outer membrane of Gram-negative bacteria. Hence, exposure of bacterial cells with EDTA leaves them vulnerable to osmotic changes and the entry and subsequent action of other antimicrobials. Recent work has shown that the efficacy of antibiotics ciprofloxacin, ampicillin, and gentamicin in *Pseudomonas aeruginosa* have been enhanced when used in conjunction with EDTA.[28] EDTA has also been shown to disrupt the biofilm formation in Gram-positive bacteria such as methicillin-resistant Staphylococcus aureus (MRSA) and make these resistant strains more susceptible to antibiotic treatment.[29]

The hydrophilic nature of this chelant implies that EDTA should act extracellularly and form complexes with metal ions prior to their uptake by cells.[30] However, it has been determined that other factors besides LPS disruption also contribute to the antibacterial effect of EDTA.[31] Experiments with *E. coli* have shown that EDTA is

predominantly responsible for sequestering Mn(II), but also decreases concentrations of Fe(III) and Zn(II).[32,33]

1.3.5. DTPMP

DTPMP is a synthetic nitrogenous polyphosphonic acid. It is widely used in household and industrial cleaning products, oilfield scale inhibition and in the treatment of wastewater.[34,35] DTPMP can bind to a number of cations.[36] Although there are many possible donor atoms in a molecule of DTPMP, this ligand is hexadentate, using three tertiary amine groups and three phosphate groups to form octahedral complexes with metal cations, although other complex structures have also been observed.[37] As DTPMP is a hydrophilic molecule, it is expected that this chelant sequesters metals from the extracellular environment.[30]

1.3.6. CHA

CHA forms part of a larger subset of molecules, hydroxamic acids, which are naturally occurring metabolites of bacteria, fungi, and plants. The use of hydroxamic acids as defensive secondary metabolites in plants[38] can be explained by their chelating activity. CHA is commonly used as a preservative in beauty products. CHA contains a hydroxamate unit which is well-known for binding to Fe(III),[32] as seen in siderophores produced by bacteria, such as desferrioxamine, to assist iron acquisition. It is expected that this hydroxamate unit acts as a bidentate ligand and chelates Fe(III) via the presence of its two oxygen atoms, as seen in the siderophore desferrioxamine.[39] Previous work has suggested that CHA shows no significant effect on the cellular

metal composition of *E. coli* cells.[23] The localization of CHA in bacterial cells has yet to be elucidated, although it is suggested that the hydrophobic portion of the molecule is able to insert into the outer membrane and allow the hydrophilic portion of the molecule to trap essential metals at the bacterial cell surface.[33]

In comparison to other chelants investigated in this work, CHA has a relatively low efficacy across all bacterial species studied (J.R. Paterson, unpublished results). As hydroxamic acids are common bacterial metabolites, the low efficacy of CHA could be due to the presence of degradation pathways to eliminate this molecule. Higher concentrations of this chelant may therefore be required to saturate these degradation pathways and lead to the antimicrobial effects of this chelant.

1.3.7. FA

Fusaric acid (FA) is a mycotoxin, a defensive secondary metabolite naturally produced by fungi and is known to have neurotoxic, antibacterial, and phytotoxic effects.[40–42] FA is a derivative of picolinic acid and therefore is most likely to act as a bidentate ligand, using the nitrogen on the pyridine ring and the carboxylate group to form complexes with cations.[43] FA has been proposed as a potential herbicide in agriculture but is predominantly used as a research tool, such as in the genetic engineering of plants resistant to FA mycotoxin absorption.[44] FA is able to bind a number of cations, of which Fe(III) shows the highest affinity.[45] It has been shown that iron chelation is the main antibacterial effect of FA in *Pseudomonas protegens* and that this molecule acts extracellularly sequestering metal ions from the

medium.[45] The antibacterial effects of FA on Gram-negative and Gram-positive bacteria has been studied, with the latter showing greater susceptibility.[28]

1.3.8. TRO

Tropones and tropolones are non-benzenoid seven-membered aromatic compounds with a carbonyl group. Many tropolone derivatives with a diverse range of biological activities, including bactericidal activity,[46] are produced by plants and fungi as natural products. TRO also displays antioxidant activity[47] and is therefore often used in household products and cosmetic and pharmaceutical formulations. Tropolone uses its two exocyclic oxygen donor atoms to bind to metals and therefore acts as a bidentate ligand.[48] Previous work has indicated that tropolone is able to form stable complexes with a variety of metal ions, of which complexation with Cu(II) shows the highest stability.[49] TRO triggers a minor reduction in the cellular concentrations of a number of metals in *P. aeruginosa*, despite most other chelants having a greater effect on a smaller number of metals.[33] Transcriptional analysis of *E. coli* treated with TRO, revealed elevated expression of genes involved in iron uptake, suggesting cells are selectively starved of this metal.[50] TRO has been identified as an inhibitor of several metalloproteins, including *P. aeruginosa* elastase (LasB) which uses a Zn(II) cofactor[51] and a capsular polysaccharide biosynthetic enzyme (CapF) in *S. aureus*.[52] It seems likely that the antimicrobial effect of tropolone and its derivatives occurs by a combination of iron starvation and inhibition of selective bacterial metalloenzymes.

1.3.9. HNK

Hinokitiol (HNK) is a natural chelant which acts as defensive secondary metabolite in plants and is known to have broad antimicrobial, antifungal, antiparasitic and antiviral properties.[46,53,54] HNK has been shown to have bactericidal efficacy against both Gram-positive and Gram-negative species.[55] HNK is commonly used in cosmetic and food products due to its antimicrobial properties. HNK, as a tropolone derivative, is also able to bind to a variety of different metal ions, of which Cu(II) shows the highest stability.[49] HNK and tropolone (TRO) share the main tropone moiety and hydroxy group at the 2-position, but HNK has an additional isopropyl group at the 4-position. HNK must therefore act as a bidentate ligand, using its two oxygen donor atoms to bind metals. The presence of the isopropyl group on the HNK molecule changes the properties of this bidentate ligand and the resulting complexes formed from HNK with respect to the tropolone ligand; dimeric structures and polymorphs have been observed for HNK metal complexes.[56] Additionally, the presence of the isopropyl group at the 4-position makes these two oxygen donors inequivalent, resulting in the formation of geometrical and optimal isomers for bis and tris-HNK complexes.[56]

1.4. Optical Microscopy

1.4.1. Fluorescence Microscopy

The word microscope was coined in 1625 by Giovanni Faber to describe rudimentary devices that consisted of two lenses – an objective lens and an eyepiece lens – that had been invented from the late 16th century onwards.[57] These simple microscopes were not used to publish any scientific observations until 1665 when Robert Hooke released Micrographia[58] and the field of microscopy became an integral component of the natural sciences.

The fundamental design of optical microscopes has changed little much but new techniques have been developed to allow for a greater resolution to be achieved and the visualisation of microscopic components that are otherwise invisible. Possibly the greatest advancement in microscopy was the development of fluorescence microscopy in the mid-20th century. Figure 1.3 shows the principle of excitation and emission in fluorescence. Most molecules are capable of undergoing excitation by a photon of light to a higher electronic energy level. Once in this excited state the energy needs to be released. Some molecules do this by non-radiative decay where the energy is lost as heat, but fluorophores lose this excess energy by radiative decay: they emit a photon of light. This emitted photon has a lower energy than the one absorbed because some of the energy absorbed is lost vibrationally. The emitted photon will, therefore, have a longer wavelength than the absorbed photon. The difference between the excitation and emission wavelengths is called a Stokes' shift as depicted in figure 1.4.

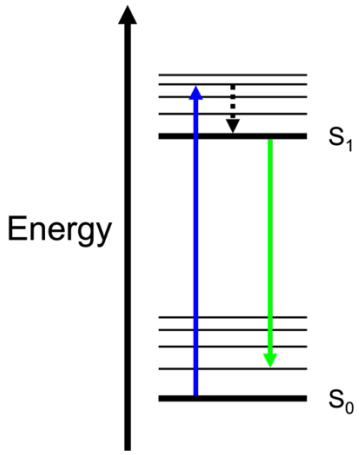

Figure 1.3: Jablonski diagram showing energy transitions during fluorescence. Upon excitation (blue line) by absorption of a photon the fluorophore moves to an excited singlet state. The fluorophore undergoes internal relaxation until it is in its lowest vibrational energy level of the excited singlet state. The fluorophore can then relax to its ground state by emitting a photon.

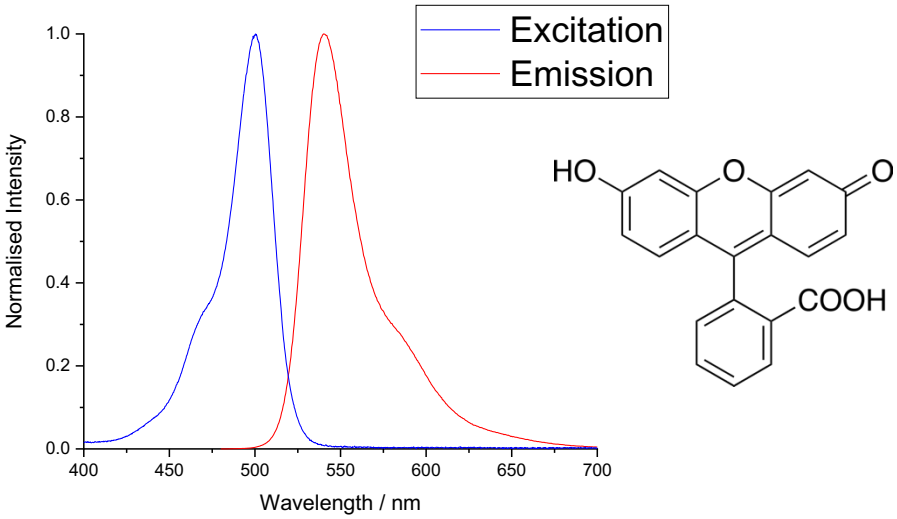

Figure 1.4: Excitation and emission spectra of fluorescein in ethanol. Structure of fluorescein shown on the right.

Most biological systems have a low inherent fluorescence so lend themselves well to fluorescence microscopy with stains being designed to target specific parts of cells to

visualise intracellular structures. Since every fluorophore has a unique excitation and emission profile it is possible to use multiple fluorophores simultaneously to visualise different components of the cell. To achieve this, each fluorophore is excited by a specific wavelength generated using band-pass filters or a laser. The signals from the different fluorophores are separated using a combination of long-pass filters and dichroic mirrors assuming the excitation and emission spectra are separated sufficiently do no energy transfer can occur between the fluorophores involved.

1.4.2. Laser Scanning Confocal Microscopy

Where fluorescence microscopy was a major improvement on transmission microscopy, laser scanning confocal microscopy (LSCM) was a major advancement in fluorescence microscopy. A significant drawback in fluorescence microscopy is the lack of optical sectioning. Fluorescence microscopy illuminates the whole specimen that is being visualised at one frame and although only the plane in focus can be seen clearly emitted light from the whole specimen travels to the detector resulting in a considerable background signal and poor signal-to-noise ratio. First described in 1961, the principle of confocal microscopy adds a pinhole to remove this obstacle and allow for improved optical sectioning.[59]

Figure 1.5 shows a schematic of a typical LSCM setup. LSCM generates an image by using a single point detector to measure the intensity of each pixel in the image sequentially rather than generating the whole image on a detector at once such as with a camera

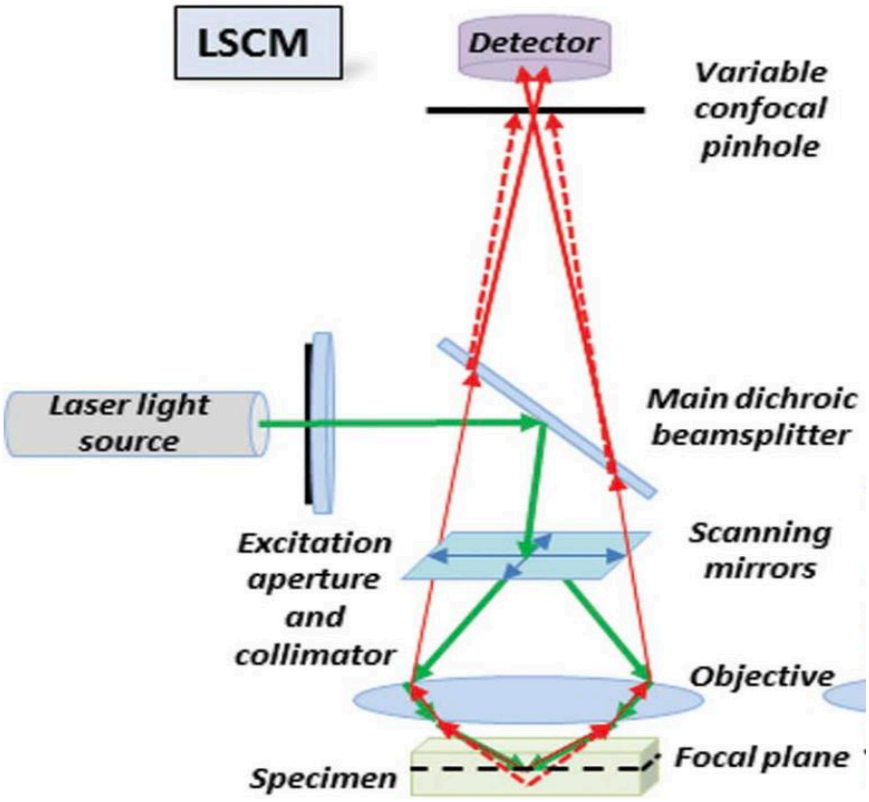

Figure 1.5: Schematic of a typical LSCM.[60]

. A pair of synchronised galvanometric mirrors (X,Y) raster scans a diffraction-limited spot across the region of interest. In the first confocal microscopes an incoherent light source, such as an arc lamp, was used to provide the illumination. In modern systems, the excitation source used is a coherent laser to provide very narrow excitation bandwidths, allowing highly selective fluorescent excitation. The light collected from the excitation spot is collected through the objective lens and the signal is recorded using a pointillistic detector. The detectors used may be a photomultiplier tube (PMT), avalanche photodiode (APD) or a combination of the two as a hybrid detector (HyD). The confocality of LSCM comes from the use of a pinhole in the detection arm of the optical pathway to provide improved optical sectioning. Light gathered from the illuminated pixel is focused to a point after the

galvo-scan mirrors. Only light from the focal plane of the objective will focus through the pinhole, excluding light from outside the focal plane. This means that the pixel imaged represents a 3D volume (voxel), making each image equivalent to a thin section through the sample. By acquiring many images at different known axial (Z) heights, 3D maps of the structures can be reconstructed from the stacks of images.

2. Materials and Methods

Throughout this work asterisks are used to indicate statistical significance of differences in data. To determine the significance of any differences one way analysis of variance (ANOVA) was used. *, $P \leq 0.05$ **, $P \leq 0.01$; ***, $P \leq 0.001$; ****, $P \leq 0.0001$.

2.1. Bacteria, plasmids and chelants.

2.1.1. Bacterial strains

Bacterial strains used in this study are listed in table 2.1 below

Species	**Strain**	**Genotype**
Escherichia coli	BW25113, CGSC7636 (wild-type K-12)	*lacI$^+$ rrnBT14 ΔlacZWJ16 hsdR514 ΔaraBADAH33 ΔrhaBADLD78 rph-1 Δ(araB–D)567 Δ(rhaD–B)568 ΔlacZ4787(::rrnB-3) hsdR514 rph-1*.
	DH5α	F$^-$ ϕ80*lac*ZΔM15 Δ(*lac*ZYA-*arg*F)U169 *rec*A1 *end*A1 *hsd*R17(r_K^-, m_K^+) *pho*A *sup*E44 λ$^-$*thi*-1 *gyr*A96 *rel*A1
	BL21-AI (B strain)	*F$^-$ ompT gal dcm lon hsdSB(rB$^-$ mB$^-$) [malB$^+$]K-12(λS) araB::T7RNAP-tetA*
	MG1655 (wild-type K-12)	□$^-$ *ilvG rfb-50 rph-1*
	LT445	MG1655 (λ) monolysogen
	LT447	MG1655 (λ *cI857 ind1*) monolysogen
	LT2166	MG1655 (λ *ΔninH*) monolysogen

	LT2230	MG1655 (λ *cI857 ind1 ΔninH*) monolysogen
	LT2258	MG1655 *fis*::*cat*
	LT2259	LT447 *fis*::*cat*
	LT2260	LT2230 *fis*::*cat*
Pseudomonas aeruginosa	NCTC10662, ATCC25668	Schroeter, Migula; originally a clinical isolate
Serratia marcescens		
Staphylococcus aureus	FDA209P, ATCC6538P	Reference methicillin-sensitive *S. aureus* (MSSA) wild-type strain
	FDA209P EDTA-selected strains	JN170, JN206, JN207
	FDA209P DTPMP-selected strains	JN174, JN208, JN209, JN210, JN212

Table 2.1: Bacterial strains used in this study. LT strains were obtained from Lynn Thomason, National Institutes of Health, Frederick, Maryland.

2.1.2. Plasmids

Plasmids used in this study are detailed in table 2.2. All plasmid constructs were synthesised by Genscript.

Plasmid name	Plasmid Details	Gene length / bp
pMu-Kil	Phage Mu *kil* inserted into pET28a(+) using NdeI and BamHI sites	234
pRac-Kil	Prophage Rac *kil* inserted into pET28a(+) using NdeI and BamHI sites	231
pQin-DicB	Prophage Qin *dicB* inserted into pET28a(+) using NdeI and BamHI sites	198
pQin-YdfD	Prophage Qin *ydfD* inserted into pET28a(+)	201

	using NdeI and BamHI sites	
pP22-Kil	Phage P22 *kil* inserted into pET28a(+) using NdeI and BamHI sites	198
pλ-Kil	Phage λ *kil* inserted into pET22b(+) using NdeI and BamHI sites	279
pFC201	pLAU17 *cfp* inserted into pET22b(+) using XbaI and NdeI sites	780
pFC209	pLAU18 *yfp* inserted into pET22b(+) using XbaI and NdeI sites	780
pFtsZ	*E. coli ftsZ* inserted into pET16b using NdeI and BamHI sites	1161
pET22b(+)	T7 expression vector. Ampicillin (Ap) resistant.	
pET28a(+)	T7 expression vector. Kanamycin (Km) resistant.	
pET16b	T7 expression vector. Ampicillin (Ap) resistant.	

Table 2.2: Bacterial plasmids used in this study.

2.1.3. Chelants

All chelating agents used in this study are listed in Table 2.3 and include the relevant solvent used in each case. Chelant stocks were sterilised by filtration through a 0.2 µm filter (Fisher Scientific, 15206869).

Synonym	IUPAC Name	CAS Number	Source	Solvent
CHA	*N*-hydroxyoctanamide	7377-03-9	Fluorochem, 227638	DMSO
DTPMP	[bis[2-[bis(phosphonomethyl) amino]ethyl]amino] methylphosphonic acid	15827-60-8	Sigma Aldrich, 36818	N/A
EDTA	2-[2-[bis(carboxymethyl) amino]ethyl-(carboxymethyl) amino]acetic acid	60-00-4	Melford, E58100	Water
FA	5-butylpyridine-2-carboxylic acid	536-69-6	Sigma Aldrich, 55952	DMSO
HNK	2-hydroxy-6-propan-2-ylcyclohepta-2,4,6-trien-1-one	499-44-5	Sigma Aldrich, 469521	DMSO
TRO	2-hydroxycyclohepta-2,4,6-trien-1-one	533-75-5	Sigma Aldrich, T89702	DMSO

Table 2.3: Chelating agents used in this study.

2.2. Media

All bacteria were grown in lysogeny broth (LB Lennox), either on agar plates (Sigma Aldrich, L7533) or in liquid media (Sigma Aldrich, L3022). Media was made up using deionised water obtained from a Milli-Q® Integral 15, Merck Millipore water filtration system and sterilised at 121˚C for 15 min at 15 psi in a Dixons Vario 1528 autoclave.

2.3. Bacterial culture preparation

Bacterial cultures were prepared fresh from frozen stocks after streaking to single colonies on LB agar plates using a sterile plastic loop (Sarstedt, 86.1562.010). Plates

were incubated at 30 °C or 37 °C overnight in a static incubator (Carbolite, PIF120) and refrigerated for later use. Plates were kept for a maximum of three weeks. To make overnight cultures a single colony was picked using a sterile plastic loop and inoculated 5 mL of LB in a 15 mL screw cap Falcon tube (Sarstedt, 62.554.502) and incubated overnight at 37 °C in a shaking incubator (SciQuip, SQ-4010). Overnight cultures were kept for a maximum of one week except for cultures of *Pseudomonas aeruginosa* which were made daily due to rapid loss of viability. For long term storage of strains, such as transformants, fresh frozen stocks were made by mixing 800 µL of an overnight culture with 500 µL of sterile 80% glycerol (Sigma Aldrich, G2025) in 1.5 ml screw-capped microtubes (Sarstedt, 72.692.005) and stored at -80 °C.

2.4. Plasmid transformation

Escherichia coli BL21-AI strains were transformed with plasmids as listed in Table 2.2. An inoculum of 500 µL of a fresh overnight culture was added to 7.5 mL of LB in 15 mL screw cap tubes and incubated at 37 °C with shaking at 150 rpm. Cultures were grown until they reached an $A_{650\ nm}$ of 0.5-0.6 using an ATI Unicam UV/Vis spectrometer (Model UV2) with Vision 3.33 software. Cells were pelleted by centrifugation for 5 minutes at 4 °C at 3000 x g (Eppendorf, 5702 RH) and the supernatant discarded. Cell pellets were resuspended in 0.5 mL ice cold 100 mM $CaCl_2$ (ThermoFisher Scientific, 10171800) and resuspended on a vortex (Scientific Industries, Vortex-Genie 2). Cells were left on ice for 30 minutes. 100 µL of the competent cells were transferred to a 1.5 mL reaction tube (Sarstedt, 72.690.001) and 2 µL of plasmid DNA added. The mixture was left on ice for a further 20 minutes

and then transferred to a heat block (Thermo Scientific, Compact Drybath S) at 37 °C for 2 minutes and back to the ice for 5 minutes. LB (200 µL) was added to the tube and incubated at 37 °C for 30 minutes. Transformed cells (200 µL) were spread using an inoculation spreader (Sarstedt, 86.1569.001) onto an LB agar plate containing an appropriate antibiotic, either ampicillin (50-100 µg/ml; Melford, A0104) or kanamycin (40 µg/ml; Sigma Aldrich, K1876). Plates were incubated at 30 °C overnight.

2.5. Bacterial viability assays

1 ml of LB containing the appropriate antibiotic in a sterile semi-micro cuvette (Sarstedt, 67.742) was inoculated with 100 µL of an overnight culture of plasmid-transformed cells and sealed with parafilm (Sigma Aldrich, P7668). The culture was incubated at 37°C with shaking at 150 rpm to an $A_{650\ nm}$ of 0.4. Three LB agar plates were poured: one with the appropriate antibiotic, one with the appropriate antibiotic and 0.2% of arabinose (Melford, A3256), and a third with the appropriate antibiotic, 0.2% of arabinose and 1 mM of IPTG (Melford, 156000 MB1008). Ten-fold serial dilutions (10^0 to 10^{-5}) of the culture were performed in LB or PBS (Melford, P32080) and 10 µl applied onto each LB agar plate and incubated overnight at 30 °C. The resulting plates were imaged in the morning and afternoon of the following days.

2.6. Plasmid subcloning

Plasmid DNA was extracted from 3-5 ml of cells using Qiagen QIAprep Spin Miniprep Kit following the manufacturer's instructions. Constructs obtained from Genscript and pFC201 and pFC209 vectors (See Table 2.2) were digested in an appropriate buffer with 1 µl each of NdeI and BamHI purchased from Promega. After 2 hours digestion at 37°C, DNA was separated on 1-2% agarose gels (Melford, A20090) and stained with ethidium bromide (0.5 µg/ml; Sigma, E1510). Insert fragments and linear vector DNA was extracted using a QIAquick Gel Extraction Kit. Vector (3 µl) and insert DNA (12 µl) was mixed in 1x ligation buffer and 1 µl of T4 DNA ligase (Sigma, D2886) and incubated for 1 hour at 20°C and 16 hours at 4°C. 4 µl of the ligation mixture was transformed into DH5α selecting for ampicillin resistance. Successful clones were confirmed by NdeI-BamH digestion and gel electrophoresis.

2.7. Fluorescent stains

All fluorescent stains used for microscopy and fluorescence assays are detailed in table 2.4.

Name	CAS Number	Source	Excitation Maxima / nm	Emission Maxima / nm
SYTO 9	N/A	Thermo Fisher, L7012	485	498
Propidium Iodide (PI)	25535-16-4	Thermo Fisher, L7012	535	617
2-(4-Amidinophenyl)-1H-indole-6-carboxamidine (DAPI)	28718-90-3	Sigma Aldrich, MBD0020	358	461
2-(4-ethoxyphenyl)-6-[6-(4-methylpiperazin-1-yl)-1H-benzimidazol-2-yl]-1H-benzimidazole;trihydrochloride (Hoechst 33342)	875756-97-1	Sigma Aldrich, B2261	361	497
3,3'-Diethyloxacarbocyanine ($DiOC_2(3)$)	905-96-4	Thermo Fisher, B34950	482	501 (670 aggregate)
[(3-Chlorophenyl)hydrazono] malononitrile (CCCP)	555-60-2	Thermo Fisher, B34950	N/A	N/A
2',7'-Dichlorofluorescin diacetate (DCFH-DA)	4091-99-0	Sigma Aldrich, D6883	485	535
N-Phenyl-1-naphthylamine (NPN)	90-30-2	Sigma Aldrich, 104043	350	420
Ethyl 2-[(3Z)-6-(ethylamino)-3-(ethylimino)-2,7-dimethyl-3H-xanthen-9-yl]benzoate hydrochloride (1:1) (Rhodamine 6G)	989-38-8	Sigma Aldrich, 252433	525	548

Table 2.4: Fluorescent stains used in this study.

2.8. Absorption, excitation, and emission spectroscopy

Absorption spectra were recorded using ATI Unicam UV/Vis spectrometer (Model UV2) with Vision 3.33 software. All the steady-state emission and excitation spectra were recorded using ISA Jobin-Yvon Spex Fluorolog-3 luminescence spectrometer using DataMax v2.2 software. Samples were held within 1 cm path length quartz cuvettes. All spectra were recorded in triplicate and averaged.

2.9. Microscopy

All microscopy was performed on a Leica SP5 II LSCM microscope with a HCX PL ACO 63×/1.40 NA LambdaBlue Oil immersion objective coupled to Leica Application Suite Advanced Fluorescence imaging software. The microscope was equipped with an argon laser (458 nm, 476 nm, 488 nm and 514 nm, 20 mW), a HeNe 543 nm laser and a HeNe 633 nm laser (both 50 mW maximum power). The microscope was also coupled to a Coherent 355 nm CW (Nd:YAG, 3rd Harmonic, operating at up to 80 mW power) laser to allow UV excitation. The microscope was equipped with a triple channel imaging detector, comprising two conventional PMT systems and a HyD hybrid avalanche photodiode detector allowing multiple channels to be collected at once. The latter part of the detection system, when operated in the BrightRed mode, can improve imaging sensitivity by 25%, reducing signal to noise by a factor of 5 for red emitting species such as PI. The pinhole was set at 1 airy unit to maximise optical sectioning in the z plane.

2.9.1. Live/Dead staining microscopy of bacteria exposed to chelants

Live/Dead staining microscopy of bacteria exposed to chelants was performed using the LIVE/DEAD™ BacLight™ Bacterial Viability Kit from Invitrogen™. 1 mL of LB was inoculated with 50 µL of a bacterial overnight culture in a 1.5 mL reaction tube. The culture was grown at 37°C with shaking at 150 rpm for 30 minutes. The chelant of interest was added at varying concentrations relative to the minimum inhibitory concentration (MIC).[33] Each culture was grown overnight (16-18 hours) at 37°C with shaking at 150 rpm. 250 µL of the culture was transferred to a fresh 1.5 mL reaction tube and centrifuged at 1713 x g for 5 minutes (Sanyo, Micro-Centaur MSB010.CX1.1) to obtain a pellet and the supernatant discarded. The Live/Dead stain was prepared by diluting the SYTO 9 and PI components in sterile 0.9% NaCl to a final concentration of 5 µM and 30 µM respectively. The pellet was resuspended in 100 µL of the staining solution by pipetting up and down and vortex mixing. 25 µL of the stained bacterial culture and 30 µL of 70% glycerol were added to a sterile concave glass slide (Celestron, #44417), covered with a glass cover slip, and sealed using fast drying clear nail varnish.

Slides for Live/Dead microscopy of chelants were imaged using the system detailed above. Each concentration of chelant was repeated three times using independent bacterial cultures and each biological repeat was used to make three independent slides. The slides were imaged in a two-step sequence, step one used a λ_{ex} of 488 nm (argon laser, 2 mW), a λ_{em} window of 500-520 nm using a PMT detector and included a bright field transmission image. Step two used a λ_{ex} of 533 nm (HeNe, 3 mW) and a λ_{em} window of 550-650 nm using a HyD detector in BrightRed mode. The imaging was carried out using a 1024x1024 window with a scan speed of 100 Hz and a 5x5 tile scan

with automatic image stitching to collect data on as many cells as possible. A 2.5x zoom was used to ensure a flat field due to the nature of the objective used which resulted in a pixel size of 96.2 x 96.2 nm and an optical section of 772 nm.

2.9.2. Microscopy of plasmid transformed strains

5 mL of LB was inoculated with 200 µL of an overnight of bacteria transformed with the appropriate plasmid in a 15 mL screw cap tube. The culture was incubated at 37°C with shaking at 150 rpm to an $A_{650\ nm}$ of 0.4. The culture was split into two 15 mL screw cap tubes, 2.5 mL in each. Arabinose and IPTG were added to one tube giving a final concentration of 0.2% and 1 mM respectively and the other tube was left unaltered. Arabinose and IPTG addition results in induction of expression from the plasmid T7 promoter and inserted gene (induced) but not in cells without these inducers (uninduced). Both tubes were incubated for 1 hour at 37°C with shaking at 150 rpm for 1 hour. 250 µL of each culture was removed and added to a 1.5 mL reaction tube and centrifuged at 5546 x g to pellet the cells. The supernatant was discarded, and the pellet resuspended in 100 µL of an appropriate stain solution by pipetting and vortex mixing. Live/Dead stain was made as detailed above, briefly, SYTO 9 and PI were diluted in 0.9% NaCl for a final concentration of 5 µM and 30 µM. Cells were also stained in DAPI, the staining solution made by diluting DAPI 1 mg/mL solution 1000-fold in PBS (Sigma Aldrich, P4417) to give a final concentration of 1 µg/mL. 10% Triton X100 (Sigma Aldrich, 93443) was added to give a concentration of 0.1%. Stained cells were left at room temperature for 20 minutes for the stain to associate with the cells. 25 µL of the stained bacterial culture and 30 µL of 70% glycerol were added to a sterile concave glass slide, covered with a glass cover slip,

and sealed using fast drying clear nail varnish. Induced and uninduced paired cultures were imaged together in as short a time scale as possible to ensure reproducibility.

Slides for microscopy of transformed strains were imaged using the system detailed above. Each transformed strain was repeated three times using independent bacterial cultures and each biological repeat was used to make three independent slides with both the induced and uninduced version of each transformed strain being imaged a total of nine times. Microscope parameters were the same as detailed above for the Live/Dead microscopy of bacterial cultures treated with chelants. For transformed strains stained with DAPI cells were imaged using a λ_{ex} of 355 nm (Nd:YAG, 3rdH laser, 5 mW) with a λ_{em} of 400-500 nm using a PMT detector with a 514 nm (argon) laser at 2 mW power to also provide a bright field transmission image. The imaging was carried out using a 1024x1024 window with a scan speed of 100 Hz and a 5x5 tile scan with automatic image stitching to collect data on as many cells as possible. A 2.5x zoom was used to ensure a flat field due to the nature of the objective used which resulted in a pixel size of 96.2 x 96.2 nm and an optical section of 772 nm.

2.9.3. Microscopy of λ lysogens

5 mL of LB was inoculated with 200 µL of an overnight culture of bacteria in a 15 mL screw cap tube. The culture was incubated at 30°C with shaking at 150 rpm to an $A_{650\ nm}$ of 0.4. The culture was split into two 15 mL screw cap tubes, 2.5 mL in each. One tube was incubated for 30 minutes at 30°C (uninduced) with shaking at 150 rpm and the other incubated at 42°C (induced) with shaking at 150 rpm for 30 minutes. 250 µL of each culture was removed and added to a 1.5 mL reaction tube and centrifuged

at 5546 x g to pellet the cells. The supernatant was discarded, and the pellet was resuspended in 100 µL of Live/Dead stain solution by pipetting up and down and vortex mixing. Live/Dead stain was made as detailed above, briefly, SYTO 9 and PI were diluted in 0.9% NaCl for a final concentration of 5 µM and 30 µM respectively. 25 µL of the stained bacterial culture and 30 µL of 70% glycerol were added to a sterile concave glass slide, covered with a glass cover slip, and sealed using fast drying clear nail varnish.

Slides for Live/Dead microscopy of lysogens were imaged using the system detailed above. Each lysogen strain, both induced and uninduced, was repeated three times using independent bacterial cultures and each biological repeat was used to make three independent slides. The slides were imaged in a two-step sequence, step one used a λ_{ex} of 488 nm (argon laser, 2 mW), a λ_{em} window of 500-520 nm using a PMT detector and included a bright field transmission image. Step two used a λ_{ex} of 533 nm (HeNe 3 mW) and a λ_{em} window of 550-650 nm using a HyD detector in BrightRed mode. The imaging was carried out using a 1024x1024 window with a scan speed of 100 Hz and a 5x5 tile scan with automatic image stitching to collect data on as many cells as possible. A 2.5x zoom was used to ensure a flat field due to the nature of the objective used which resulted in a pixel size of 96.2 nm x 96.2 nm and an optical section of 772 nm.

2.9.4. Size measurements and morphology of *S. aureus* mutant strains

1 mL of LB was inoculated with 50 µL of a bacterial overnight culture in a 1.5 mL reaction tube. The culture was grown at 37°C with shaking at 150 rpm until an $A_{650\,nm}$

of 0.4 was reached. 250 µL of the culture was transferred to a fresh 1.5 mL reaction tube and centrifuged at 1713 x g for 5 minutes to obtain a pellet and the supernatant discarded. The Live/Dead stain was prepared by diluting the SYTO 9 and PI components in sterile 0.9% NaCl to a final concentration of 5 µM and 30 µM respectively. The pellet was resuspended in 100 µL of the staining solution by pipetting up and down and vortex mixing. 25 µL of the stained bacterial culture and 30 µL of 70% glycerol were added to a sterile concave glass slide, covered with a glass cover slip, and sealed using fast drying clear nail varnish.

Slides for Live/Dead microscopy of *S. aureus* mutants were imaged using the system detailed above. Each mutant strain was repeated three times using independent bacterial cultures and each biological repeat was used to make three independent slides. The slides were imaged in a two-step sequence, step one used a λ_{ex} of 488 nm (argon laser, 2 mW), a λ_{em} window of 500-520 nm using a PMT detector and included a bright field transmission image. Step two used a λ_{ex} of 533 nm (HeNe, 3 mW) and a λ_{em} window of 550-650 nm using a HyD detector in BrightRed mode. The imaging was carried out using a 1024x1024 window with a scan speed of 100 Hz and a 5x5 tile scan with automatic image stitching to collect data on as many cells as possible. A 2.5x zoom was used to ensure a flat field due to the nature of the objective used which resulted in a pixel size of 96.2 x 96.2 nm and an optical section of 772 nm.

2.9.5. Image analysis

All image processing and data extraction was performed using Fiji (v1.53q[61]). Details of the parameters and settings are provided in detail in the relevant sections, but some general principles apply to all analyses. For comparisons between series, any

adjustments of brightness and contrast were kept identical for the full series. Scale bars are consistently set at 25 µm throughout unless stated otherwise to allow ease of comparability.

2.10. Fluorescence Plate Reader Assays

2.10.1. Reactive oxygen species assay

1 mL of LB was inoculated with 50 µL of overnight culture and incubated at 37 °C with shaking until at an $OD_{600\ nm}$ of 0.3. The culture was centrifuged at 1713 x g for 5 minutes (Sanyo, Micro-Centaur MSB010.CX1.1) to obtain a pellet. The supernatant was discarded and washed twice with PBS using the same centrifuge parameters. The pellet was finally resuspended in PBS with DCFH-DA at a concentration of 10 µM. The chelant of interest was added at one of the concentrations to be studied and the bacteria were incubated at 37 °C with shaking for 30 minutes (SciQuip, SQ-4010). 100 µL of the sample was added to black 96 well plates for fluorescence (Thermo Fisher, 237105). The fluorescence intensity was measured with a fluorescence plate reader (Agilent BioTek Synergy H4 Hybrid Microplate Reader), using the parameters for excitation and emission collection of: λ_{ex} = 485 nm, λ_{em} = 535±10 nm. All chelants were studied at concentrations of 0.1, 1 and 10 mM with three biological repeats and three technical repeats in each biological repeat.

2.10.2. Outer membrane integrity assay

1 mL of LB was inoculated with 50 µL of overnight culture and incubated at 37 °C with shaking until at an $OD_{600\ nm}$ of 0.3. The culture was centrifuged at 1713 x g for 5 minutes (Sanyo, Micro-Centaur MSB010.CX1.1) to obtain a pellet. The supernatant was discarded and washed twice with PBS using the same centrifuge parameters. The pellet was finally resuspended in PBS. The chelant of interest was added at one of the concentrations to be studied and the bacteria were incubated at 37 °C with shaking for 30 minutes (SciQuip, SQ-4010). NPN was added to give a final concentration of 5 µM and the bacteria were incubated for a further 30 minutes at 37 °C with shaking. 100 µL of the sample was added to black 96 well plates for fluorescence (Thermo Fisher, 237105). The fluorescence intensity was measured with a fluorescence plate reader (Agilent BioTek Synergy H4 Hybrid Microplate Reader), using the parameters for excitation and emission collection of: λ_{ex} = 350 nm, λ_{em} = 420±10 nm. All chelants were studied at concentrations of 0.1 and 1 mM with three biological repeats and three technical repeats in each biological repeat.

3. Effects of chelants on the bacterial cell envelope

3.1. Introduction

3.1.1. Structure of the bacteria cell envelope

Bacteria have a complex multi-layered cell envelope comprising either one or two lipid bilayers. Bacteria can be broadly classified into two categories based on their cell envelope by the Gram stain which separates bacteria based on their membrane's ability to retain the purple stain crystal violet: Gram-positive bacteria retain the stain whereas Gram-negative don't.[62] The structure the bacterial cell envelope is shown in figure 3.1 which shows the difference between the two broad categories of bacteria.

Both types of bacteria have a cytoplasmic membrane which are very similar, however, the exterior of the cells differ. Gram-positive bacteria have a thick layer of peptidoglycan, a large macromolecular polysaccharide consisting of sugars and amino acids, on the outer surface with long anionic polymers called teichoic acids embedded in the peptidoglycan layer. In Gram-positive species the peptidoglycan constitutes up to 90% of the dry weight of the cell envelope. It is this thick layer of peptidoglycan that traps the crystal violet staining the bacteria purple in the Gram stain.

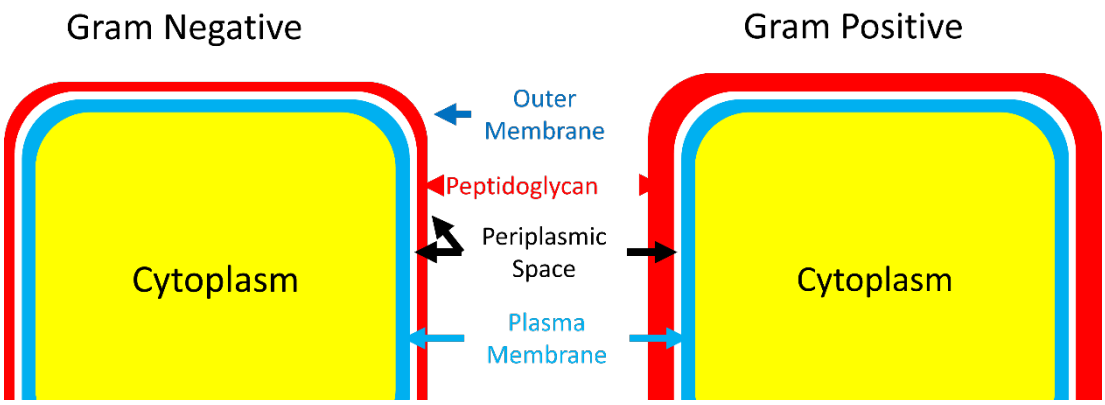

Figure 3.1: Structure of Gram-positive and Gram-negative bacterial cell envelopes. The yellow indicates the inside of the cell (cytoplasm), the blue is the plasma membrane, red is the peptidoglycan layer and the gaps between is the periplasmic space.

Gram-negative bacteria possess two lipid bilayer membranes which sandwich a thin peptidoglycan layer; the outer membrane contains lipopolysaccharide, efflux pumps, porins and other transport proteins.[63] The presence of this fortified outer membrane tends to make Gram-negative bacteria more resistant to antibiotics than Gram-positives.[64]

The hydrophobic lipid bilayer of the outer membrane, together with its membrane porins with size-exclusion properties, acts as a selective barrier to the entry of molecules.[65] Hydrophobic antibiotics can pass through the outer membrane by diffusion, whereas hydrophilic drugs require the presence of diffusion porins to be taken up by Gram-negative bacteria. Therefore, changes in the lipid or protein composition of the outer membrane can affect entry of these drugs, as seen in many antibiotic-resistant strains, including *E. coli*.[66]

3.1.2. Assessing Outer Membrane Damage – Using NPN

1-N-phenylnapthylamine (NPN), the structure of which is shown in figure 3.2, is a small hydrophobic non-polar fluorescent molecule which has been used to assess the outer membrane of the Gram-negative bacteria.

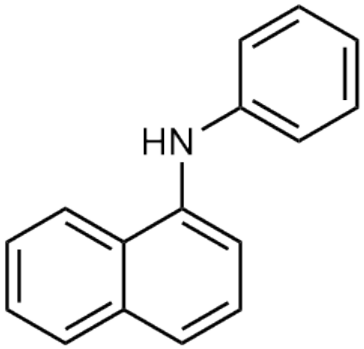

Figure 3.2: Structure of NPN.

NPN fluorescence is quenched in aqueous environments but fluoresces much more strongly in the hydrophobic interior of the phospholipid bilayer due to the solvation elimination of quenching of OH oscillators of water. The emission spectra of NPN in both water and octanol is shown in figure 3.3 to illustrate the difference in fluorescence intensity between these environments. Here, octanol is used to simulate a membrane-like environment and the fluorescence increases 15-fold at the maximum emission wavelength indicating that it can be used effectively to detect membrane damage and disruption.

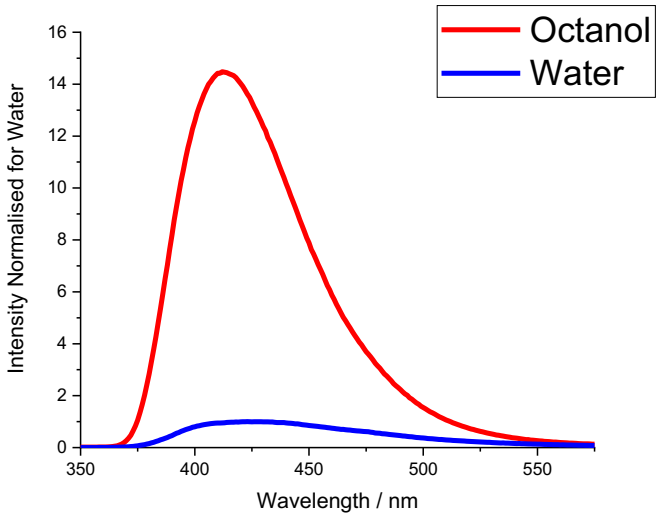

Figure 3.3: Emission spectrum of NPN in water and octanol. NPN dissolved in water (blue) and octanol (red) to show the quenching of NPN by water. Both spectra are normalised with respect to the water spectrum. λ_{ex} *= 350 nm.*

The intact Gram-negative outer membrane functions as a permeability barrier that excludes many external hydrophobic molecules, such as NPN, due to its bilayer structure containing a high proportion of lipopolysaccharide molecules within the outer leaflet and glycerophospholipids within the inner leaflet. However, if membrane integrity is compromised, NPN can readily penetrate the lipid portion of the bilayer and fluoresce. This sensitive spectral shift of NPN in different environments allows detection of NPN uptake and outer membrane permeability changes and can indicate weakening of the outer membrane.[67] However, NPN shows limited efficacy as a measure of membrane permeability in Gram-positive bacteria, since they lack the presence of an outer membrane.

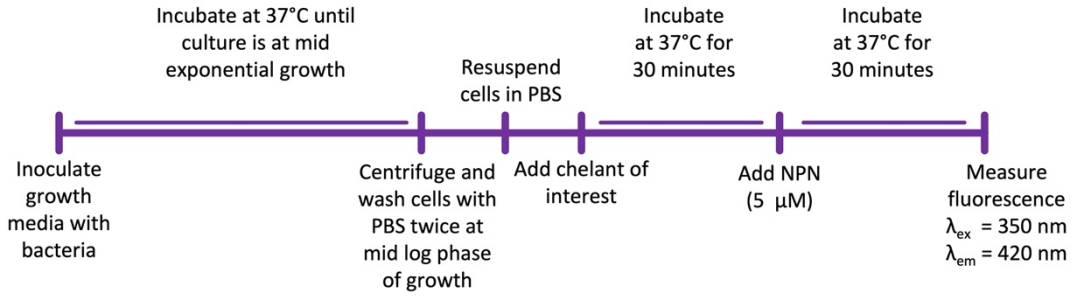

Figure 3.4: Outer membrane integrity assay protocol timeline.

The protocol and timeline for the NPN assay used to investigate chelant effects on bacterial membrane permeability is shown in figure 3.4. An important point to note is that NPN must be added after the bacteria have been exposed to the chelant of interest, allowing time for chelant to affect the bacterial membrane. NPN associates rapidly with the membrane so fluorescence intensity can be measured soon after exposure.

3.1.3. Inner membrane damage – Live/Dead staining

To assess the integrity of the cytoplasmic, or inner, membrane a viability stain was used. SYTO 9 and Propidium Iodide (PI) are used in combination to determine bacterial cell viability, which is defined, in this case, as a function of the inner membrane permeability. Once the inner membrane is permeabilised the cell is considered to be inviable and is effectively dead. The structures of PI and SYTO 9[68] are shown in figure 3.5.

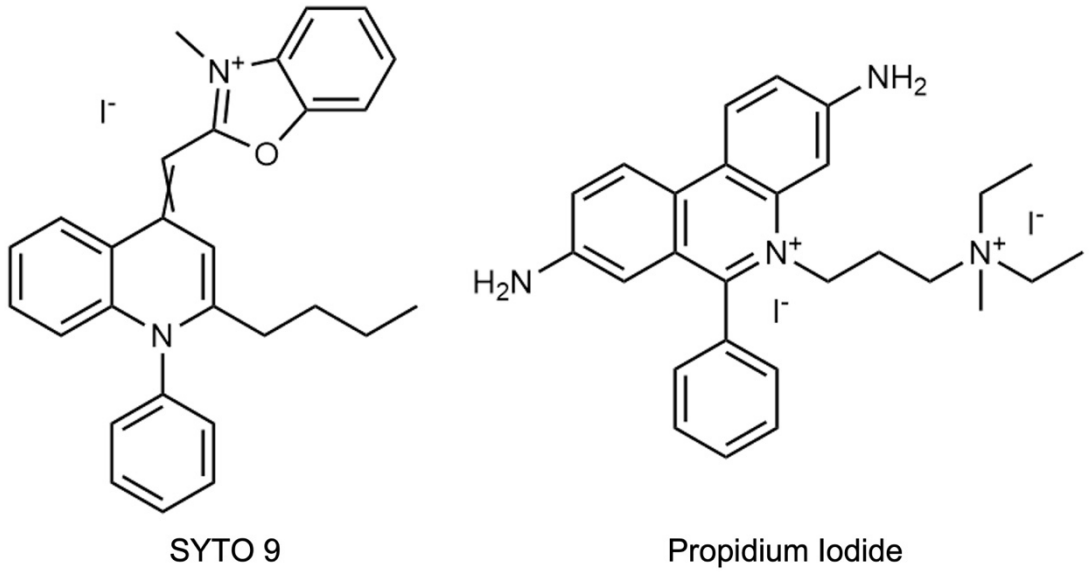

Figure 3.5: Structure of SYTO 9 and Propidium Iodide.

Both stains are nucleic acid stains and intercalate with DNA and RNA bases. When bound to RNA or DNA the fluorescence intensity of both stains increases significantly. When bound to DNA, SYTO 9 has a fluorescence enhancement of 600-fold and when bound to RNA there is an increase of 1400-fold. When PI binds to DNA its fluorescence intensity is increased 30-fold and the emission undergoes a hypsochromic shift of ~20 nm. PI has a stronger binding affinity for DNA than SYTO 9, so when both are present the SYTO 9 can be displaced by the PI meaning only one stain will fluoresce when excited.[69,70]

SYTO 9 is a “live” stain and PI is a “dead” stain; SYTO 9 can passively pass through both the outer and inner membrane of all bacteria whereas PI is only able to pass through the outer membrane (if it is present) and the peptidoglycan. This means that cells that are healthy and have a viable inner membrane will be stained with SYTO 9 exclusively. Once the integrity of the inner membrane is diminished PI is able to enter

the cell and intercalate with the DNA, displacing SYTO 9 and the fluorescence profile of the cell changes. Figure 3.6 shows the excitation and emission spectra of both SYTO 9 and PI. In these spectra there was DNA added to the solution to simulate the intracellular environment and obtain the correct profile of excitation and emission.

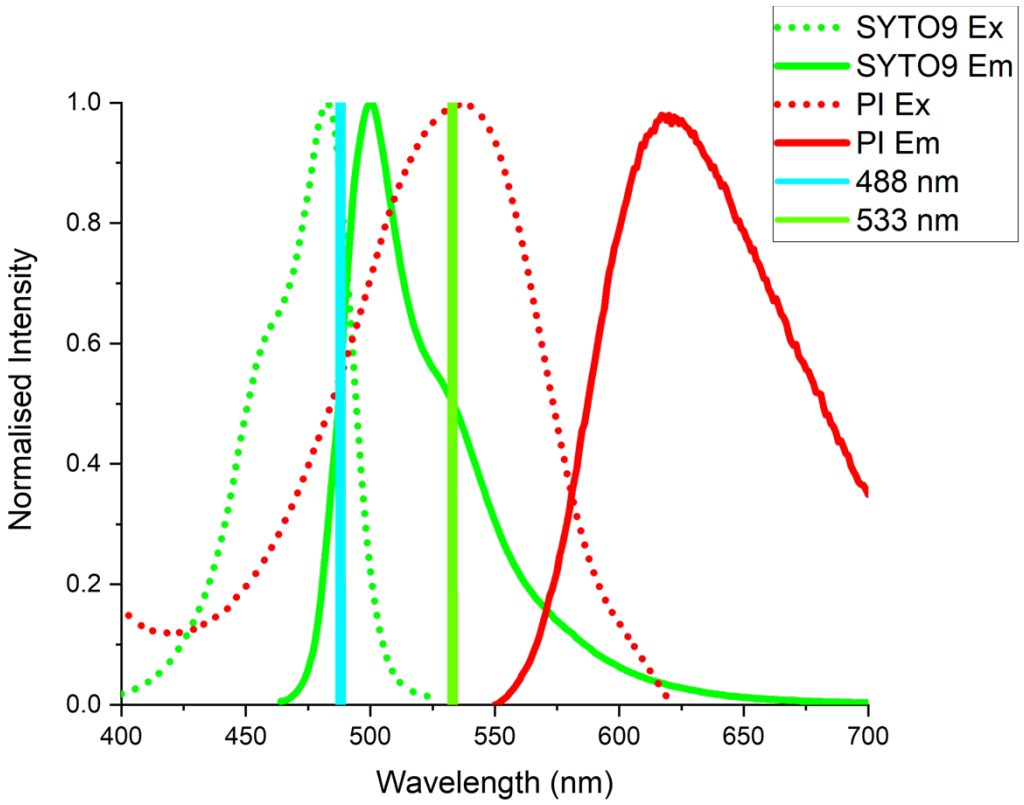

Figure 3.6: Excitation and emission spectra of SYTO 9 and Propidium Iodide in water with added DNA. SYTO 9, λ_{ex} = 450 nm, λ_{em} = 530 nm. PI, λ_{ex} = 500 nm, λ_{em} = 650 nm. Also shown are the two laser lines used for excitation in microscopy, 488 nm and 533 nm for SYTO 9 and PI respectively.

Also shown are the laser lines used to excite the fluorophores, 488 and 533 nm for SYTO 9 and PI respectively. This shows when using the 488 nm laser line both fluorophores are excited, but since the detector only collects emission from 500-520

nm there will be no emission from PI detected. Upon excitation with the 533 nm laser line no SYTO 9 will be excited and only PI fluorescence will be detected.

Figure 3.7 shows the protocol and timeline for the inner membrane damage assay.

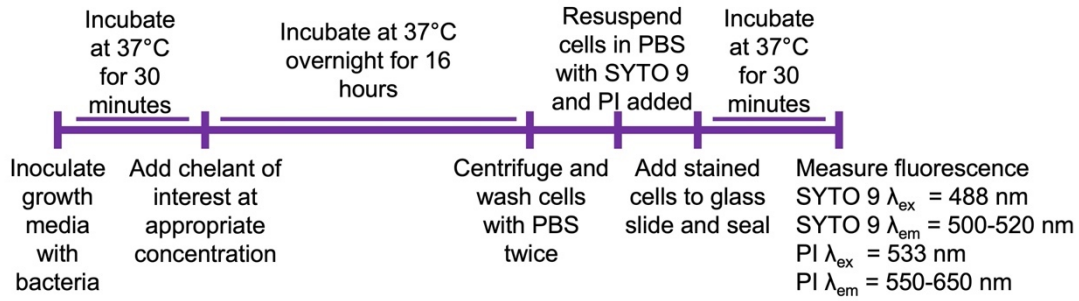

Figure 3.7: Inner membrane integrity assay protocol timeline.

3.2. Effect of EDTA on the bacterial cell envelope

Previous work has shown that EDTA causes damage to the outer membrane of cells in *E. coli* and *P. aeruginosa* so effects on membrane integrity by this chelant were investigated further using two representative Gram-negatives, *E. coli* and *S. marcescens*, in comparison with a Gram-positive, *S. aureus*.

Figure 3.8 shows the effect of EDTA on the inner and outer membrane of *E. coli* and *S. marcescens* through Live/Dead staining and NPN fluorescence. *S. aureus* was also examined, with both methods, although the NPN assay was not expected to reveal changes as this species lacks an outer membrane.

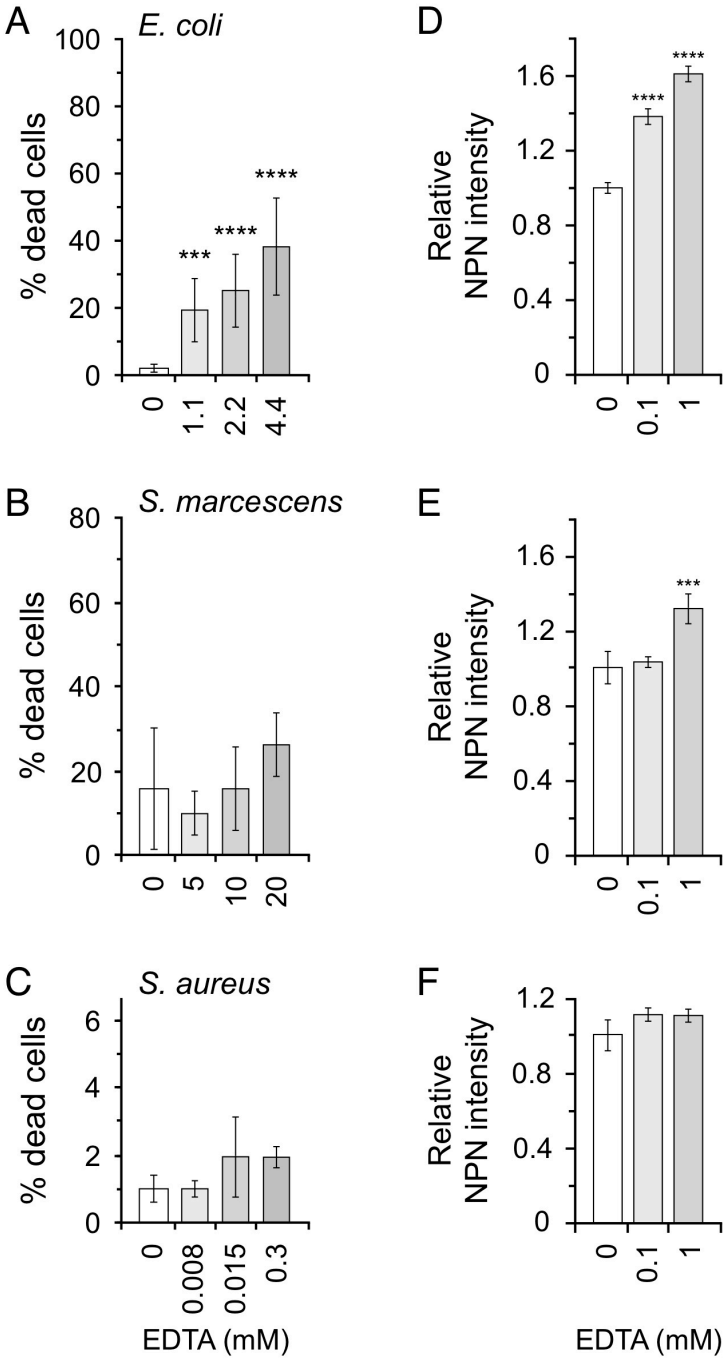

Figure 3.8: Effect of EDTA exposure on the bacterial cell envelope. Left, damage to the inner cell membrane as indicated by the percentage of cells stained as "dead" by PI when exposed to 6.25%, 12.5% and 25% of the MIC of EDTA in E. coli (A), S. marcescens (B) and S. aureus (C). Right, damage to the outer membrane as indicated by the relative intensity of NPN when exposed to 0.1 and 1 mM EDTA in E. coli (D), S. marcescens (E) and S. aureus (F).

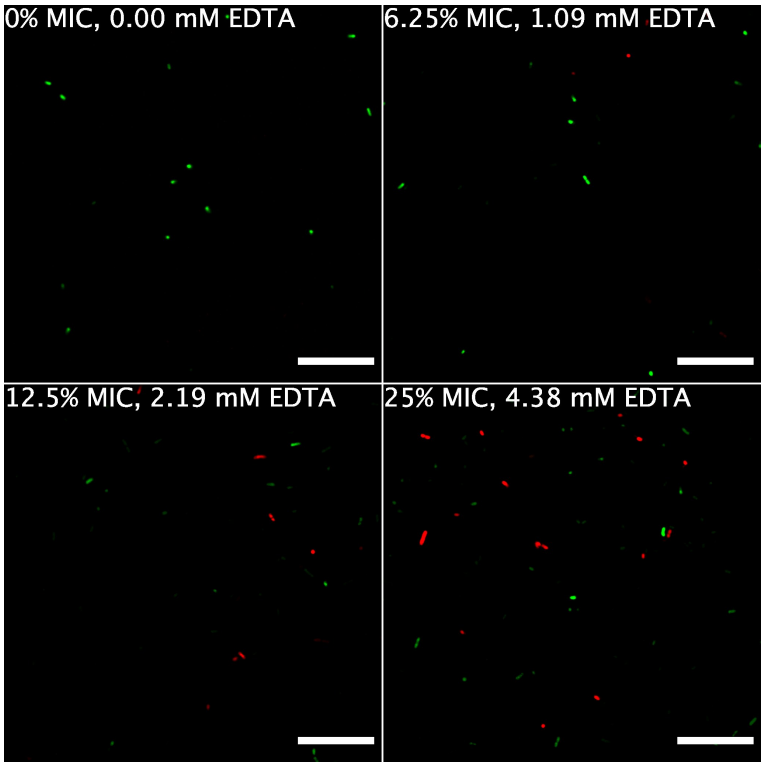

Figure 3.9: Live/Dead staining of E. coli exposed to EDTA. LSCM images of E. coli exposed to 0% MIC, 6.25% MIC, 12.5% MIC and 25% MIC EDTA and stained with SYTO9 (green) and PI (red). SYTO9, λ_{ex} = 488 nm, λ_{em} = 500-520 nm. PI, λ_{ex} = 533 nm, λ_{em} = 550-650 nm. Scale bar = 25 µm.

EDTA has a significant detrimental effect on both inner and outer membranes of *E. coli* (Figure 3.8 and 3.9), as well as reducing cellular levels of Mn, Fe and Zn (Paterson et al 2022). Exposure of *E. coli* to sub-MIC concentrations of EDTA causes an increase in NPN fluorescence, consistent with outer membrane damage that allows NPN to enter the lipid bilayer. This is apparent even at 0.1 mM EDTA which is 0.57% the MIC of EDTA for *E. coli* (17.5 mM) indicating that even low EDTA concentrations induce outer membrane damage. It also suggests that membrane damage, and therefore increased membrane permeability, is not the primary mechanism of growth inhibition because the MIC would have been expected to be lower. The percentage of dead cells, indicated by the number of cells with red fluorescence from PI being

able to bypass the inner membrane of the cell envelope, increases at concentrations of only 6.25% of the EDTA MIC concentration. Both membranes are therefore damaged and permeability increased. The percentage of stained cells increases linearly with the concentration of EDTA (Fig. 3.8). The mechanism responsible for damage to both inner and outer membranes is unclear, although these results support a direct effect on the membrane rather than indirect causes due to metal sequestration or an inability to synthesise key membrane components. No morphological changes were observed with *E. coli* exposed to EDTA.

Figure 3.10 shows LSCM images of *S. marcescens* exposed to EDTA. EDTA does not have such a pronounced effect on *S. marcescens* as it does on *E. coli*. At the sub-MIC concentrations used, the percentage of cells stained with PI does not significantly change with addition of EDTA. Given that these concentrations are not sufficient to inhibit *S. marcescens* growth, it may be that some membrane damage occurs at higher concentrations closer to the MIC, but the main antibacterial effects is more likely through metal deprivation. This is supported by the results of the outer membrane damage assay (Fig. 3.8E). As judged by increased NPN fluorescence, the outer membrane is damaged by 1 mM EDTA (1.25% of the MIC). Hence, EDTA induces some damage to the outer membrane but this does not appear to be enough for full permeabilisation. As with *E. coli*, no morphological changes were observed when *S. marcescens* is exposed to EDTA.

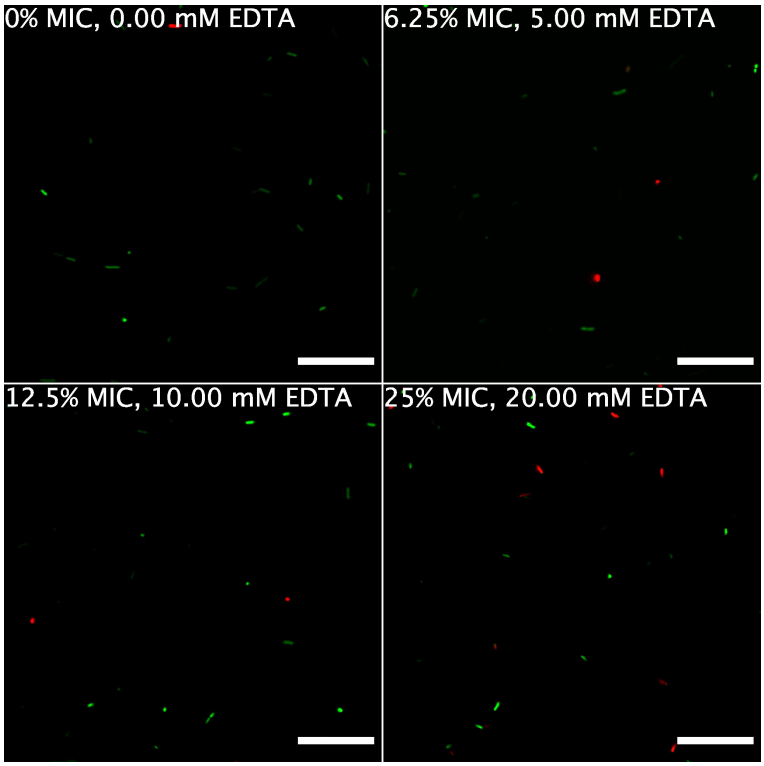

Figure 3.10: Live/Dead staining of S. marcescens exposed to EDTA. LSCM images of S. marcescens exposed to 0% MIC, 6.25% MIC, 12.5% MIC and 25% MIC EDTA and stained with SYTO9 (green) and PI (red). SYTO9, λ_{ex} = 488 nm, λ_{em} = 500-520 nm. PI, λ_{ex} = 533 nm, λ_{em} = 550-650 nm. Scale bar = 25 µm.

EDTA does not appear to have any effect on the membrane of *S. aureus* at sub-MIC concentrations of EDTA (Figure 3.8C and Fig. 3.11).

This suggests differing mechanisms of antibacterial activity with EDTA against Gram-positive and Gram-negative species. No morphological changes were detected when *S. aureus* was exposed to EDTA.

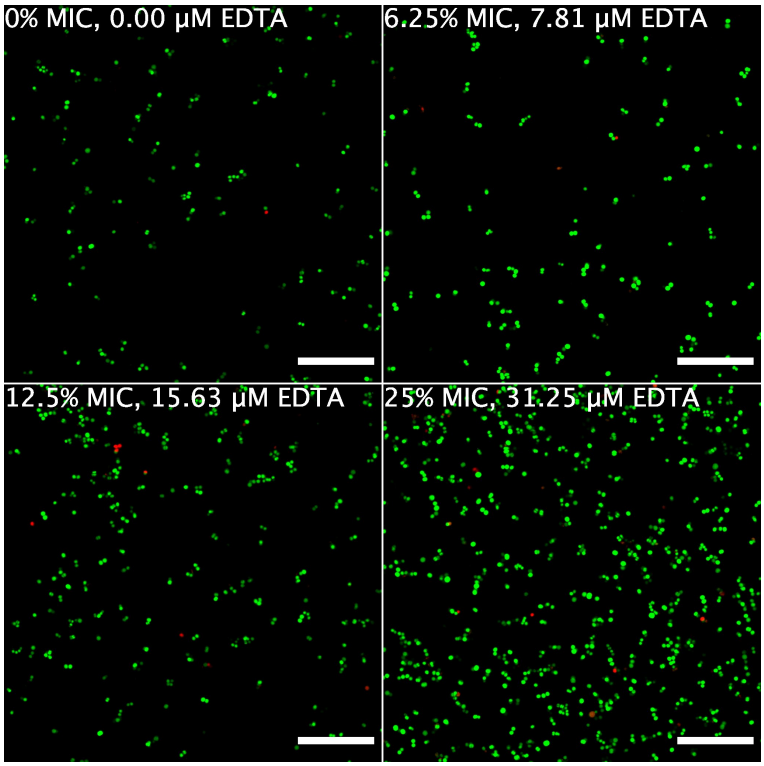

Figure 3.11: Live/Dead staining of S. aureus exposed to EDTA. LSCM images of S. aureus exposed to 0% MIC, 6.25% MIC, 12.5% MIC and 25% MIC EDTA and stained with SYTO9 (green) and PI (red). SYTO9, λ_{ex} = 488 nm, λ_{em} = 500-520 nm. PI, λ_{ex} = 533 nm, λ_{em} = 550-650 nm. Scale bar = 25 µm.

3.3. Effect of DTPMP on the bacterial cell envelope

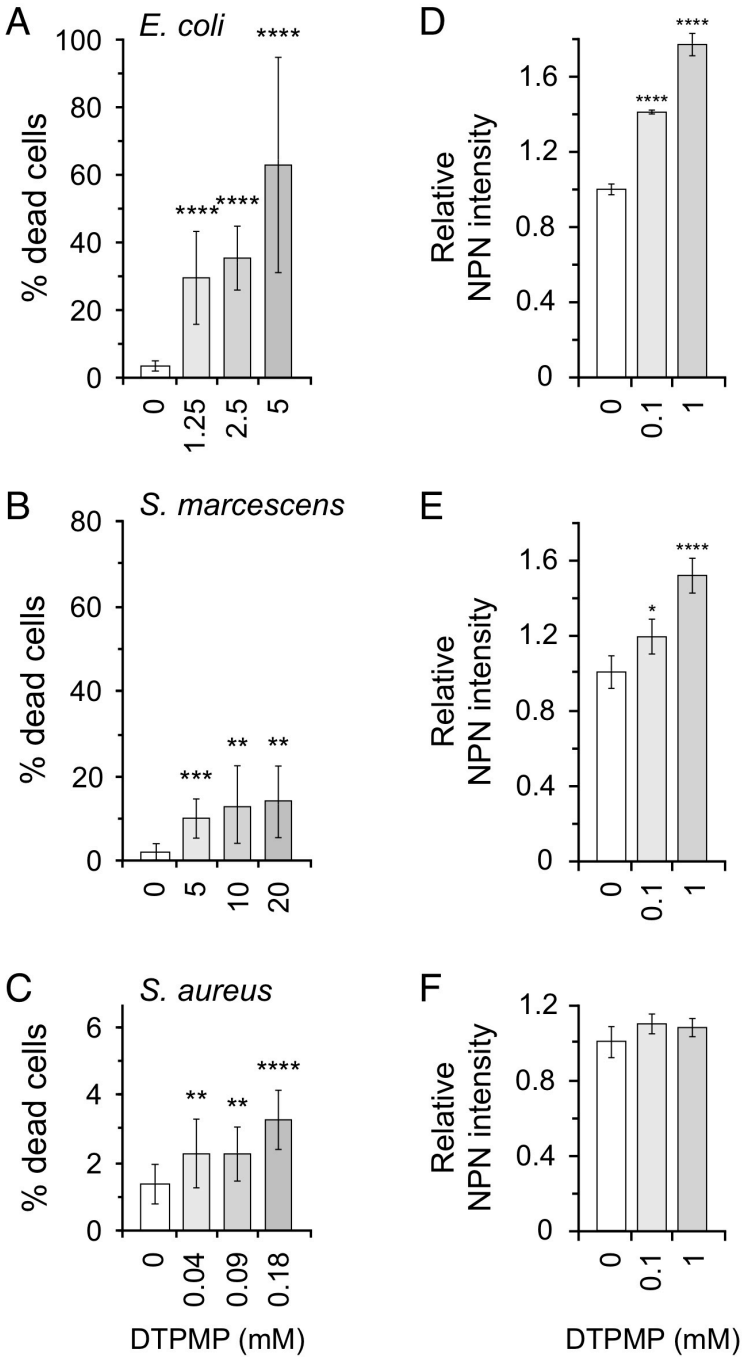

Figure 3.12: Effect of DTPMP exposure on the bacterial cell envelope. Left, damage to inner cell membrane as indicated by the percentage of cells stained as "dead" by PI when exposed to 6.25%, 12.5% and 25% of the MIC of DTPMP in E. coli (A), S. marcescens (B) and S. aureus (C). Right, damage to the outer cell membrane as indicated by the relative intensity of NPN when exposed to 0.1 and 1 mM DTPMP in E. coli (D), S. marcescens (E) and S. aureus (F).

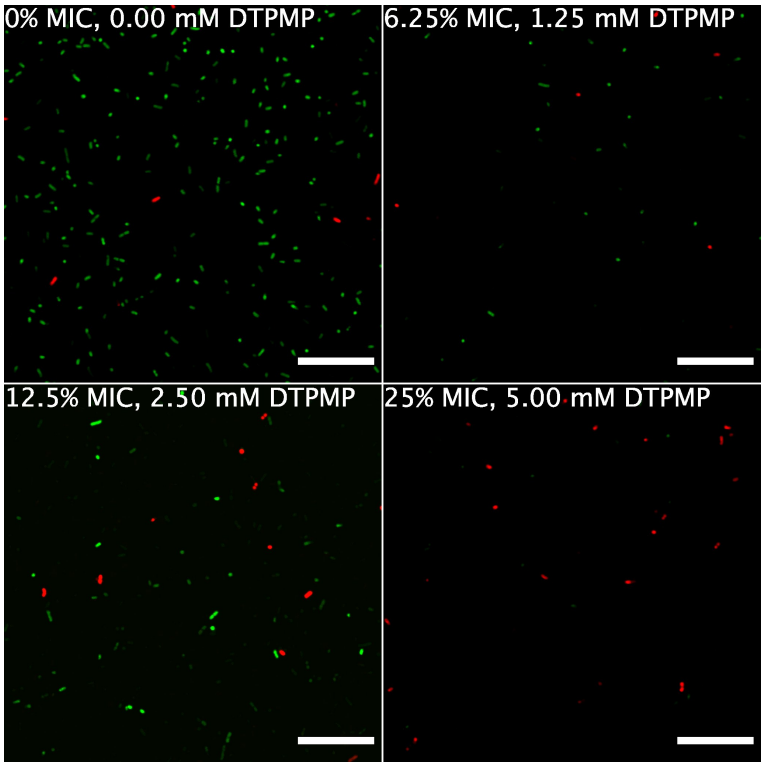

Figure 3.13: Live/Dead staining of E. coli exposed to DTPMP. LSCM images of E. coli exposed to 0% MIC, 6.25% MIC, 12.5% MIC and 25% MIC DTPMP and stained with SYTO9 (green) and PI (red). SYTO9, λ_{ex} = 488 nm, λ_{em} = 500-520 nm. PI, λ_{ex} = 533 nm, λ_{em} = 550-650 nm. Scale bar = 25 µm.

DTPMP has a similar effect on the *E. coli* membrane as EDTA (Figure 3.12A), which is not entirely unexpected given the similarity in their chemistries. The linear increase in both inner and outer membrane injury, which matches that of EDTA, indicates a direct membrane damaging mechanism for both compounds because their effects on cellular metal content are radically different.[32] The capacity to maintain growth despite impairment in membrane integrity and permeability indicates that the membrane effects are not sufficient to be the sole antibacterial mechanism of action of DTPMP against *E. coli*, though it likely contributes to efficacy.

In microscopy assays (Figure 3.13), the total number of cells, both alive and dead, decreased as the concentration of DTPMP increased. There are two possible explanations for this. Either fewer bacteria were present because of growth inhibition by the chelant or that damage to the cell envelope resulted in cell lysis and loss of recovery following centrifugation. To determine which explanation was correct, two approaches were used, a) measuring the optical density of the culture before centrifugation, and b) staining the cells directly after growth without centrifugation and washing. The optical density of the cultures with and without DTPMP yielded similar values and direct staining of the cultures confirmed that a similar number of cells were present either with or without DTPMP. This suggests that membrane damage is the main reason and that the centrifugal force applied during cell pellet recovery contributes to cell lysis.

Unlike EDTA, DTPMP does act more significantly on the cell envelope of *S. marcescens* (Figure 3.12B and 3.14). Both the inner and outer membranes are affected negatively, although not as much as *E. coli*. At 0.1 mM DTPMP, 0.125% of the MIC for *S. marcescens*, some outer membrane damage was evident as judged by the increase in NPN fluorescence. Similarly, a measurable increase in PI fluorescence, indicating inner membrane damage was apparent at low DTPMP concentrations.

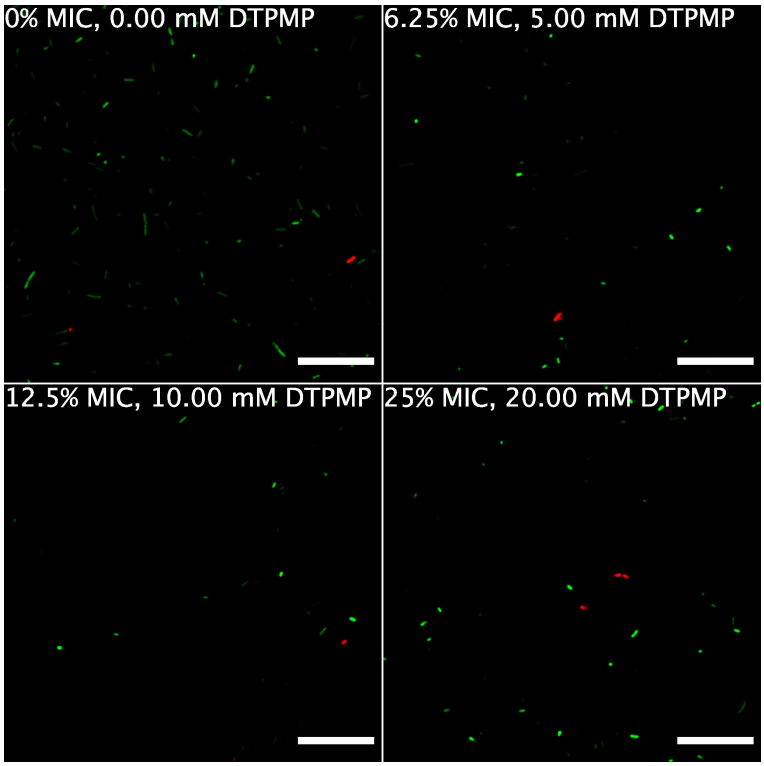

Figure 3.14: Live/Dead staining of S. marcescens exposed to DTPMP. LSCM images of S. marcescens exposed to 0% MIC, 6.25% MIC, 12.5% MIC and 25% MIC DTPMP and stained with SYTO9 (green) and PI (red). SYTO9, λ_{ex} = 488 nm, λ_{em} = 500-520 nm. PI, λ_{ex} = 533 nm, λ_{em} = 550-650 nm. Scale bar = 25 µm.

With *S. aureus*, the percentage of cells stained with PI increased slightly as the concentration of DTPMP increased, suggesting damage to the cytoplasmic membrane (Figure 3.12C and 3.15). No change in NPN fluorescence was detected but since *S. aureus* is a Gram-positive species this was anticipated. The level of membrane damage with DTPMP differs from that seen with EDTA against *S. aureus* despite their similar chemistries. The number of dead cells does remain low, however, with only 3% of cells stained with PI.

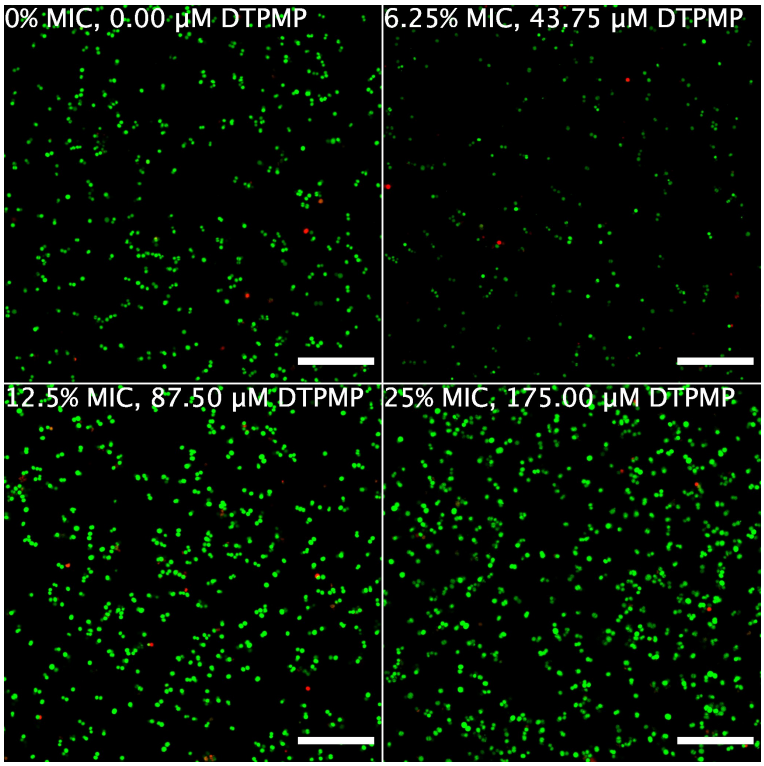

Figure 3.15: Live/Dead staining of S. aureus exposed to DTPMP. LSCM images of S. aureus exposed to 0% MIC, 6.25% MIC, 12.5% MIC and 25% MIC DTPMP and stained with SYTO9 (green) and PI (red). SYTO9, λ_{ex} = 488 nm, λ_{em} = 500-520 nm. PI, λ_{ex} = 533 nm, λ_{em} = 550-650 nm. Scale bar = 25 µm.

3.4. Effect of CHA on the bacterial cell envelope

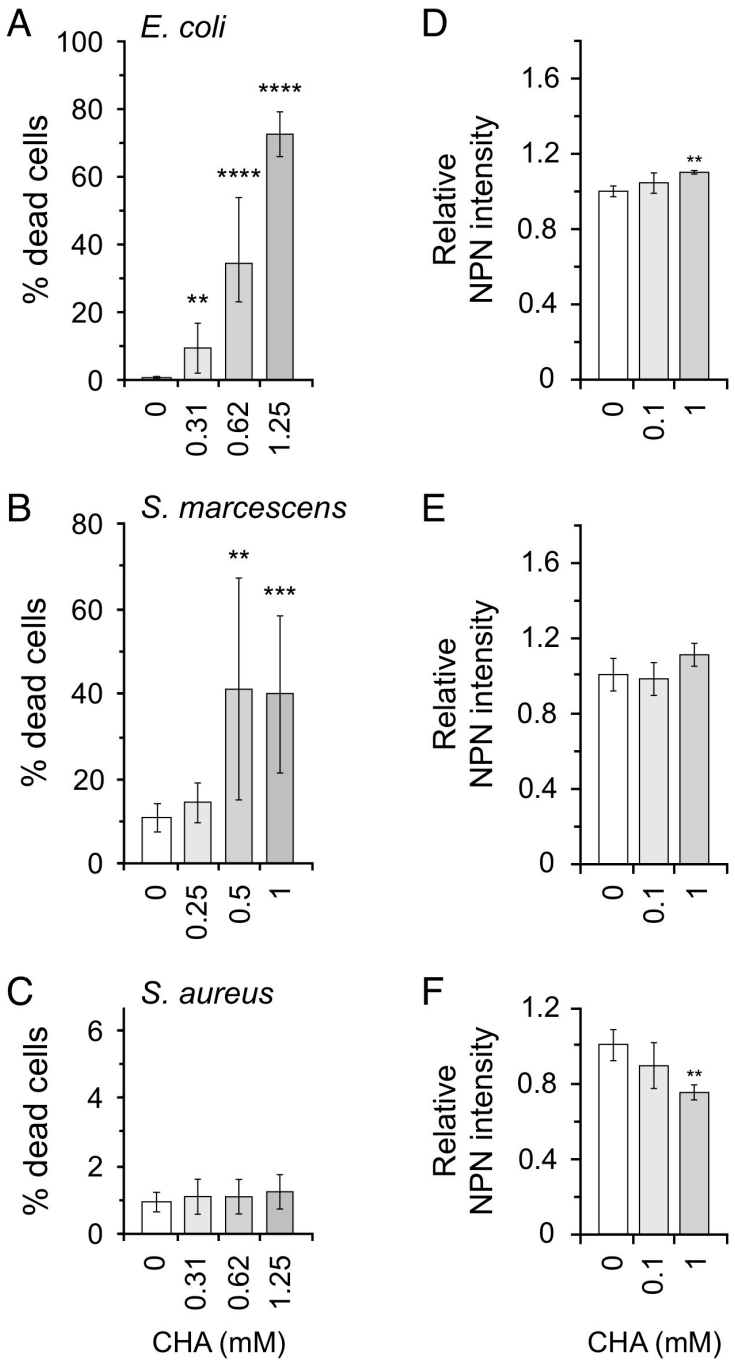

Figure 3.16: The effect of CHA exposure on the bacterial cell envelope. Left, damage to inner cell membrane as indicated by the percentage of cells stained as "dead" by PI when exposed to 6.25%, 12.5% and 25% of the MIC of CHA in E. coli (A), S. marcescens (B) and S. aureus (C). Right, damage to the outer cell membrane as indicated by the relative intensity of NPN when exposed to 0.1 and 1 mM CHA in E. coli (D), S. marcescens (E) and S. aureus (F).

CHA is a hydroxamic acid that had no apparent effect on the cellular metal content of *E. coli*.[23] Effects on the inner and outer membrane of CHA on *E. coli*, *S. marcescens* and *S. aureus* by Live/Dead staining and NPN fluorescence are shown in Figure 3.16.

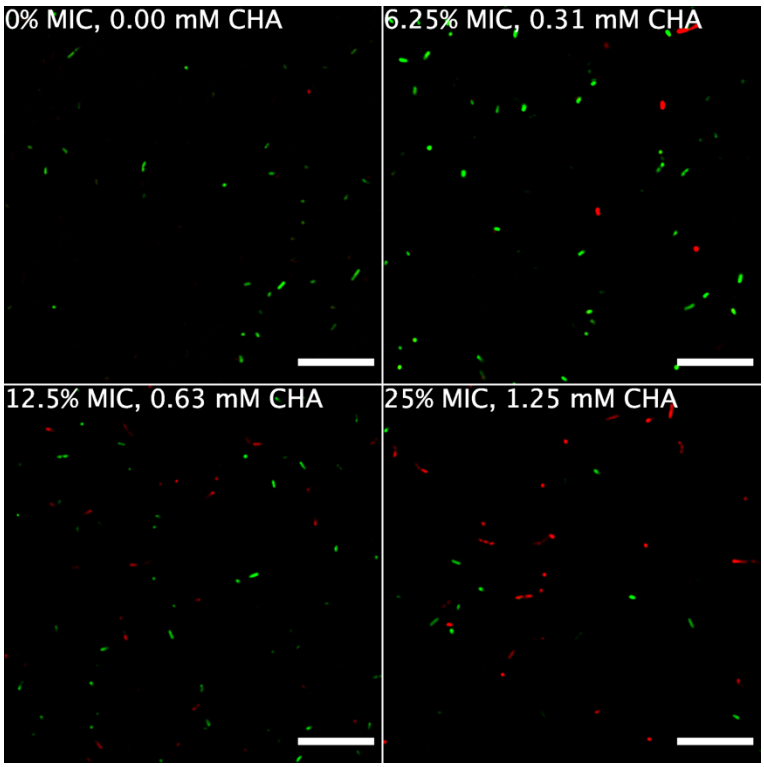

Figure 3.17: Live/Dead staining of E. coli exposed to CHA. LSCM images of E. coli exposed to 0% MIC, 6.25% MIC, 12.5% MIC and 25% MIC CHA and stained with SYTO9 (green) and PI (red). SYTO9, λ_{ex} = 488 nm, λ_{em} = 500-520 nm. PI, λ_{ex} = 533 nm, λ_{em} = 550-650 nm. Scale bar = 25 µm.

CHA has significant detrimental effects on the cell envelope of *E. coli* (Figure 3.17), although there are contrasting results for outer and inner membrane damage from the two tests applied. The results of the NPN assay indicate little or no outer membrane damage occurs (Figure 3.16A). In contrast the Live/Dead staining suggests a high degree of damage. Approximately 70% of the cells stain with PI at concentrations only 25% of the MIC indicating a high degree of membrane damage

(Figure 3.16A and 3.17). Since CHA does not alter cellular metal levels, these results suggest that membrane damage may be a key component in the antibacterial mechanism of action of CHA against *E. coli*.

This is not surprising given the structure of CHA, which has a surfactant-like structure with a polar hydroxamate head and a non-polar, 7-membered carbon tail. It could be expected that the surfactant like structure of the molecule induces some membrane damage by inserting its tail group into the bilayer of the membrane and the head group on the outside of the membrane where it can still act as a chelating agent for metals. This proposed mechanism could explain the discrepancy between the two results, the membrane is disrupted but is insufficient to allow a breach to form that would allow NPN insertion, hence the limited changes seen in fluorescence.

The Live/Dead staining also revealed that the size of the cells increases in parallel with CHA concentration. Figure 3.18 shows a box and whisker plot of the length of *E. coli* cells when exposed to increasing amounts of CHA. The length of the cells does not change significantly until 25% of the MIC has been reached. There are two possible explanations for this cell size increase: the membrane has been disrupted to such a degree that the cell volume increases and hence the cells are longer; or the process of cell division has been interrupted, producing elongated cells.

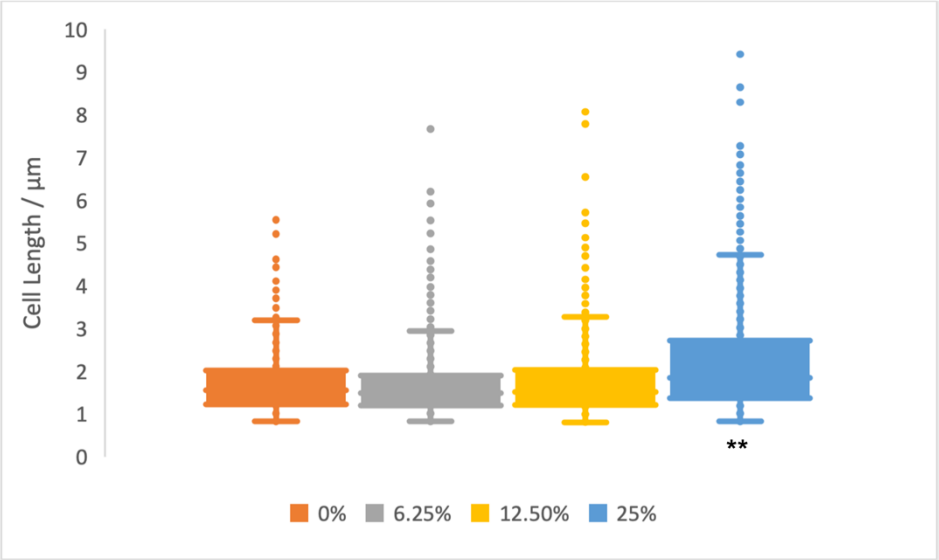

Figure 3.18: Box and whisker plot of the length of E. coli cells when exposed to increasing concentrations of CHA. The bottom of the line is the minimum of the range, the upper line is the maximum of the range with outliers appearing as dots above the maximum, the bottom of the box is the first quartile, the top of the box is the upper quartile with the whole box representing the interquartile range of cell lengths and the line in the centre of the interquartile range the median cell length.

There is evidence for both possible explanations. It has already been established that it is likely membrane disruption is present in the mechanism of action of CHA against *E. coli*. It follows that this could explain the increase in cell size as well as the inhibitory mechanism of action. On the other hand, the hydroxamate unit of CHA is known to bind strongly to Fe(III), it could be deduced that this chelant disrupts bacterial cell division by sequestering these cations, potentially at the specific point of division. This might also fit with previous studies in *E. coli* showing that iron chelators downregulate the transcription of genes involved in division, leading to cell filamentation.[71]

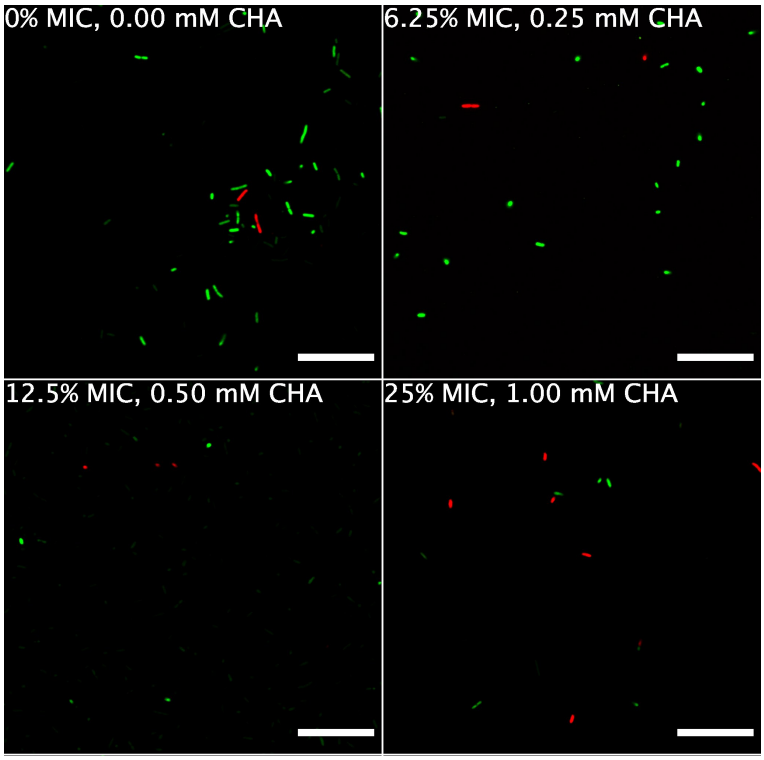

Figure 3.19: Live/Dead staining of S. marcescens exposed to CHA. LSCM images of S. marcescens exposed to 0% MIC, 6.25% MIC, 12.5% MIC and 25% MIC CHA and stained with SYTO9 (green) and PI (red). SYTO9, λ_{ex} = 488 nm, λ_{em} = 500-520 nm. PI, λ_{ex} = 533 nm, λ_{em} = 550-650 nm. Scale bar = 25 µm.

CHA has a similar effect on the membrane of *S. marcescens* as it does on *E. coli* (Figure 3.16B and 3.19). Increasing concentrations of CHA cause a dramatic increase in the number of cells stained with PI suggesting a significant degree of membrane damage. Similarly, the NPN assay indicates that there is minimal disruption to the outer membrane. Although *S. marcescens* and *E. coli* both belong to the family *Enterobacteriaceae*, the Fe(III) transport systems present in *S. marcescens* are known to be complex and unconventional.[72] Differences in susceptibility of bacterial species to different chelants are probably affected by the chemical and structural differences Gram-negative outer membrane constituents. In contrast to *E. coli*, no obvious morphological changes were noted with *S. marcescens* exposed to CHA.

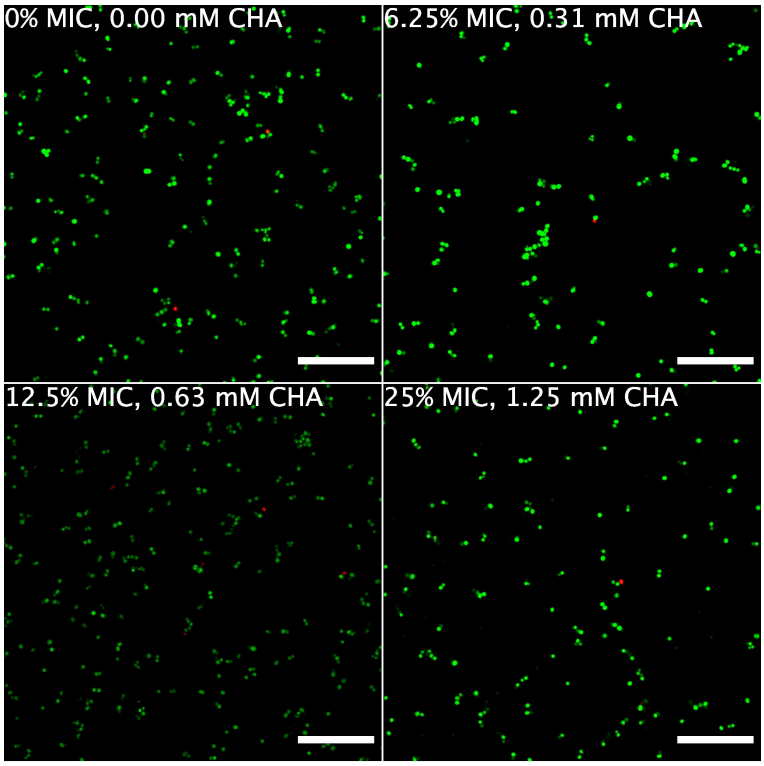

Figure 3.20: Live/Dead staining of S. aureus exposed to CHA. LSCM images of S. aureus exposed to 0% MIC, 6.25% MIC, 12.5% MIC and 25% MIC CHA and stained with SYTO9 (green) and PI (red). SYTO9, λ_{ex} = 488 nm, λ_{em} = 500-520 nm. PI, λ_{ex} = 533 nm, λ_{em} = 550-650 nm. Scale bar = 25 µm.

CHA does not appear to have any detrimental effects on the membrane of *S. aureus* at the concentrations studied (Figure 3.16C and 3.20). There was no increase in the percentage of cells stained as dead when exposed to CHA. There was a slight decrease in the NPN fluorescence intensity when *S. aureus* was exposed to CHA which was unexpected with a Gram-positive species. This could be accounted for by the surfactant qualities of CHA allowing some limited access of NPN to the cytoplasmic membrane. It is possible CHA also acts on *S. aureus* at these concentrations but given Fe(III) is the main metal sequestered by hydroxamates, *S. aureus* may be able to overcome this starvation due to its ability to upregulate genes involved in iron acquisition when faced with nutritional immunity.[73,74]

3.5. Effect of FA on the bacterial cell envelope

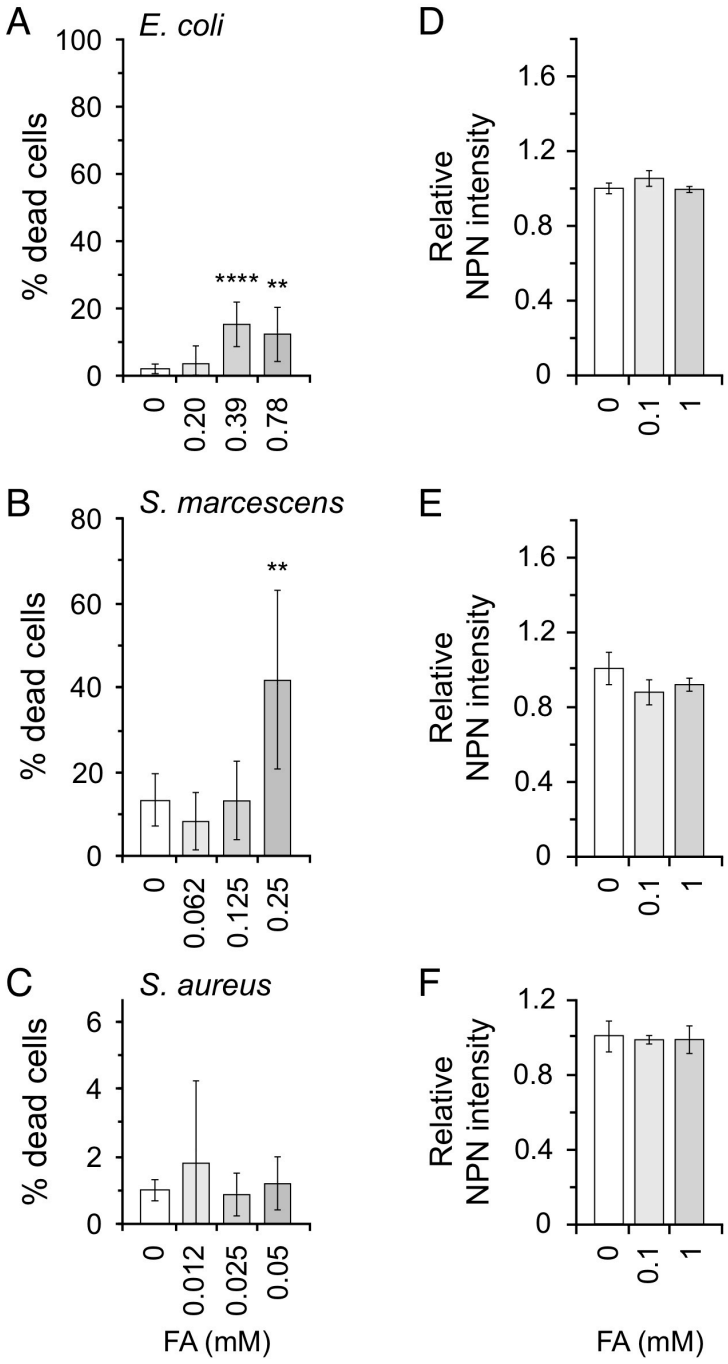

Figure 3.21: The effect of FA exposure on the bacterial cell envelope. Left, damage to inner cell membrane as indicated by the percentage of cells stained as "dead" by PI when exposed to 6.25%, 12.5% and 25% of the MIC of FA in E. coli (A), S. marcescens (B) and S. aureus (C). Right, damage to the outer cell membrane as indicated by the relative intensity of NPN when exposed to 0.1 and 1 mM FA in E. coli (D), S. marcescens (E) and S. aureus (F).

Figure 3.21 shows the effect on the inner and outer membrane of the phytotoxin FA on *E. coli*, *S. marcescens* and *S. aureus* by Live/Dead staining and NPN fluorescence.

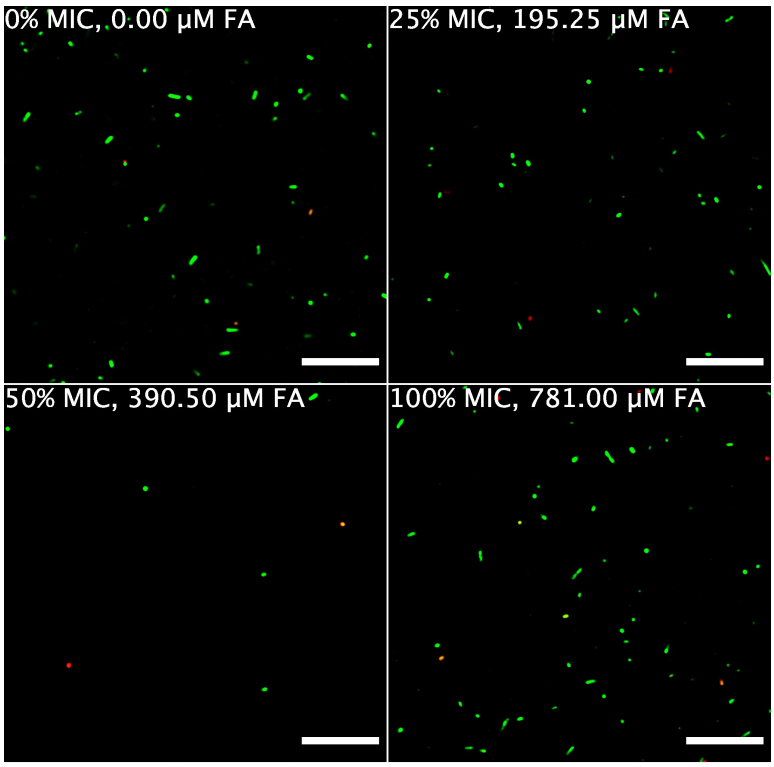

Figure 3.22: Live/Dead staining of E. coli exposed to FA. LSCM images of E. coli exposed to 0% MIC, 6.25% MIC, 12.5% MIC and 25% MIC DTPMP and stained with SYTO9 (green) and PI (red). SYTO9, λ_{ex} = 488 nm, λ_{em} = 500-520 nm. PI, λ_{ex} = 533 nm, λ_{em} = 550-650 nm. Scale bar = 25 µm.

In *P. aeruginosa*, FA results in reductions in cellular concentrations of Fe and Mn.[33] FA does not appear to affect the outer membrane of *E. coli* as evidenced by NPN fluorescence (Figure 3.21A and 3.22). However, FA did increase the number of cells stained with PI and indicative of a compromised membrane. The effects of FA on *E. coli* cellular metal content are not known, although in the Gram-negative species *P.*

protegens, iron deprivation seems to be responsible for its antibacterial mode of action. No morphological changes could be observed with *E. coli* was treated with FA.

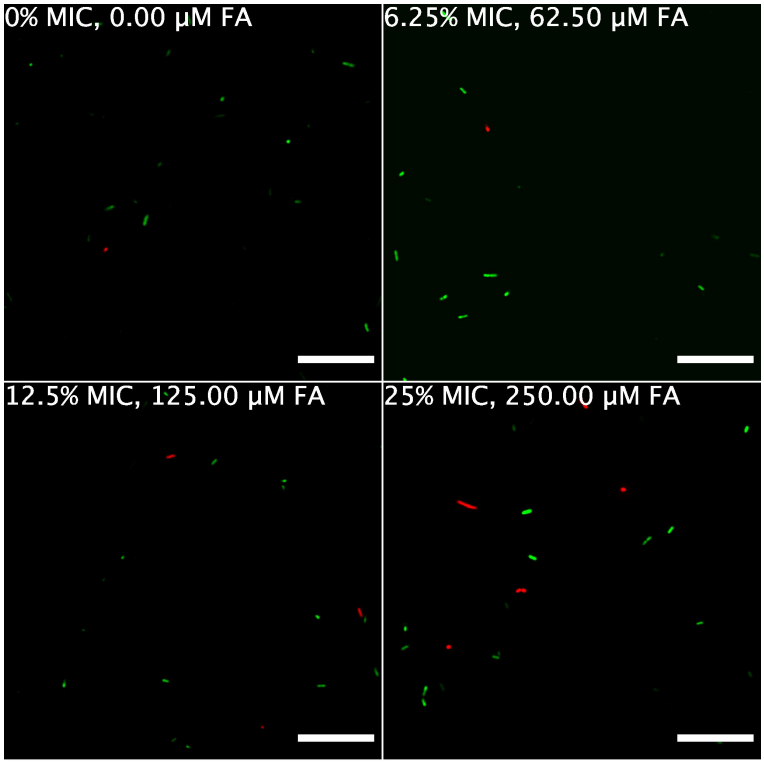

Figure 3.23: Live/Dead staining of S. marcescens exposed to FA. LSCM images of S. marcescens exposed to 0% MIC, 6.25% MIC, 12.5% MIC and 25% MIC DTPMP and stained with SYTO9 (green) and PI (red). SYTO9, λ_{ex} = 488 nm, λ_{em} = 500-520 nm. PI, λ_{ex} = 533 nm, λ_{em} = 550-650 nm. Scale bar = 25 µm.

Figure 3.23 shows LSCM images of *S. marcescens* exposed to FA at various concentrations that inhibit bacterial growth. *S. marcescens* and *E. coli* seem to share a similar membrane damage profile following exposure to FA. The percentage of dead cells increases when the cells are exposed to 25% of the MIC of FA but no obvious damage to the membrane was apparent in NPN assays. It is probable that FA acts on both Gram-negative species by a similar mechanism that does not result in significant

disruption of the outer membrane. No significant morphological changes were noted with *S. marcescens* exposed to FA.

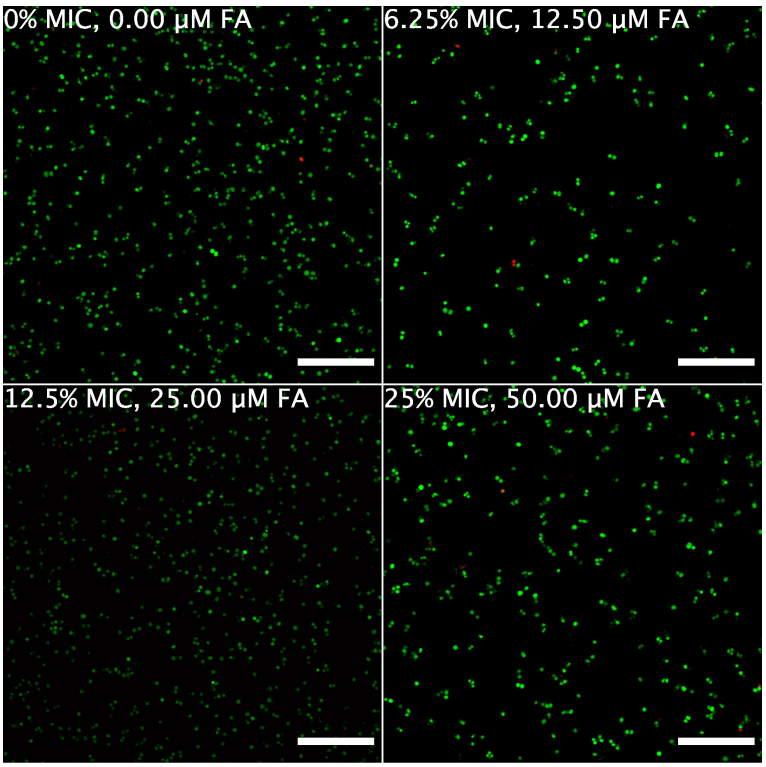

Figure 3.24: Live/Dead staining of S. aureus exposed to FA. LSCM images of S. aureus exposed to 0% MIC, 6.25% MIC, 12.5% MIC and 25% MIC DTPMP and stained with SYTO9 (green) and PI (red). SYTO9, λ_{ex} = 488 nm, λ_{em} = 500-520 nm. PI, λ_{ex} = 533 nm, λ_{em} = 550-650 nm. Scale bar = 25 µm.

Figure 3.24 shows LSCM images of *S. aureus* exposed to FA. FA does not appear to have any effect on the cell envelope of *S. aureus* with increasing concentrations of FA leaving the number of cells stained with PI unchanged. No morphological changes could be observed when *S. aureus* is exposed to FA.

3.6. Effect of TRO on the bacterial cell envelope

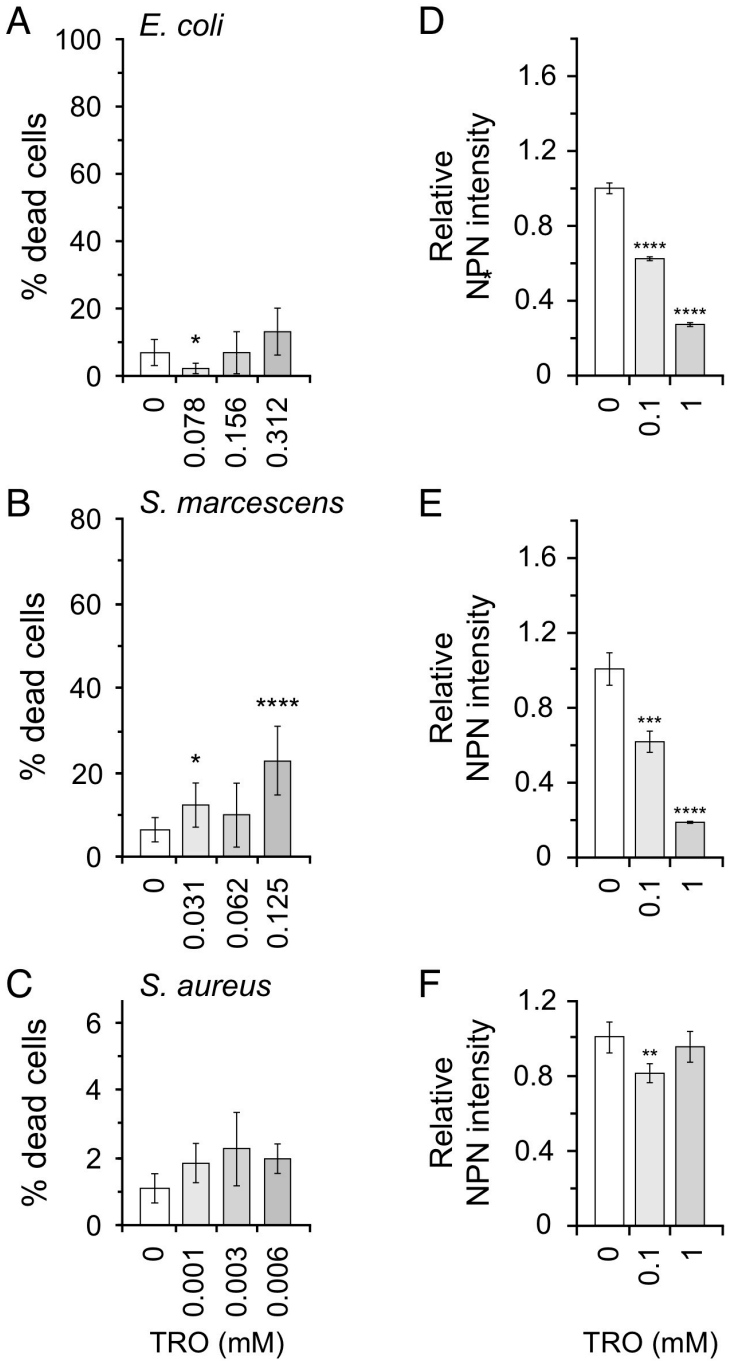

Figure 3.25: The effect of TRO exposure on the bacterial cell envelope. Left, damage to inner cell membrane as indicated by the percentage of cells stained as "dead" by PI when exposed to 6.25%, 12.5% and 25% of the MIC of TRO in E. coli (A), S. marcescens (B) and S. aureus (C). Right, damage to the outer cell membrane as indicated by the relative intensity of NPN when exposed to 0.1 and 1 mM TRO in E. coli (D), S. marcescens (E) and S. aureus (F).

Figure 3.25 shows the effect on the inner and outer membrane of TRO on *E. coli*, *S. marcescens* and *S. aureus* through Live/Dead staining and NPN fluorescence.

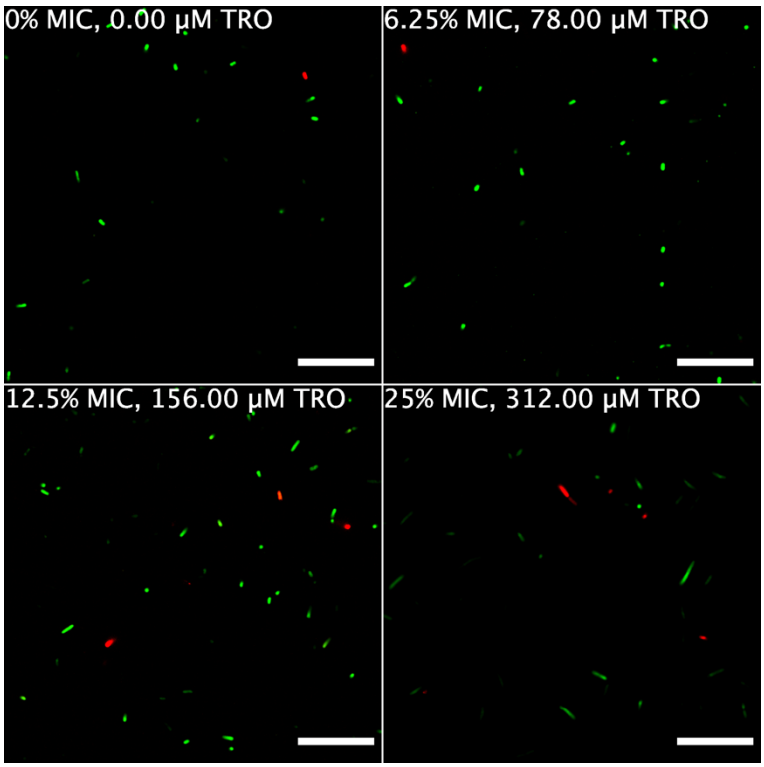

Figure 3.26: Live/Dead staining of E. coli exposed to TRO. LSCM images of E. coli exposed to 0% MIC, 6.25% MIC, 12.5% MIC and 25% MIC DTPMP and stained with SYTO9 (green) and PI (red). SYTO9, λ_{ex} = 488 nm, λ_{em} = 500-520 nm. PI, λ_{ex} = 533 nm, λ_{em} = 550-650 nm. Scale bar = 25 µm.

Figure 3.26 shows LSCM images of *E. coli* exposed to TRO. The results from Live/Dead staining indicate that at these sub-MIC concentrations the outer membrane is not disrupted based on measurements of the number of cells stained with PI. The decrease in number of cells stained as dead at 6.25% of the MIC, although statistically significant, is more likely to be an error or variability rather than a genuine result given the data for higher concentrations.

TRO resulted significant morphological changes to *E. coli* with the average cell length increasing when exposed to TRO at 25% of the MIC. Figure 3.27 shows a box and whisker plot of the length of *E. coli* cells when exposed to increasing MIC fractions of TRO. For concentrations of TRO at 6.25% and 12.5% the MIC of TRO for *E. coli* there was no marked alteration in cell length, however, there was at the highest (25% MIC) concentration. As noted above with *E. coli* and CHA there are two likely explanations for the increase in cell length: membrane disruption and inhibition of cell division. Given there does not appear to be any damage to the cell envelope it is more likely that the increase in cell length is caused by disruption to normal cell division, lengthening the time it takes to divide and producing longer daughter cells.

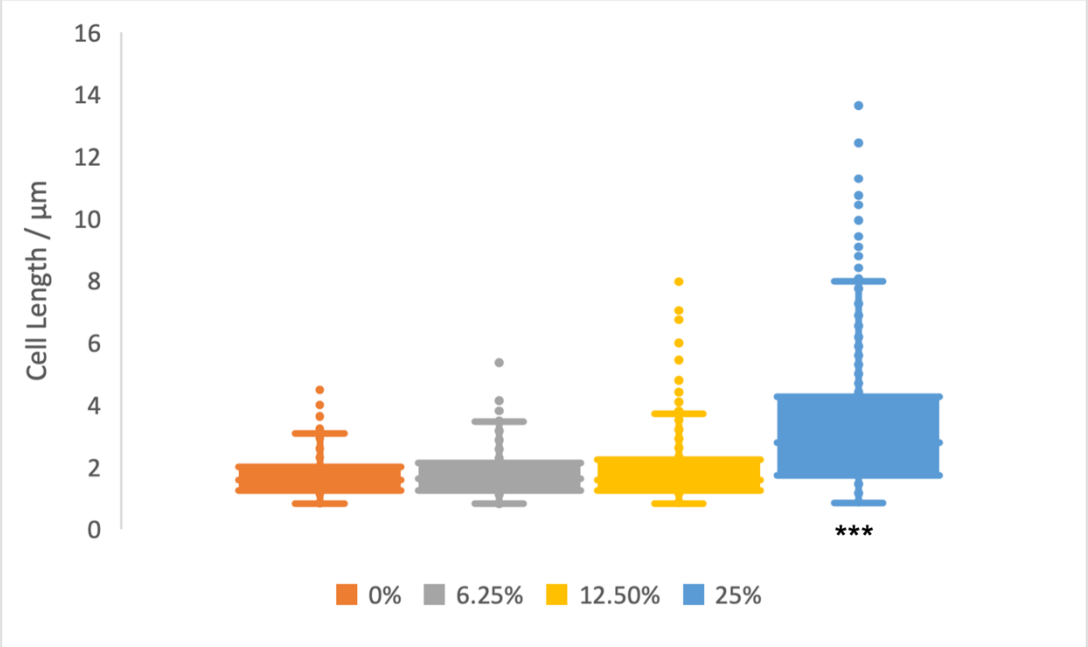

Figure 3.27: Box and whisker plot of the length of E. coli cells when exposed to increasing concentrations of TRO. The bottom of the line is the minimum of the range, the upper line is the maximum of the range with outliers appearing as dots above the maximum, the bottom of the box is the first quartile, the top of the box is the upper quartile with the whole box representing the interquartile range of cell lengths and the line in the centre of the interquartile range the median cell length.

Although there is limited information concerning the antibacterial mechanism of TRO, it has been shown to be an inhibitor of metalloenzymes by antagonistically binding the metal cofactor of these enzymes.[75,76] This indicates that TRO is able to enter cells and act intracellularly, most likely sequestering metals once inside the cell and reducing their availability. It is therefore feasible that TRO interacts with a metalloenzyme inside the cell involved in the cell division process, rendering it less effective and inducing cell filamentation.

In support of the argument TRO acts intracellularly rather than sequestering metals outside the cell reducing availability is the data from the NPN fluorescence assay. Surprisingly, TRO caused a decrease in fluorescence in the NPN assay. Given that NPN fluorescence increases when the outer membrane, specifically its fluidity, is perturbed, follows that a decrease in NPN fluorescence might indicate an increase in the integrity of the outer membrane. A strengthened outer membrane is counterintuitive, although it is possible that TRO somehow prevents access to the outer membrane, or indeed blocks or inhibits porins that normally allow NPN access to the envelope. However, a more likely scenario is the possibility that NPN fluorescence is affected by the internal redox environment of the bacterial cell and this enhanced reductive intracellular environment reduces the intensity of NPN fluorescence.[77–81] If this is correct, it might be expected that TRO chelates metals such as Fe(III), particularly in the cytosol, reducing its availability. The oxidation status of the cell in response to chelant exposure will be explored in a later chapter of this thesis.

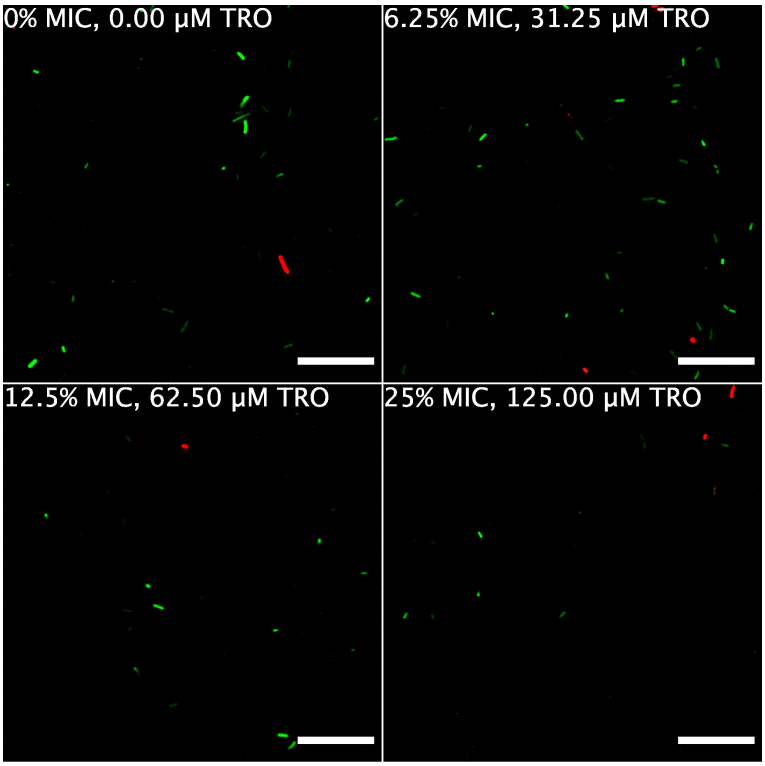

Figure 3.28: Live/Dead staining of S. marcescens exposed to TRO. LSCM images of S. marcescens exposed to 0% MIC, 6.25% MIC, 12.5% MIC and 25% MIC DTPMP and stained with SYTO9 (green) and PI (red). SYTO9, λ_{ex} = 488 nm, λ_{em} = 500-520 nm. PI, λ_{ex} = 533 nm, λ_{em} = 550-650 nm. Scale bar = 25 µm.

Figure 3.28 shows LSCM images of *S. marcescens* exposed to TRO. TRO shows an equivalent effect on NPN fluorescence with *S. marcescens* as it does with *E. coli*, the fluorescence intensity decreases as the TRO concentration increases. The Live/Dead staining indicates that unlike with *E. coli*, TRO does cause some damage to the cell envelope of *S. marcescens*, allowing PI to enter the cell. Although both are Gram-negative within the *Enterobacterales* order, there are significant differences in their cell envelope composition, particularly the integral membrane proteins that may allow TRO damage the *S. marcescens* membrane but not that of *E. coli*. Unlike with *E. coli*, there were no morphological changes to *S. marcescens* when TRO was added to cells.

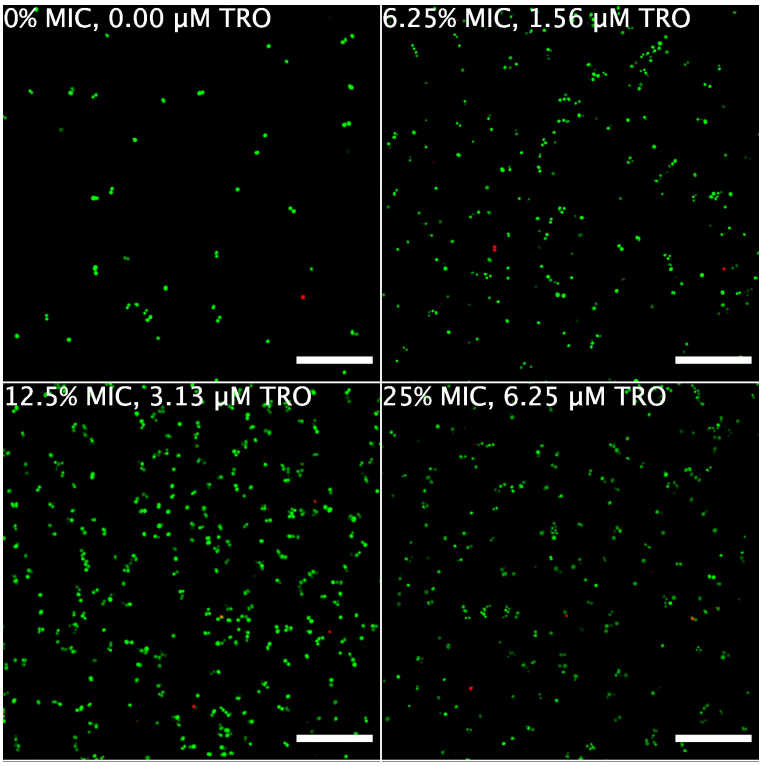

Figure 3.29: Live/Dead staining of S. aureus exposed to TRO. LSCM images of S. aureus exposed to 0% MIC, 6.25% MIC, 12.5% MIC and 25% MIC DTPMP and stained with SYTO9 (green) and PI (red). SYTO9, λ_{ex} = 488 nm, λ_{em} = 500-520 nm. PI, λ_{ex} = 533 nm, λ_{em} = 550-650 nm. Scale bar = 25 µm.

Figure 3.29 shows LSCM images of *S. aureus.* TRO does not appear to have any effect on the cell envelope of *S. aureus* with increasing concentrations failing to change the proportion of cells stained with PI. Although there appears to be a slight increase in the number of dead cells present, this increase is not statistically significant. No morphological changes were found with TRO-treated *S. aureus* cells.

3.7. Effect of HNK on the bacterial cell envelope

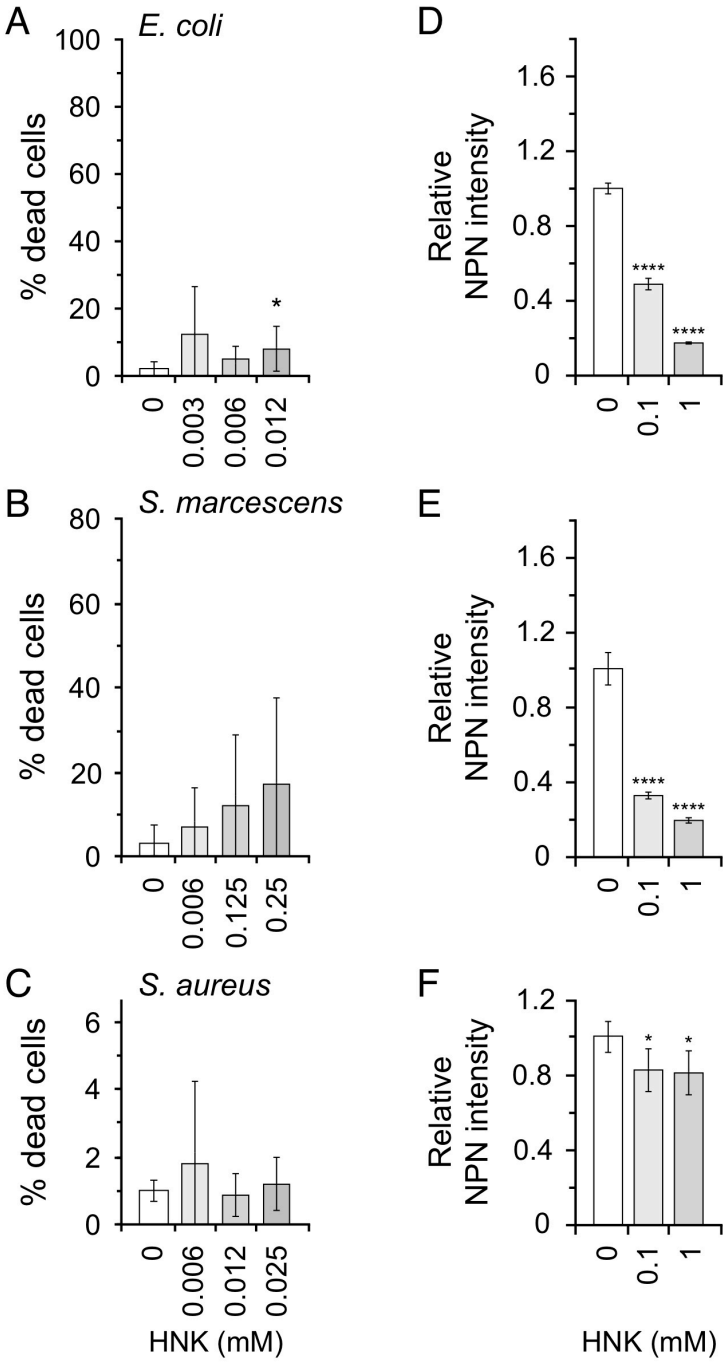

Figure 3.30: The effect of HNK exposure on the bacterial cell envelope. Left, damage to inner cell membrane as indicated by the percentage of cells stained as "dead" by PI when exposed to 6.25%, 12.5% and 25% of the MIC of HNK in E. coli (A), S. marcescens (B) and S. aureus (C). Right, damage to the outer cell membrane as indicated by the relative intensity of NPN when exposed to 0.1 and 1 mM HNK in E. coli (D), S. marcescens (E) and S. aureus (F).

Figure 3.30 shows the effect on the inner and outer membrane of HNK on *E. coli*, *S. marcescens* and *S. aureus* through Live/Dead staining and NPN fluorescence.

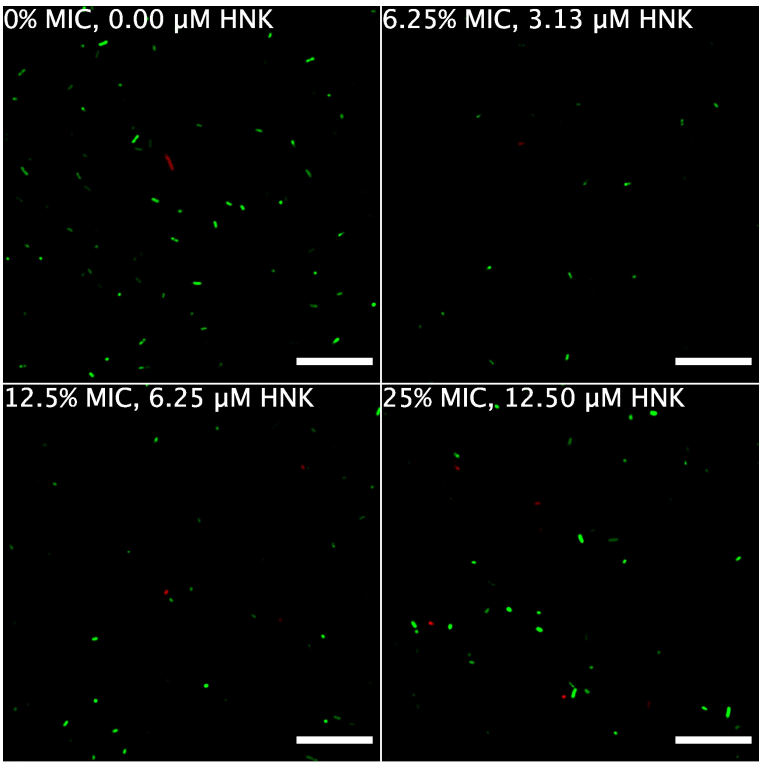

Figure 3.31: Live/Dead staining of E. coli exposed to HNK. LSCM images of E. coli exposed to 0% MIC, 6.25% MIC, 12.5% MIC and 25% MIC DTPMP and stained with SYTO9 (green) and PI (red). SYTO9, λ_{ex} = 488 nm, λ_{em} = 500-520 nm. PI, λ_{ex} = 533 nm, λ_{em} = 550-650 nm. Scale bar = 25 µm.

Figure 3.31 shows LSCM images of *E. coli* exposed to HNK. The effects of HNK on the *E. coli* cell envelope was similar to those observed for TRO, apart from the absence of the morphological changes with HNK; no prevalence of cells with increased length were apparent with the latter. Little change in the percentage of cells stained as dead by PI were found, suggesting limited cell envelope damage occurs. Previous studies using electron microscopy had indicated that no major envelope changes occur when

E. coli and *S. aureus* are exposed to HNK. [82] This study suggested that the mode of action of HNK against *E. coli* and *S. aureus* was due to inhibition of cellular respiration.[82] This fits with the proposed intracellular sequestration of metal cations essential as metalloenzyme cofactors.

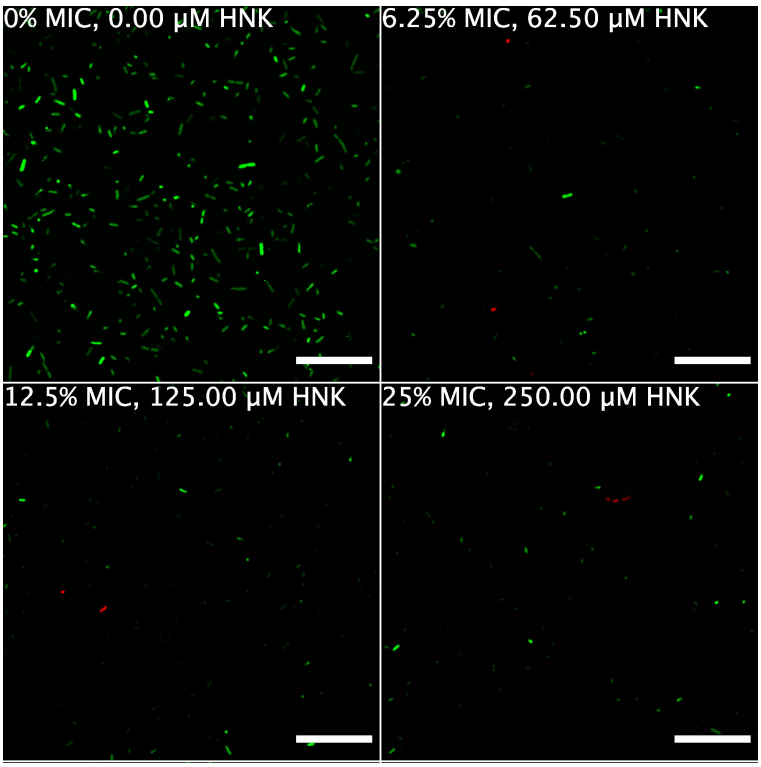

Figure 3.32: Live/Dead staining of S. marcescens exposed to HNK. LSCM images of S. marcescens exposed to 0% MIC, 6.25% MIC, 12.5% MIC and 25% MIC DTPMP and stained with SYTO9 (green) and PI (red). SYTO9, λ_{ex} = 488 nm, λ_{em} = 500-520 nm. PI, λ_{ex} = 533 nm, λ_{em} = 550-650 nm. Scale bar = 25 µm.

Figure 3.32 shows LSCM images of *S. marcescens* exposed to HNK at 0 µM, 62.5 µM, 125 µM, and 250 µM which are 0%, 6.25%, 12.5% and 25% the MIC.

As with *E. coli*, the effect of HNK on *S. marcescens* reflected its similarity to TRO. There did not appear to be any damage to the cell envelope caused by HNK, based on

Live/Dead staining, although the marked decrease in NPN fluorescence intensity was evident (Figure 3.30E). No morphological changes were apparent when *S. marcescens* was exposed to HNK.

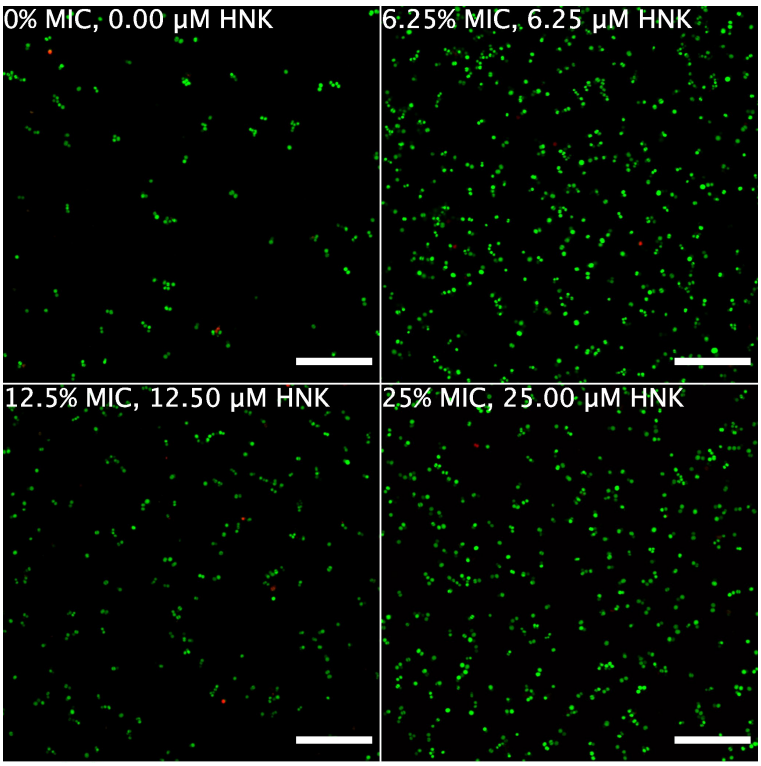

Figure 3.33: Live/Dead staining of S. aureus exposed to HNK. LSCM images of S. aureus exposed to 0% MIC, 6.25% MIC, 12.5% MIC and 25% MIC DTPMP and stained with SYTO9 (green) and PI (red). SYTO9, λ_{ex} = 488 nm, λ_{em} = 500-520 nm. PI, λ_{ex} = 533 nm, λ_{em} = 550-650 nm. Scale bar = 25 µm.

Figure 3.33 shows LSCM images of *S. aureus* exposed to HNK at 0 µM, 6.25 µM, 12.5 µM, and 25 µM which are 0%, 6.25%, 12.5% and 25% the MIC. HNK does not appear to have a significant effect on the cell envelope of *S. aureus,* with increasing concentrations not altering the number of cells stained with PI. There was a modest decrease in NPN fluorescence, although not as extreme as seen with the two Gram-

negative species (Figure 3.30F). No morphological changes were observed when *S. aureus* was treated with HNK.

3.8 Conclusions and Future Work

This work shows that chelating agents have a varied impact on the membrane integrity of bacteria depending on the chemistry of the chelant and the species it is affecting. Overall, most chelants investigated disrupted the cell envelope of bacteria at some level and this may be the outer membrane, inner membrane, or both membranes that are damaged. Some chelating agents were found to induce morphological changes on some bacteria studied, namely an overall decrease in cell size.

Further investigations could be carried out to determine whether the thickness of the bacterial cell envelope is affected by exposure to chelants, either by cryoTEM or for a higher throughput technique, LSCM imaging of Nile Red stained cells which only stains the membrane of the cells.

Furthermore, additional investigations could be carried out into the damage induced in the inner membrane of using O-Nitrophenyl-β-D-galactopyranoside (ONPG). ONPG cannot cross the inner membrane unless it has been permeabilised but once it does it can be converted by β-lactamase to β-D-galactose and o-nitrophenol. Both ONPG and β-D-galactose are colourless but o-nitrophenol is slightly yellow in colour ($\lambda_{max} \approx$ 480 nm) allowing the degree of inner membrane damage to be tracked by absorption.

Similarly outer membrane damage could also be investigated using an absorption technique based on β-lactamase using the compound nitrocefin. Nitrocefin is colourless until it is degraded by β-lactamase and shows a red colour ($\lambda_{max} \approx 500$ nm) which can be detected by absorption. Both of these experiments would provide additional information on the effect of chelants on the bacterial cell envelope, but both are not as sensitive as the two techniques used; absorption is not as sensitive as fluorescence because absorption is a bulk process requiring many molecules for detection, whereas fluorescence is a single molecule process allowing for a much lower limit of detection. Additionally, these experiments require strains which express β-lactamase.

The membrane potential could also be investigated using $DiOC_3$ which shows a bathochromic shift in fluorescence from green to red when the molecule aggregates. This aggregation can occur when the polarisation of the membrane changes resulting in the compound able to travel across the membrane in one direction but not return because of the charge on the compound. With this experiment being fluorescence based and not absorption, the limit of detection would be low so any changes in membrane polarisation could readily be detected.

4. Effects of Chelants on the Bacterial Intracellular Redox Environment

4.1. Reactive Oxygen Species in Bacteria

Reactive oxygen species (ROS) include superoxide anion radical, (O_2^-) hydrogen peroxide (H_2O_2) and hydroxyl radicals (·OH), formed through a series of one electron reduction of molecular oxygen. Although these species can be highly damaging to macromolecules in bacteria they are nonetheless used by bacteria as signalling molecules.[83,84] Bacteria have evolved mechanisms to tightly regulate the amount of ROS being generated inside the cell to ensure they maintain their viability. Bacteria cannot stop the production of ROS inside the cell because it is a non-biological process where transition metals catalyse the formation of ROS. Since bacteria require transition metals for various processes as cofactors and inclusion in metalloenzymes, they cannot stop the production of ROS without having a deficiency of essential transition metal ions.

Bacteria have uptake systems, siderophores and haem-uptake systems, that tightly regulate iron levels to maintain homeostasis. Poorly regulated iron uptake would lead to an increase in intracellular free iron concentration. The redox activity of iron catalyses the Haber-Weiss reaction (equation 4.3) which is the sum of two redox reactions of iron, the kinetically slow reduction of ferric ions into ferrous ions by superoxide (equation 4.1), and the Fenton reaction (equation 4.2) in which ferrous ions are converted back to the ferric form by hydrogen peroxide. This leads to an

overall reaction of hydrogen peroxide and superoxide being converted to hydroxyl radicals, hydroxide ions and molecular oxygen. The hydroxyl radical is short lived but rapidly reacts to causes oxidative damage to lipids, proteins, and DNA. This damage activates cell death processes, through regulated pathways, apoptosis. The Fe(III) can be reduced by superoxide to regenerate Fe(II), enabling a continuous Fenton reaction.[85,86] Under aerobic conditions, a Fenton-like reaction, involving the redox cycling between Cu(I)/Cu(II), generates hydroxyl radicals, shown in Equation 4.4, leading to a similar catalytic cycle.[87]

$$Fe^{3+} + \cdot O_2^- \rightarrow Fe^{2+} + O_2 \qquad \text{Equation 4.1}$$

$$Fe^{2+} + H_2O_2 \rightarrow Fe^{3+} + \cdot OH + OH^- \qquad \text{Equation 4.2}$$

$$\text{Net reaction: } H_2O_2 + \cdot O_2^- \rightarrow \cdot OH + OH^- + O_2 \qquad \text{Equation 4.3}$$

$$Cu^{+} + H_2O_2 \rightarrow Cu^{2+} + OH^{\cdot} + OH^- \qquad \text{Equation 4.4}$$

Any change in the available concentration of these metal ions inside the cell or sequestration of them by chelants outside of the cell, therefore reducing availability to the cell, will have an effect on the generation of ROS and therefore the homeostasis of the cell which could affect viability.

4.2. Reactive Oxygen Species Detection

2′,7′-dichlorofluorescin diacetate (DCFH-DA) was used to investigate the intracellular oxidative environment when the bacteria are exposed to chelants.[88] DCFH-DA is a non-fluorescent molecule that upon encountering reactive oxygen species (ROS) generated inside cells, becomes fluorescent, figure 4.1. The presence of acetyl groups in DCFH-DA assists cell penetration and once in the cytosol these groups are acted upon by various deacetylases that generate 2′,7′-dichlorofluorescin (DCFH); inclusion of the acetyl groups is essential since unmodified DCFH is unable to passively diffuse across lipid bilayers unless facilitated by an active transport mechanism.[89,90] Hence, DCFH, which is not fluorescent, is oxidised by ROS to the fluorescent molecule 2′,7′-dichlorofluorescein (DCF).

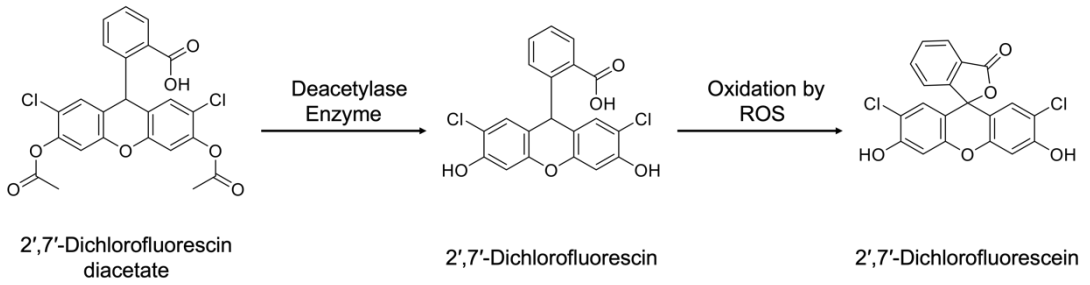

Figure 4.1: Structure of DCFH-DA, DCFH and DCF and the steps involved to exhibit fluorescence when exposed to ROS inside cells.

DCF displays a fluorescence profile typical of fluorescein derivatives as shown in Figure 4.2.

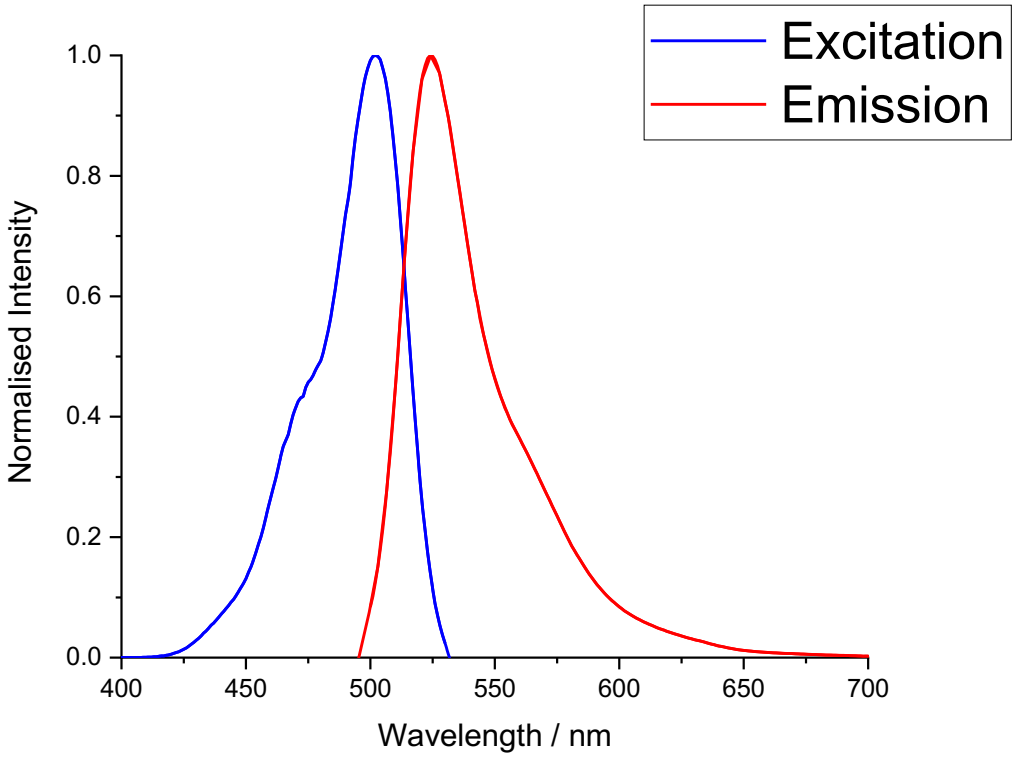

Figure 4.2: Excitation and emission spectra of 2',7'-dichlorofluorescein in ethanol. For the excitation spectrum (blue line) the λ_{em} = 560 nm. For the emission spectrum (red line) the λ_{ex} = 470 nm.

DCFH-DA was initially developed as a probe to detect hydrogen peroxide production in cells.[91] However, it was demonstrated that several enzymes were able to convert DCFH to DCF *in cellulo* suggesting that it could also be converted by other reactive oxygen species in addition to hydrogen peroxide. The DCFH to DCF conversion can in fact be mediated by hydroxy radicals, peroxy radicals and reactive nitrogen species, nitric oxide and peroxynitrite.[92–95] DCFH-DA is thus an effective and sensitive probe for detection of a range of oxidative stresses inside cells.

The protocol and timeline for the DCFH-DA assay used to investigate ROS generation inside bacterial cells following chelant exposure is shown in Figure 4.3. Importantly,

DCFH-DA must be added at the same time as the chelants of interest to allow time for the probe to be taken up by cells and for ROS to convert it into its fluorescent form.

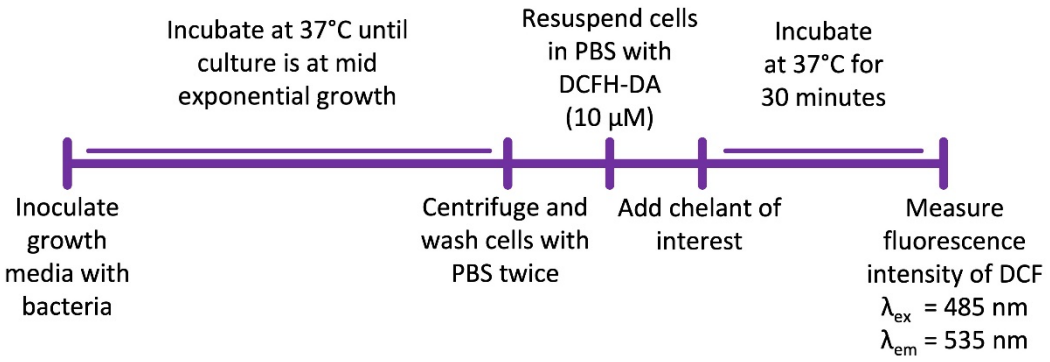

Figure 4.3: Reactive oxygen species detection assay protocol timeline.

4.3. Microscopical Validation

To establish that this methodology is effective at detecting changes in the intracellular redox environment and not externally in the surrounding media, the assay was initially evaluated using laser scanning confocal microscopy. Control experiments were performed with all chelants tested on *E. coli*.

Control experiments were carried out with the cells alone, cells with the probe added and cells with the probe plus hydrogen peroxide (H_2O_2) to induce excess ROS generation. Cells harvested at mid-log exponential growth were incubated with (or without in the first case) the probe for 30 minutes at a concentration of 10 µM. For the third control, H_2O_2 was added at a sub-lethal (<1 mM[66]) concentration of 10 µM

and incubated for a further 10 minutes before imaging. Figure 4.4 shows microscope images of these control experiments.

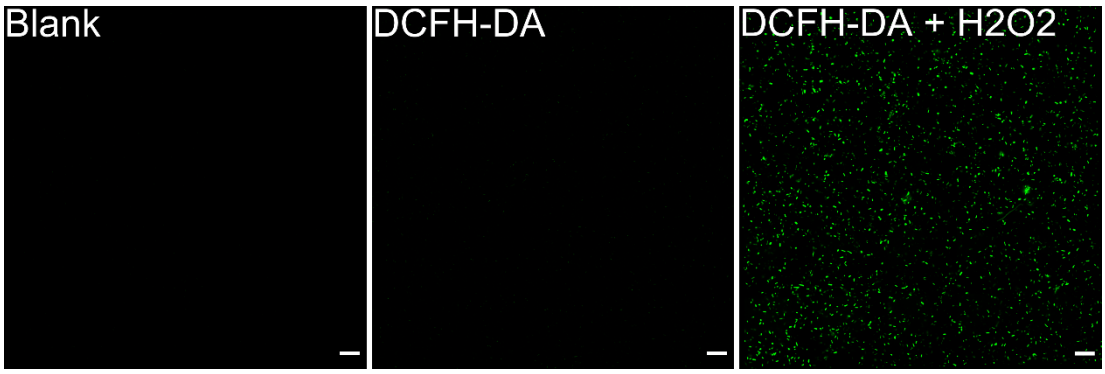

Figure 4.4: Microscope images of control experiments of DCFH-DA as a ROS probe in E. coli. From left to right, cells with nothing added, cells with 10 µM DCFH-DA added and cells with 10 µM DCFH-DA and 10 µM H_2O_2 added. λ_{ex} = 476 nm, λ_{em} = 500-650 nm. Scale bar = 25 µm.

It is clear that addition of hydrogen peroxide causes a large increase in DCF fluorescence. To quantify this an intensity profile plot of each image is shown in figure 4.5. Here the mean 8-bit gray value of each x-axis position is plotted for each image. It shows not only is there an increase in fluorescence intensity of the experiment with addition of hydrogen peroxide but also there is some residual fluorescence for the image with just the probe present. This is because there is some DCFH being converted into DCF inside the cell from endogenous ROS. We can use this as a baseline to see whether the fluorescence intensity increases or decreases indicating more or less ROS production inside the cell respectively.

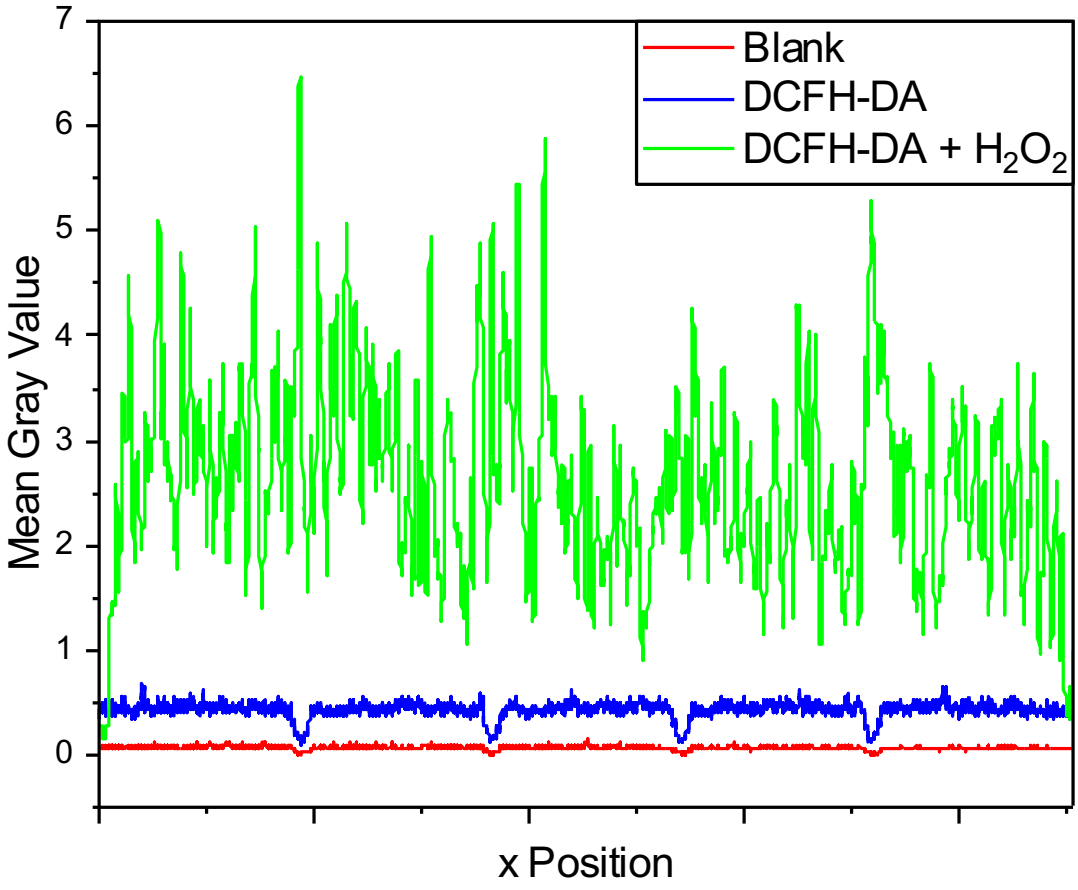

Figure 4.5: Intensity profile plot of DCFH-DA assay control experiments. Cells with nothing added in red, cells with DCFH-DA added in blue and cells with DCFH-DA and H_2O_2 added in green.

4.4. Results and Discussion

The six chelants of interest were investigated for their effect on the Gram-negative species *E. coli* and *S. marcescens* and the Gram-positive species *S. aureus*. Three fixed concentrations were investigated: 0.1, 1 and 10 mM. The concentrations were purposefully not matched to the MIC of each chelant species pair because commercial use of a chelant as an antimicrobial would not be discriminate and should expect to be broad spectrum. The three concentrations investigated because they broadly represented sub-MIC, peri-MIC, and post-MIC concentrations for most of the chelant species pairs.

The MIC for *S. aureus* for all the chelants investigated is lower than that of the two Gram-negative species used. This means that a statistically significant change in the DCF fluorescence intensity at a lower concentration is more indicative of a ROS concentration increase or decrease than a result at a higher concentration. If there is only a statistically significant change in the intensity of DCF fluorescence at a higher concentration of chelant used, especially if it only exists at 10 mM, this may not be indicative of any real ROS generation or reduction changes. A trend across all three concentrations investigated could indicate that there is a change in ROS concentration even if the results are not as statistically significant as others.

4.4.1. Effect of EDTA on the Redox Environment inside Bacteria

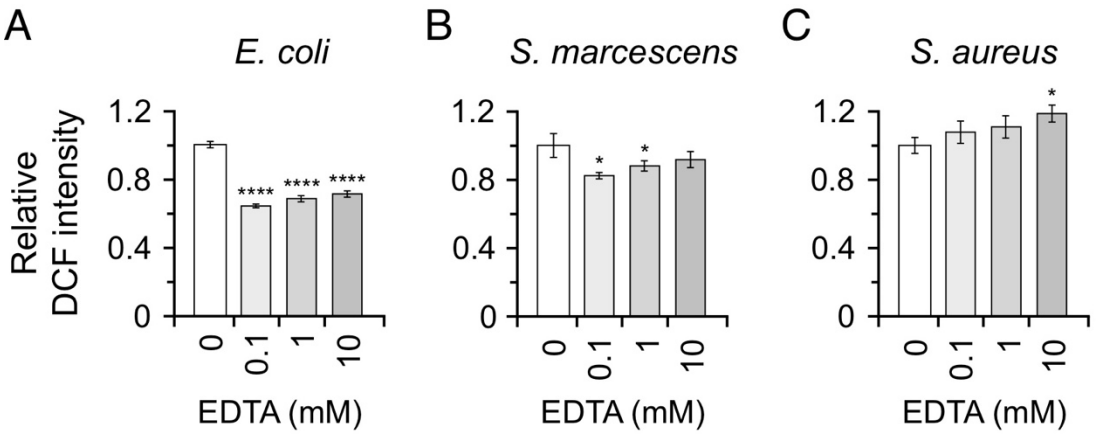

Figure 4.6: Effect of EDTA exposure on the redox environment inside cells. Redox environment in bacteria cells as indicated by the relative fluorescence intensity of DCF when exposed to 0.1 and 1 and 10 mM EDTA in E. coli (A), S. marcescens (B) and S. aureus (C).

In *E. coli* EDTA reduces the oxidative stress on cells as indicated by a reduction in the fluorescence intensity of DCF compared to the control. Given EDTA's strong affinity for iron this is to be expected as there would be less iron available for the cell to use to produce ROS with through the Fenton reaction. This provides evidence for EDTA working extracellularly binding to iron and its bacteriostatic mechanism being metal starvation.

In *S. marcescens* there is a similar trend as seen in *E. coli* indicating that a similar mechanism of action between the two species exists with both being Gram-negative so many of their biological pathways are similar. The reduction in DCF fluorescence intensity is not as high as in *E. coli* so this common mechanism may not be the main mechanism of action against *S. marcescens,* and an additional pathway also exists such as more membrane damage rather than metal sequestration.

In contract to the two Gram-negative species, the Gram-positive species *S. aureus* does not appear to decrease ROS generation in the cell. There appears to be an upward trend in DCF fluorescence intensity and at 10 mM there is a statistically significant increase in the intensity of DCF fluorescence indicating more ROS generation. However, given this concentration is very high compared to the MIC of EDTA of this species it may be that a significant proportion of cells are dying and there may be some other mechanism that is oxidising the DCFH to DCF and increasing the relative fluorescence intensity.

4.4.2. Effect of DTPMP on the Redox Environment inside Bacteria

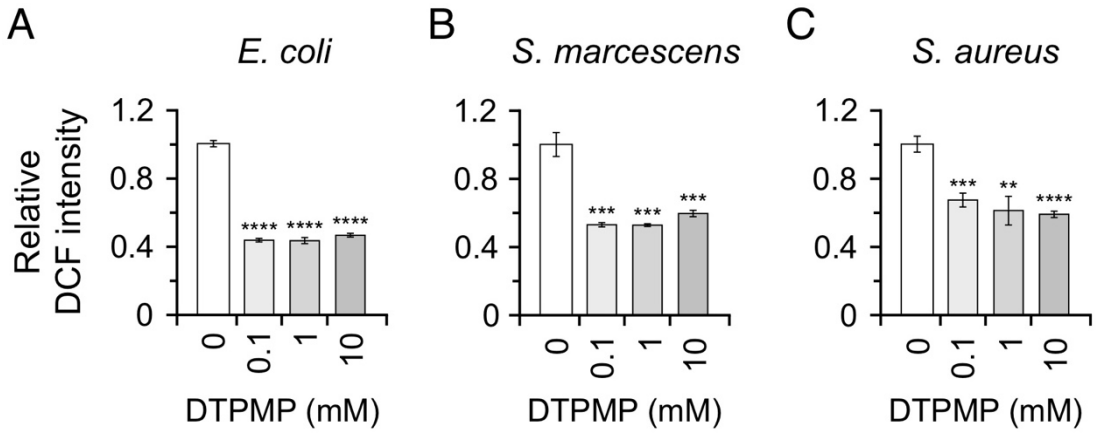

Figure 4.7: Effect of DTPMP exposure on the redox environment inside cells. Redox environment in bacteria cells as indicated by the relative fluorescence intensity of DCF when exposed to 0.1 and 1 and 10 mM DTPMP in E. coli (A), S. marcescens (B) and S. aureus (C).

DTPMP has similar chemistry to EDTA and ROS assay results are like it for the two Gram-negative species. In *E. coli* the intensity of DCF fluorescence is reduced by over half. As with EDTA this could indicate that the chelant is sequestering metals used by

the cell to produce ROS such as iron and the bacteria are not able to produce ROS as efficiently as they otherwise would be. This is evidence for the chelant being active extracellularly and not crossing the membrane and acting internally.

In contrast to the effect of EDTA on *S. marcescens*, DTPMP does affect the amount of ROS inside bacteria by a significant amount. Similar to *E. coli*, the amount of ROS inside cells is reduced by approximately half as indicated by a reduction in the intensity of DCF fluorescence by about half relative to the control. It may be that DTPMP has a stronger affinity for iron (and other metals used in ROS generation) than EDTA has.

DTPMP also decreases the concentration of ROS in *S. aureus* unlike EDTA. The reduction in DCF fluorescence intensity it statistically significant at the lowest concentration tested, 0.1 mM. This is below the MIC for DTPMP with *S. aureus* so this indicates the reduction is present even when the cell is still able to grow, albeit at a reduced rate. This trend carries on for the post-MIC concentrations of DTPMP so it clearly is a significant part of the mechanism of action of DTPMP against *S. aureus*.

DTPMP acts consistently across all species, probably by sequestering metal ions outside of the bacterial cell, starving it of the necessary cofactors to produce reactive oxygen species. This in addition to the evidence of damage to the cell membrane makes DTPMP a potent antibacterial agent.

4.4.3. Effect of CHA on the Redox Environment inside Bacteria

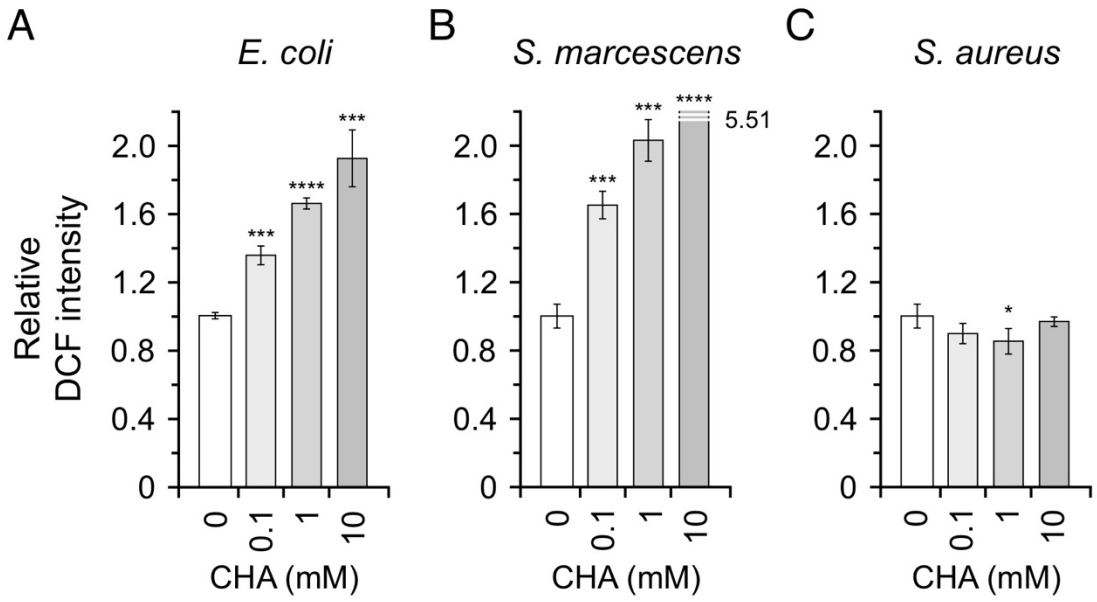

Figure 4.8: Effect of CHA exposure on the redox environment inside cells. Redox environment in bacteria cells as indicated by the relative fluorescence intensity of DCF when exposed to 0.1 and 1 and 10 mM CHA in E. coli (A), S. marcescens (B) and S. aureus (C).

CHA affects Gram-negative species differently to all other chelants tested. In both *E. coli* and *S. marcescens* there was a large increase in the relative intensity of DCF fluorescence indicating an increase in the concentration of ROS inside the bacterial cells. In *E. coli*, at 10 mM the relative DCF fluorescence intensity doubled and in *S. marcescens* the relative intensity increased five-fold.

Given this large increase it is clear that there is something about the chemistry and structure of CHA that causes this effect. As already detailed, CHA has a structure resembling a surfactant: a polar hydroxamate head and a non-polar seven membered carbon chain tail. This suggests it could locate itself in the membrane of the bacteria, particularly the outer membrane of Gram-negative species as this is more accessible

and the CHA does not have to surpass an energy barrier to pass through the outer membrane, peptidoglycan and inner membrane or any combination thereof. Hydroxamates are strong chelators of iron. It is possible that the hydroxamate group chelates iron extracellularly and locates itself in the outer membrane. The iron is then much more readily available to the bacteria to uptake through mechanisms such as siderophore capture since siderophores bind more strongly to metal ions than individual chelants owing to the chelate effect and the reduction in entropy associated with it.

The increase in ROS generation may have a different cause but the result remains the same, the large increase in ROS generation will cause irreversible damage to DNA, proteins and other macromolecules in the bacterial cell which will cause the cell to lose its viability, possibly its ability to reproduce and will eventually die.

In contrast to the two Gram-negative species, *S. aureus* does not display the same increase in ROS generation as evidenced by there being no change in the intensity of DCF fluorescence. This supports the initial theory that the CHA is located in the outer membrane of the Gram-negative species because Gram-positive species like *S. aureus* do not have an outer membrane for the surfactant like molecule to interact with.

4.4.4. Effect of FA on the Redox Environment inside Bacteria

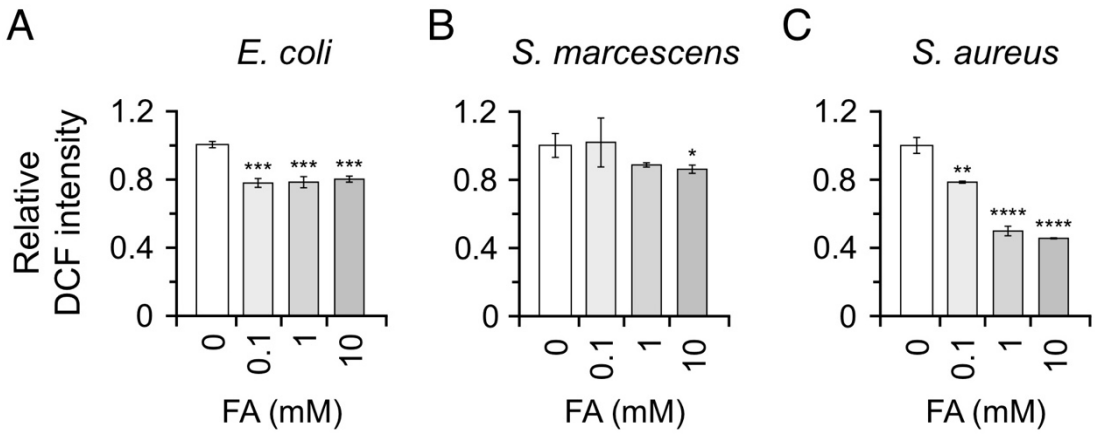

Figure 4.9: Effect of FA exposure on the redox environment inside cells. Redox environment in bacteria cells as indicated by the relative fluorescence intensity of DCF when exposed to 0.1 and 1 and 10 mM FA in E. coli (A), S. marcescens (B) and S. aureus (C).

The two Gram-negative species investigated display a decrease in the amount of ROS generated by the bacteria as shown by the decreased intensity of DCF fluorescence. This effect is more apparent in *E. coli*, compared to *S. marcescens*, with a drop of 20% intensity for all concentrations tested. In *S. marcescens* there is no drop in intensity for 0.1 and 1 mM concentrations but at 10 mM there is a reduction of 20% intensity. This could imply that there needs to be a critical concentration of FA to start affecting the ROS generation of *S. marcescens* which is higher than that required for *E. coli*.

As with the previous chelants where a reduction in ROS generation was observed, this could be explained by sequestration of metal ions, particularly iron, which does not allow for ROS to be generated within the bacterial cell.

FA does have an effect on the redox environment of *S. aureus* showing a decrease in the fluorescence intensity of DCF when exposed to all concentrations of FA tested. The effect gets stronger moving from 0.1 mM to 1 mM but does not change moving to 10 mM indicating a limit to the effect of FA against *S. aureus*.

4.4.5. Effect of TRO on the Redox Environment inside Bacteria

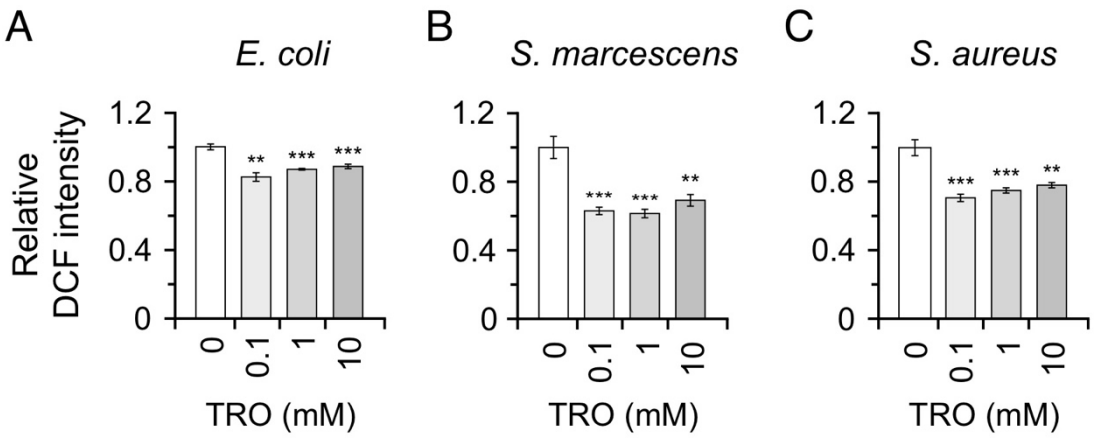

Figure 4.10: Effect of TRO exposure on the redox environment inside cells. Redox environment in bacteria cells as indicated by the relative fluorescence intensity of DCF when exposed to 0.1 and 1 and 10 mM TRO in E. coli (A), S. marcescens (B) and S. aureus (C).

TRO affects all the species tested in a similar way by reducing the amount of ROS generated as indicated by the reduction in the intensity of DCF fluorescence.

In *E. coli* the amount of ROS generated decreases by approximately 20% across all concentrations tested. In *S. marcescens* the amount of ROS generated decreases by approximately 40% when exposed to TRO at all concentrations tested. The amount of ROS generated in *S. aureus* when exposed to TRO decreases by approximately 40% for all concentrations tested.

The mechanism of action for TRO could be different to EDTA, DTPMP and FA where the proposed mechanism is iron starvation in the extracellular media and reduced generation of ROS inside the cell. TRO has been shown to have antioxidant properties by being oxidised itself as a protective agent.[46,47,96] The amount of ROS generated could be at the same whether or not the bacteria are exposed to TRO. However, once TRO is present, the amount of DCFH that is oxidised to DCF by ROS would be reduced because the TRO is also oxidised. This implies that TRO could have a small protective effect to the bacteria, but this is outweighed by any negative effects it also has such as membrane damage.

4.4.6. Effect of HNK on the Redox Environment inside Bacteria

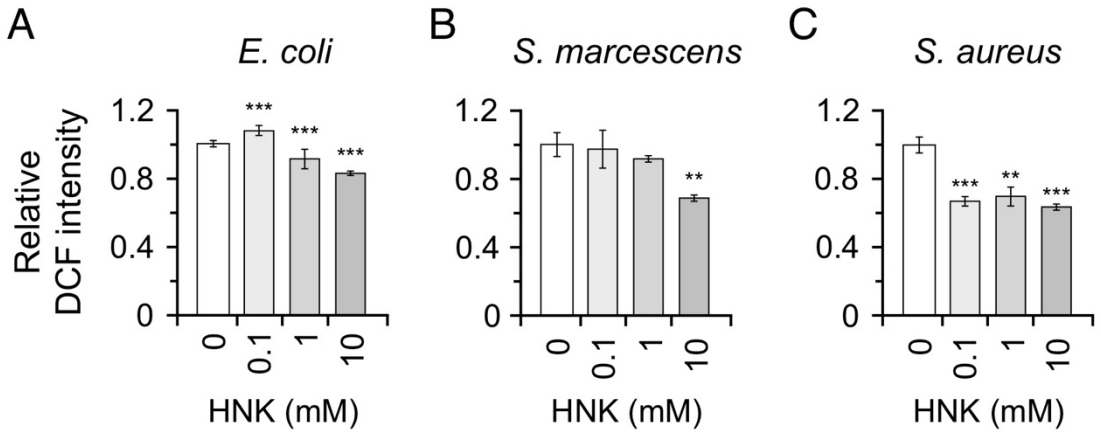

Figure 4.11: Effect of HNK exposure on the redox environment inside cells. Redox environment in bacteria cells as indicated by the relative fluorescence intensity of DCF when exposed to 0.1 and 1 and 10 mM HNK in E. coli (A), S. marcescens (B) and S. aureus (C).

Although HNK has a similar structure to TRO (same structure with the addition of an isopropyl group) its effect on the three species of bacteria tested does not correspond to the effect of TRO.

In *S. aureus* the effect of HNK is the same as that of TRO, a reduction in ROS by approximately 40% as indicated by a reduction in the intensity of DCF fluorescence. This suggests that HNK could act through a similar mechanism to TRO in *S. aureus*, possibly by the antioxidant effect proposed earlier.

In the two Gram-negative species tested the change in intensity of DCF fluorescence does not follow the same pattern as with TRO. Both species do exhibit a reduction in DCF fluorescence intensity when exposed to 10 mM of HNK but not as significant as with TRO. It could be that HNK is not as effective as an antioxidant as TRO is at the concentrations tested or it may be that the antibacterial mechanism of action is different even though their structures are similar.

5. Morphology of *S. aureus* mutants

5.1. Introduction

To understand the mechanism of action of any antimicrobial, including chelants, against bacteria it can be beneficial to understand how the bacteria develop resistance to the antimicrobial. Bacteria that have been exposed to an antimicrobial at a concentration that would normally inhibit its growth and yet continue to grow will likely have some level of tolerance. This tolerance could have come from a mutation in a gene that encodes a protein that is targeted by the antimicrobial. Alternatively, the mutation could result in upregulation of a gene product confers some protection against the antimicrobial, or it might potentially cause downregulation of a gene that gives the bacteria a disadvantage against the antimicrobial.

Previous work isolated eight mutated strains of *S. aureus* that were exposed to sub-lethal concentrations of EDTA and DTPMP and have had their genomes investigated to determine which mutations are present.[33] Subsequent analysis by transmission electron microscopy (TEM) revealed that many of these mutated strains have aberrations in cell division and other morphological changes affecting the cell wall. TEM has the benefit of providing a very high resolution (~0.2 nm)[97], however, sample preparation involves toxic compounds, is difficult to adapt as a high-throughput technique and can produce artefacts due to sample preparation. LSCM, on the other hand, lends itself to being a high-throughput technique with rapid sample preparation and data acquisition. The reduced resolution compared to TEM limits the

conclusions that can be drawn from LSCM, but the resolution is sufficient to evaluate the size and shape of bacteria.

5.2. Isolated mutant strains

Two sets of *S. aureus* mutants were isolated that showed resistance to EDTA and/or DTPMP. *S. aureus* FDA209P was used to generate the mutants, it is a methicillin susceptible strain, and its complete genome is available.[98] The bacteria were exposed to EDTA or DTPMP for 15 or 29 days and a single colony selected, grown and frozen stocks retained. The mutant strains are detailed in table 5.1.

Strain	Chelant Exposed To	Concentration and Duration
JN170	EDTA	0.1 mM, 15 days
JN206		0.1 mM, 29 days
JN207		0.1 mM, 29 days
JN174	DTPMP	1 mM, 15 days
JN208		1 mM, 15 days; 2 mM, 14 days
JN209		1 mM, 15 days; 2 mM, 14 days
JN210		1 mM, 29 days
JN212		1 mM, 29 days

Table 5.1: Chelant resistant mutant strains of S. aureus and the conditions used to generate them.

The isolated mutant strains were tested for resistance to both EDTA and DTPMP compared with the wild type and all strains were found to have increased resistance

to both chelants, irrespective of which chelant they were exposed to generate their mutations. This indicates a common mechanism is present between the two chelants as resistance to one imparts some resistance to the other. The genomes of each mutant strain were sequenced and compared with the wildtype to determine which mutations were present. The mutations present are detailed in figure 5.1.

		EDTA			DTPMP				
	Day isolated:	15	29	29	15	29	29	29	29
Gene	Function	JN170	JN206	JN207	JN174	JN208	JN209	JN210	JN212
fnbA	Fibronectin-binding protein A	T510K	T510K	T510K	T510K	T510K	T510K	T510K	T510K
sasG1	Surface protein G1								E407*
sasG2	Surface protein G2	▲▼■			▲▼■			▲▼■	▲▼■
sdrD	Calcium binding protein			T463I					
sbi	Immunoglobulin-binding protein					P241L			
1331	Quinolone resistance transporter							T291I	
2055	Glycine betaine transporter					A131V			
qoxA	Quinol oxidase subunit II							▲▼■	▲▼■
388	Lipase/esterase								T111*fs*
1745	Arginine ABC transporter							P157L	P157L
vraF	Antibiotic ABC transporter					Q8*	Q8*		
arcD	Arginine/ornithine antiporter	M189I	M189I	M189I	M189I	M189I	M189I	M189I	M189I
1546	Membrane-bound protein	T39M	T39M	T39M	T39M	T39M	T39M	T39M	T39M
fmtA	D-Ala teichoic acid esterase	Q109*	Q109*	Q109*					
pbp2	Penicillin-binding protein 2	L53F	L53F	L53F	S147L	Q232H	Q232H	A146V	A146V
614	AraC transcriptional regulator							H7Y	H7Y
2355	Hypothetical protein								D33V
1454	Probable RNA helicase	F107Y							
ahpF	Alkyl hydroperoxide reductase							P131V	
aroB	3-dehydroquinate synthase							K165N	
aroC	Chorismate synthase							D158N	
butA	Oxidoreductase					A143E			
dinB	DNA polymerase IV							▲▼■	
lysC	Aspartate kinase					F218Y			
bsaA1	Glutathione peroxidase							▲▼■	
citZ	Citrate synthase						▲▼■		
2122	Truncated transposase							A114T	
t0048	tRNA-Ile		▲▼■	▲▼■	▲▼■				
r0012	23S ribosomal RNA						▲▼■	▲▼■	▲▼■
r0015	23S ribosomal RNA	▲▼■							
r0003	5S ribosomal RNA			▲▼■					

Surface proteins | Cell wall synthesis | Transposases, tRNA and rRNA
Membrane transporters | Others | ▲▼■ Upstream mutations

Figure 5.1: Mutations present in the eight chelant resistant mutant S. aureus strains.[33]

There are some mutations that are present in all the isolated strains which are noteworthy because they are likely to be responsible for the strain developing

resistance. These include amino acid substitutions in FnbA (fibronectin binding protein), ArcD (an arginine:ornithine antiporter), PBP2 (penicillin binding protein 2) and 1546 (an uncharacterised membrane bound protein). Additional mutations of interest included stop codons disrupting *fmtA*, encoding a teichoic acid esterase present in all three EDTA-resistant strains, and *vraF* that encodes an antibiotic efflux pump found in JN208 and JN209, two of the strains selected against DTPMP.

Interestingly many of the mutations found are in genes relating to the membrane and cell wall of the bacteria. In a previous chapter it was established that DTPMP acts on the cell envelope of *S. aureus*, but EDTA does not have as much of an effect. This provides evidence that EDTA may also act on the cell envelope of *S. aureus* as well as DTPMP.

Unpublished data from cryoTEM experiments on the chelant exposure derived mutant strains suggests that there is significant disruption to the morphology of cells when compared to the wild type.

This disruption includes changes to the cross-sectional area of the cells imaged, which indicates a change in the overall size of the cells. There is also disruption in the membrane of the cells with changes in the thickness of the cell wall and the shape that it adopts. There are anomalies where the cell wall protrudes into the cell and folds back on itself, so it does not adhere to a spherical shape. There are also changes to the amount of aggregation between cells with some strains exhibiting more close clustering and some exhibiting less.

CryoTEM is able to deliver a much higher resolution than LSCM, but the sample preparation and other experimental factors do not lend to it being a high throughput technique. To achieve this high throughput need for cell morphology analysis, LSCM was used to assess the morphology of the cells on a larger scale.

5.3. *S. aureus* mutant morphology analysis using LSCM

LSCM was employed to quantify any changes to the shape, size, and aggregation capabilities of the mutant strains on a larger, more representative scale. The wild type *S. aureus* and the mutant strains were all grown to their mid-exponential growth phase in LB media, pelleted by centrifugation and washed in PBS. Cells were then stained with the DNA stain, Hoechst 33342, the excitation, and emission spectrum of which is shown in figure 5.2.

While imaging all parameters were kept consistent, such as laser power, gain, pinhole size and scan speed to ensure comparisons could be made across the image series. To analyse the images from LSCM, firstly direct observations were made. Looking at the arrangement of the cells can provide information on the surface of the cell wall. Wild type *S. aureus* usually presents as small grape-like clusters of a few bacteria stuck together. If the bacteria form larger clusters, it may be that there is a change on the surface of the cell wall that encourages aggregation. Conversely, if the bacteria appear mostly as individual cells or freshly divided diplococci only it may be that there is a change in the cell wall surface that discourages proximity to another cell. Both

provide insight into how the mutations that are present are affecting the cell and what the implications are for the mechanism of action of the chelants.

The images were also analysed by measuring the cell size. Fiji (v1.53q)[61] was used to determine cell dimensions using the analyse particles feature. This detects individual particles which have 8-bit intensity values over a certain threshold and are between predetermined sizes and provides measurements for all the particles. Assumptions must be made when making these measurements and as such some error is introduced. Firstly, a size range for the software to detect the bacteria must be determined. In this work, based on experience and visual inspection of the images generated, a minimum area of 9 pixels (based on an absolute minimum size of 3x3 pixels) for each particle was adopted with no upper limit. 9 pixels corresponds to an area of 0.729 μm^2 based on the imaging parameters used. Secondly, an assumption is made that all the cells represent perfect spheres, which may not be the case, but this assumption is necessary for comparability across images and strains. Rather than an area of the cell, a volume is estimated based on the average radius of the shortest and longest diameter across the cell. Finally, it is assumed that each cell in the field is at its maximal diameter. The section thickness for the parameters used was 0.772 µm which is larger than the typical diameter of a *S. aureus*. Given the cells that are imaged are located on the surface of the coverslip so should all be in the same plane we can assume that the maximum diameter has been captured whilst imaging.

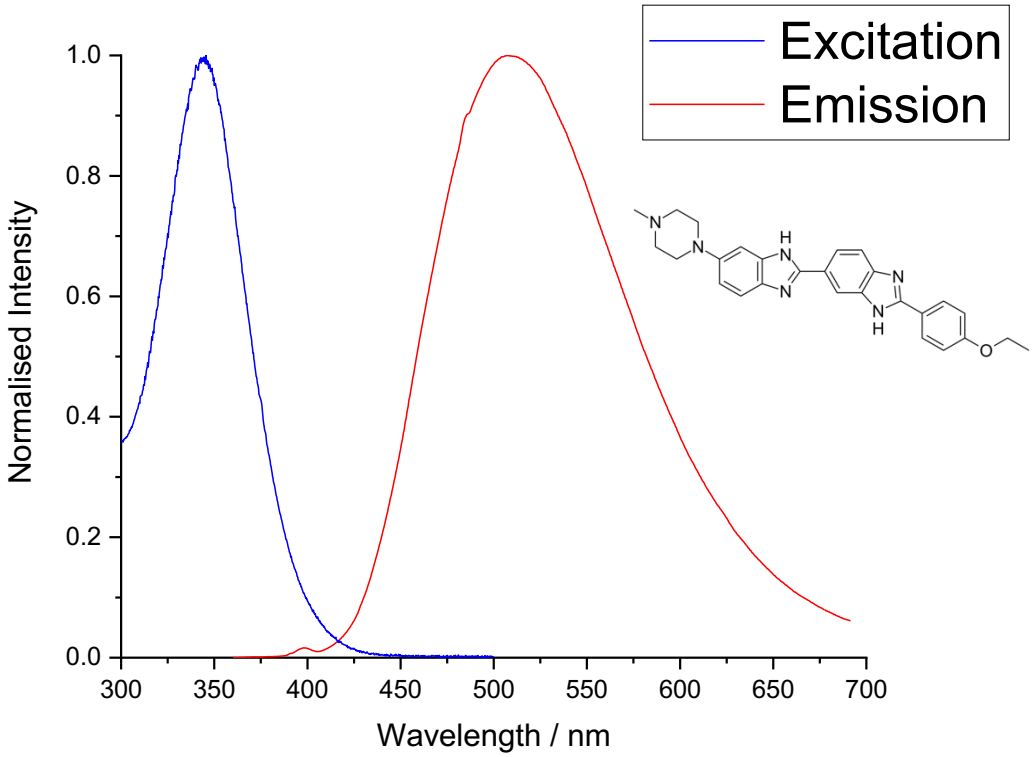

Figure 5.2: Excitation and emission spectra of Hoechst 33342 in water. For the excitation spectrum (blue line) the λ_{em} = 620 nm. For the emission spectrum (red line) the λ_{ex} = 480 nm. The structure of Hoechst 33342 is shown to the right.

To obtain as robust representative values as possible the imaging was repeated extensively to obtain size measurements for thousands of individual bacteria of each strain.

Figure 5.3 shows a representative image of the wild type of *S. aureus* stained with Hoechst 33342 while Figure 5.4 shows representative images of the mutant strains derived from exposure to EDTA, JN170, JN206 and JN207. Figure 5.5 shows representative images of the mutant strains derived from exposure to DTPMP, JN174, JN208, JN209, JN210 and JN212.

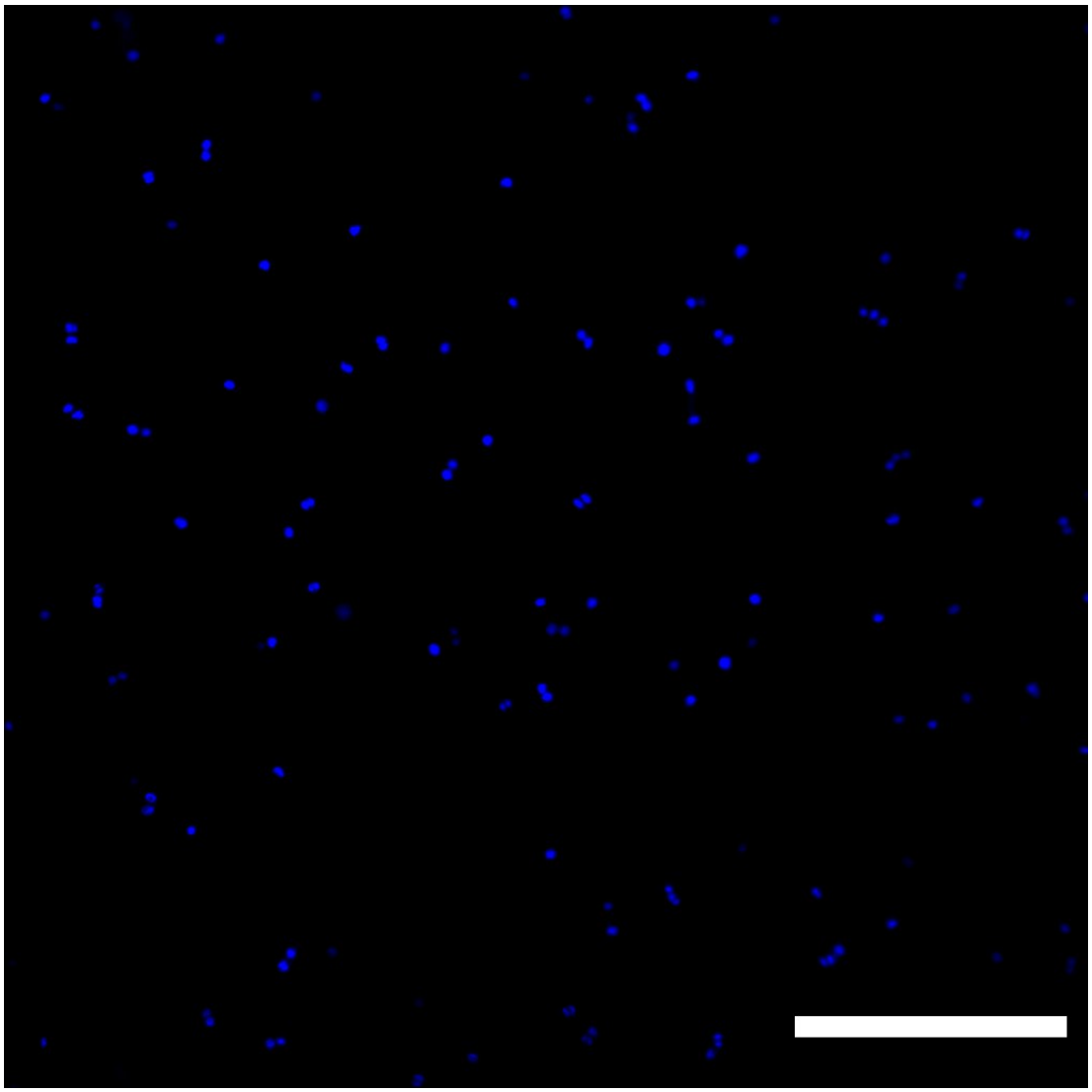

Figure 5.3: Wild type S. aureus stained with Hoechst 33342. λ_{ex} = 355 nm, λ_{em} = 450-600 nm. Scale bar = 25 µm.

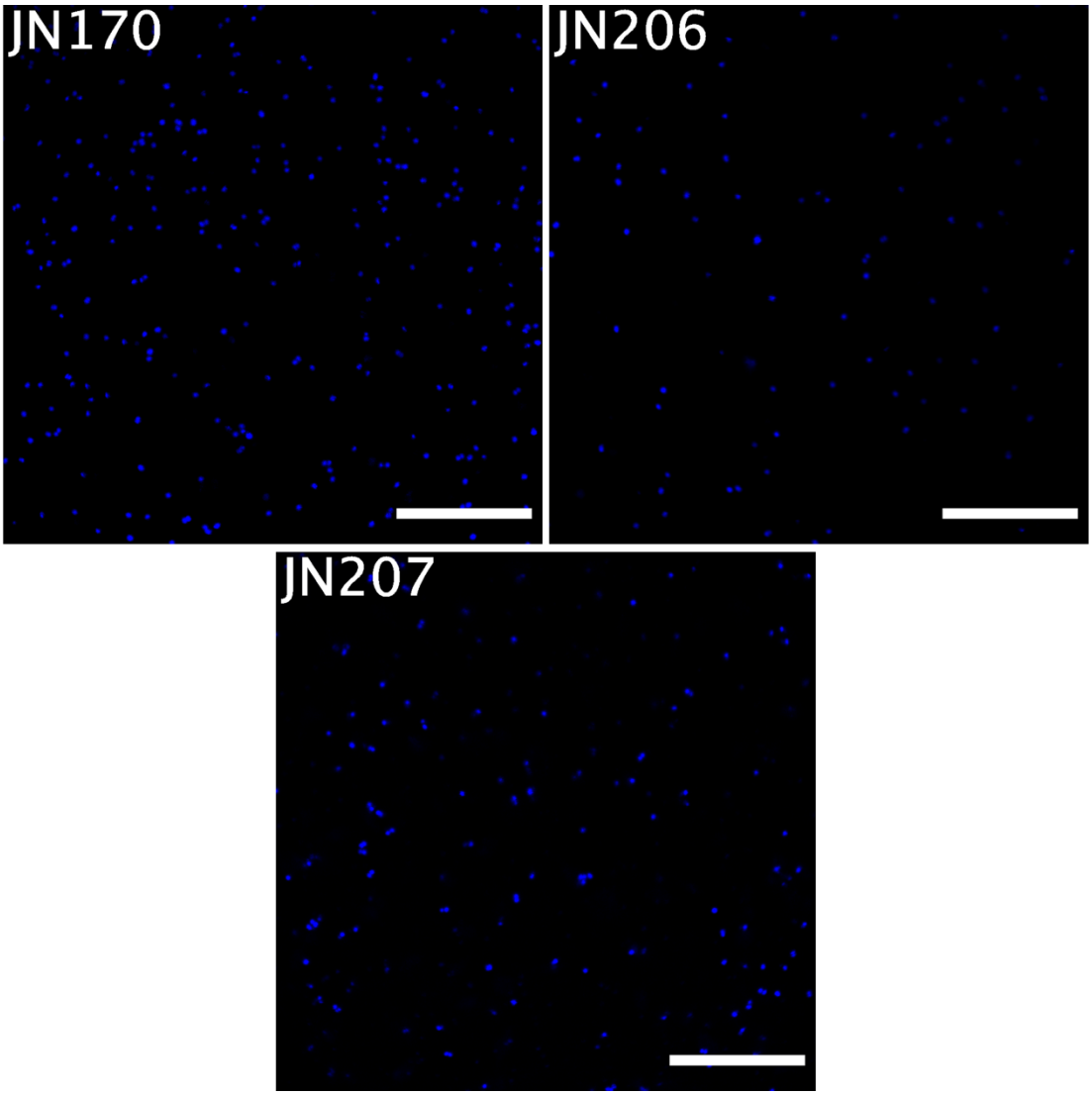

Figure 5.4: S. aureus mutant strains obtained from exposure to EDTA stained with Hoechst 33342. λ_{ex} = 355 nm, λ_{em} = 450-600 nm. Scale bar = 25 µm.

Table 5.2 summarises the results of the size measurements on the wild type and all mutant strains and highlights the strains which have a reduction in overall size: JN170, JN206, JN207, JN208 and JN209. This is better visualised in figure 5.5 which is a box and whisker plot of the size measurements for the wild type and each mutant strain.

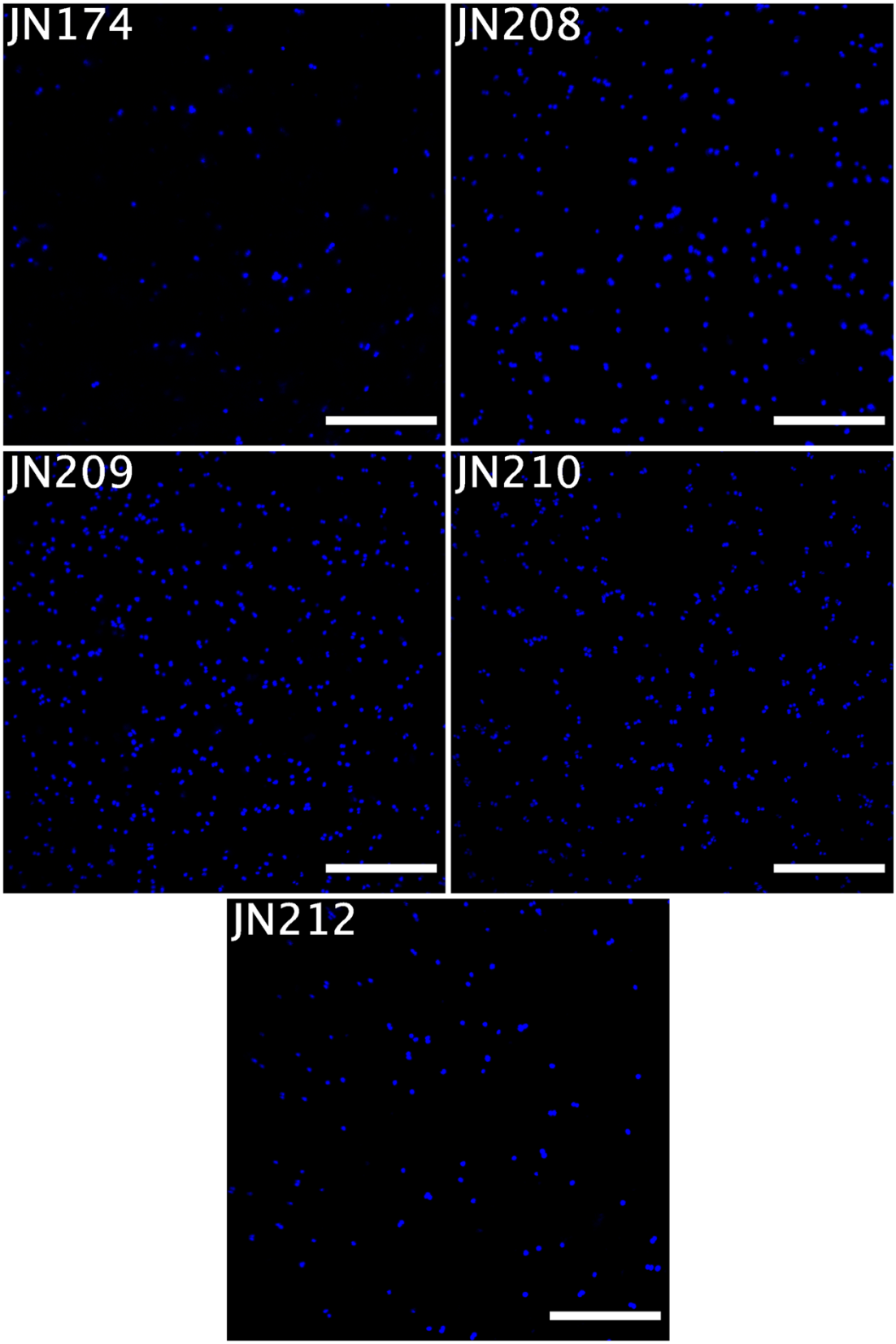

Figure 5.5: S. aureus mutant strains obtained from exposure to DTPMP stained with Hoechst 33342.

λ_{ex} = 355 nm, λ_{em} = 450-600 nm. Scale bar = 25 µm.

Strain	Chelant Exposed to	Cells Measured	Mean Volume / μm^3	Standard Deviation / μm^3
wt	N/A	5966	0.85	0.36
JN170	EDTA	9348	0.41	0.23
JN206		4673	0.22	0.22
JN207		14327	0.52	0.30
JN174	DTPMP	7416	0.84	0.34
JN208		8240	0.33	0.20
JN209		13339	0.63	0.38
JN210		7844	0.94	0.54
JN212		5261	0.87	0.36

Table 5.2: Statistical data from size measurements of S. aureus mutant strains. The wild type strain is highlighted in grey and any strains which showed a statistically significant reduction in cell size are highlighted in red. No cells showed an increase in size.

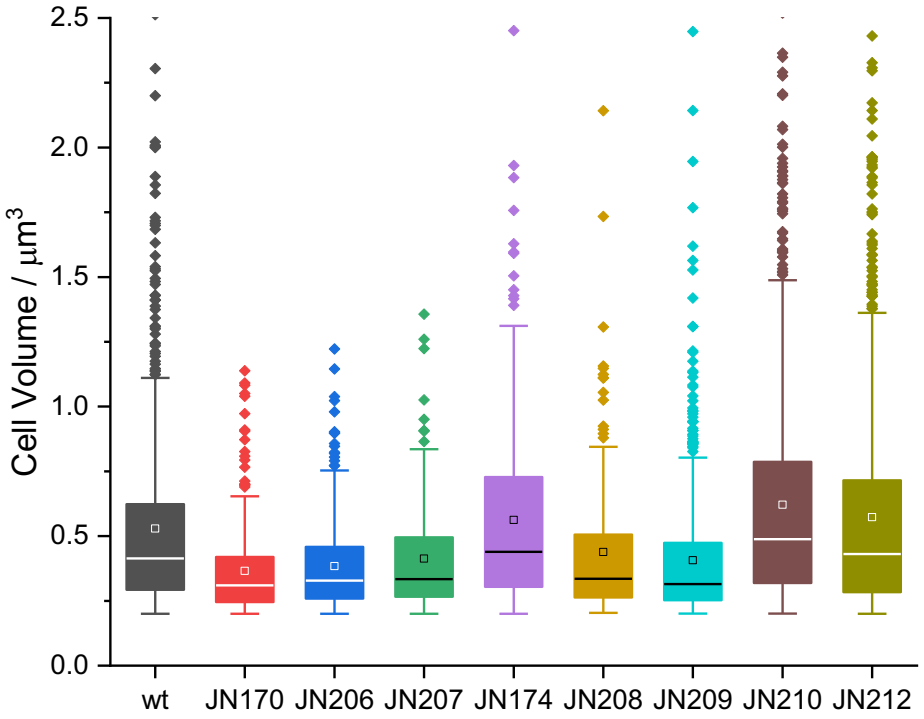

Figure 5.6: Box and whisker plot of size measurements of S. aureus mutant strains. The bottom of the line is the minimum of the range, the upper line is the maximum of the range with outliers appearing as dots above the maximum, the bottom of the box is the first quartile, the top of the box is the upper quartile with the whole box representing the interquartile range of cell lengths, the square inside the interquartile range is the mean and the line in the centre of the interquartile range the median cell length.

Figure 5.6 shows a 5x5 field of view tile scan of the wild type strain (JN112) and the three DTPMP mutant strains (JN170, JN206 and JN207) and Figure 5.7 shows the wild type strain and the five DTPMP mutant strains (JN174, JN208, JN209, JN210 and JN212) as 5x5 field of view tile scans This view allows the intracellular interactions to be investigated more easily as more cells can be viewed at once to see patterns of cell-cell interactions.

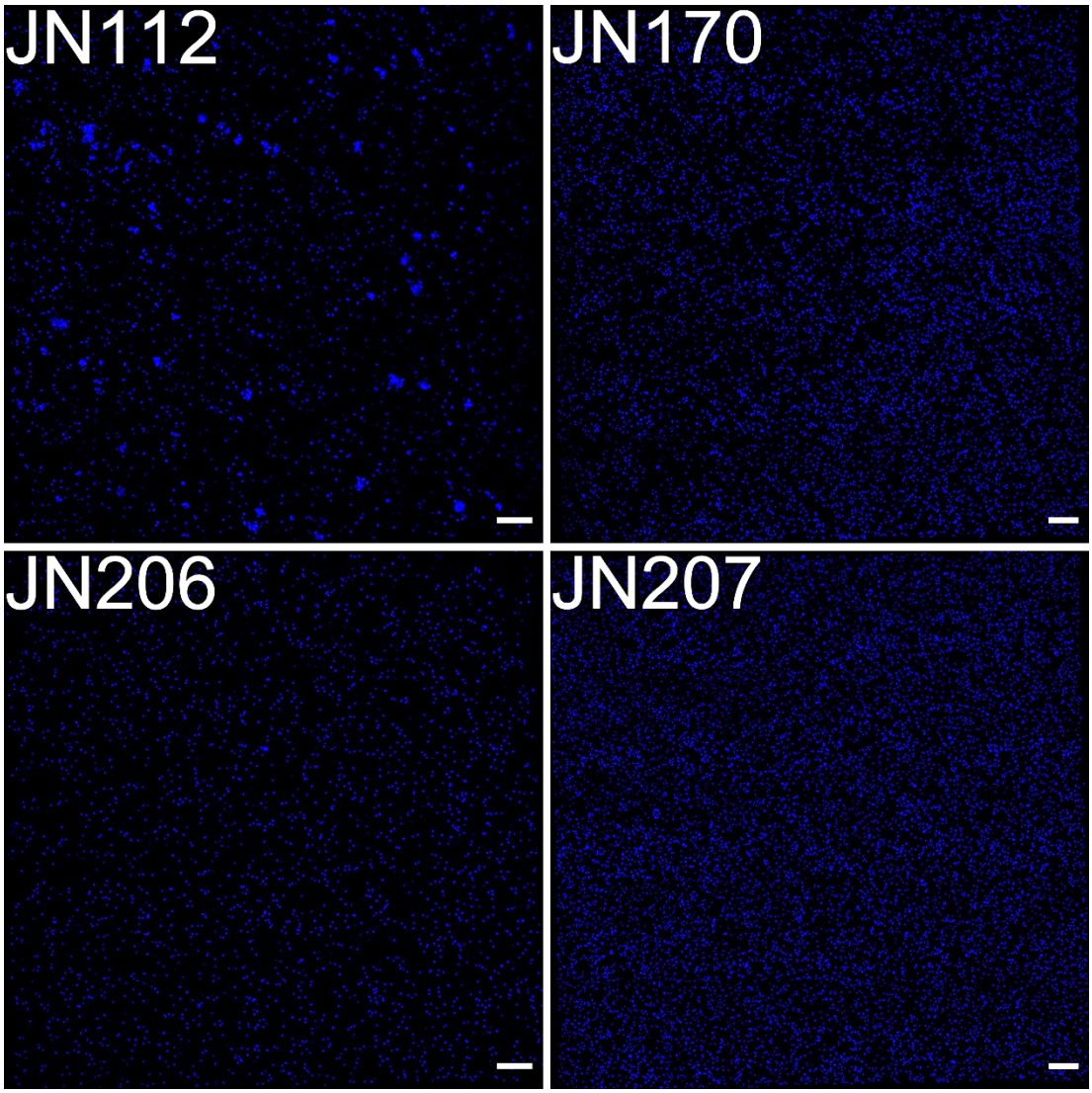

Figure 5.7: Tile scan images of S. aureus wild type and mutant strains obtained from exposure to DTPMP stained with Hoechst 33342. λ_{ex} = 355 nm, λ_{em} = 450-600 nm. Scale bar = 25 µm.

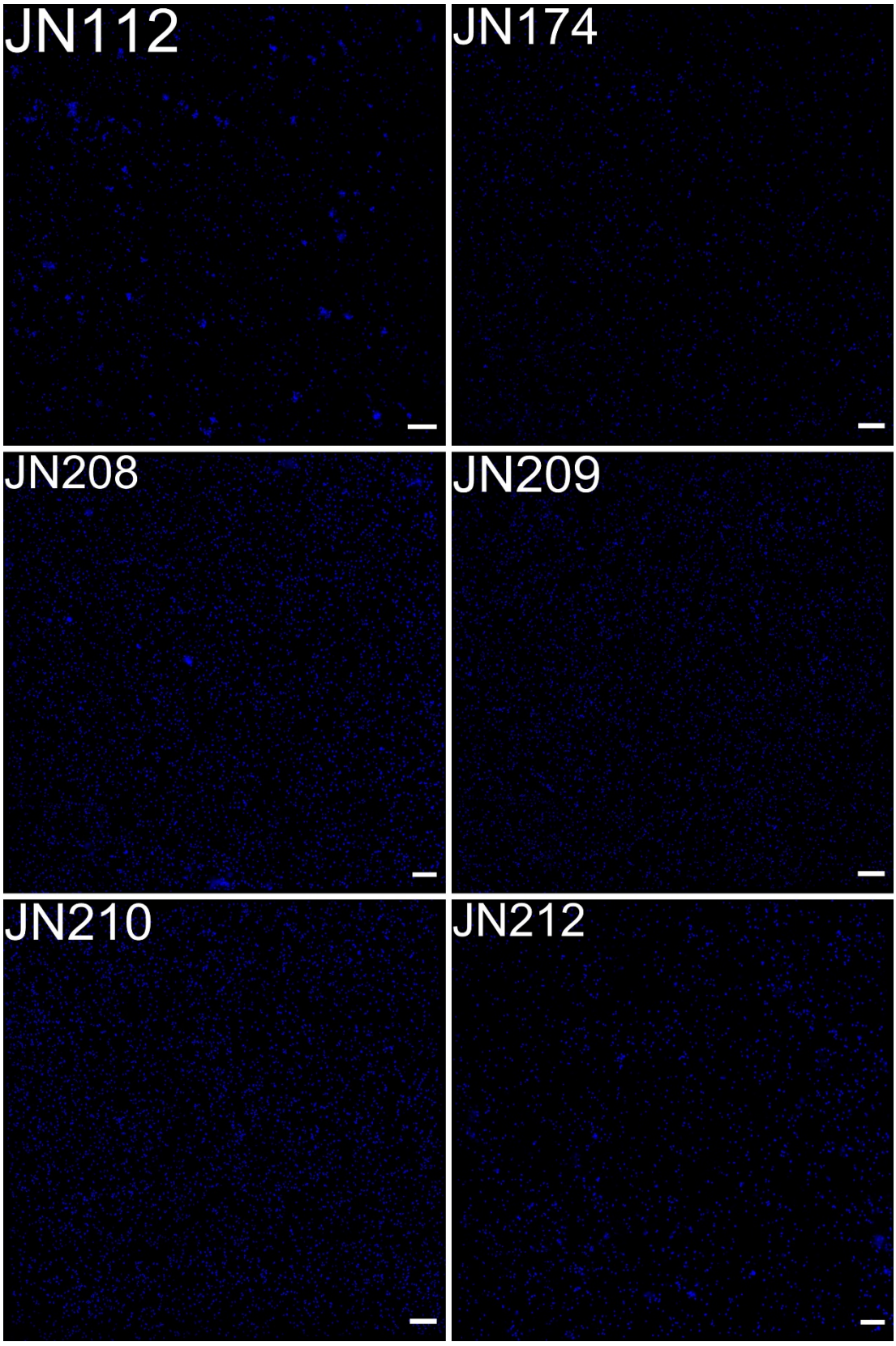

Figure 5.8: Tile scan images of S. aureus wild type and mutant strains obtained from exposure to DTPMP stained with Hoechst 33342. λ_{ex} = 355 nm, λ_{em} = 450-600 nm. Scale bar = 25 µm.

To validate the size measurements recorded the pixel size of the instrument needs to be determined using a standardised micrometer. Figure 5.8 shows an image of a Carl Zeiss Standardised micrometer where the line spacing is 10 µm using the same instrument setup as the images recorded.

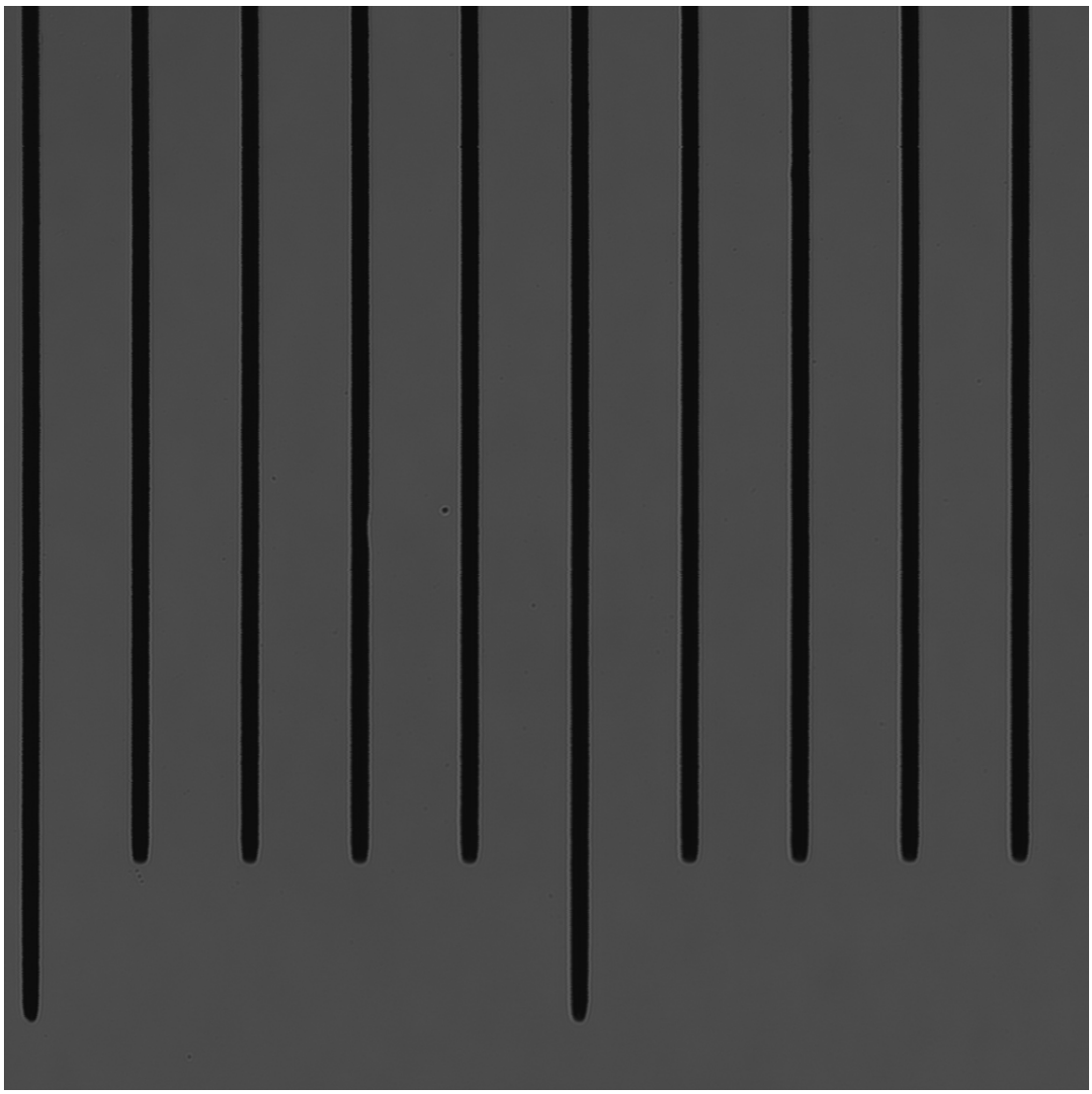

Figure 5.9: Standardised micrometer. The image was recorded on the same system with the same parameters for image recording used. The line spacing is 10 µm.

The 8 bit grey value intensity was plotted across the top of the image and is shown in figure 5.9.

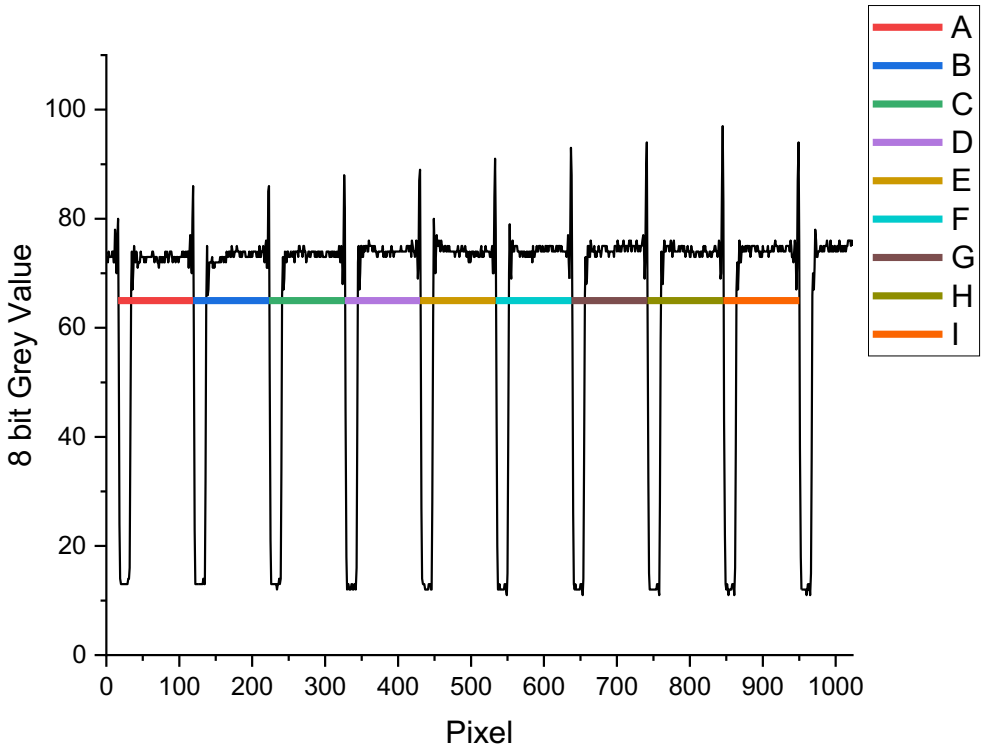

Figure 5.10: Intensity plot of top pixel row of micrometer. The lines indicate measured distances between each line on the micrometer from the left side of each descent at a grey value of 65.

Table 5.3 shows the distance in pixels between the initial descent of each micrometer marking from the left to right to the descent of the next micrometer marking. The length of each pixel is then determined by dividing 10 µm by the number of pixels counted. This shows a regular repeating pattern of 0.0962 µm per pixel or 96.2 nm per pixel. This corresponds exactly with the internally determined pixel size by the microscope confirming that the measurements taken in this chapter are true measurements.

Gap	Initial Pixel	Final Pixel	Number of pixels	10 µm/pixels
A	14	118	104	0.0962
B	118	222	104	0.0962
C	222	326	104	0.0962
D	326	430	104	0.0962
E	430	534	104	0.0962
F	534	638	104	0.0962
G	638	742	104	0.0962
H	742	846	104	0.0962
I	846	950	104	0.0962

Table 5.3: Determination of pixel size of the microscope system. The difference between the initial and final pixel is calculated and then this is divided into 10 µm to determine the length per pixel.

5.4. Discussion

5.4.1. Changes in cell size

Given the small size of the cells it is difficult to distinguish relatively small changes in volume when looking at microscope images so quantitative measurements are required. As shown in table 5.2 and figure 5.5 there were decreases in the cell volumes of some of the mutant strains, some cell volumes remained comparable with the wild type and no mutant strains showed an increase in cell volume. All three strains obtained from exposure to EDTA showed a statistically significant decrease in cell volume at the 99.99% confidence interval. JN208, derived from exposure to DTPMP, has a statistically significant reduced cell volume at the 99.99% confidence interval and JN209, also derived from exposure to DTPMP, had a statistically significant reduced cell volume at the 99% confidence interval. All of the mutants that show a statistically significant decrease in cell volume also show a decrease in overall

cell surface charge, becoming more negatively charged as shown by cytochrome C binding assay.[23]

There is no common mutation between these five mutant strains that are not present in the remaining mutant strains that showed no change in cell volume (Figure 5.1). Conversely there are no mutations present for the mutant strains that did not change cell volume that are not present in the mutant strains the reduced in cell volume. There are, however, some mutations that are common to all the DTPMP-selected mutant strains but not the EDTA derived strains and some mutations that are present in JN208 and JN209 that are different from the other EDTA derived strains.

The change in overall cell volume may be a result of several factors: loosening or tightening of the bacterial cell envelope resulting in an increased or decreased intracellular volume respectively; an increase or decrease in the thickness of the bacterial cell envelope; or changes to the cell division mechanism which could result in smaller or larger daughter cells if cell division occurs earlier or later than it should respectively.

5.4.2. Changes in cell aggregation

Figures 5.6 and 5.7 shows the changes in how the DTPMP and EDTA derived mutated strains aggregate compared to the wild type strain respectively. It is difficult to quantify the overall aggregation of the cells, however, qualitatively it is clear there is a change in the aggregation of the DTPMP and EDTA exposed mutated cells compared to the wild type cells.

The wild type cells aggregate in grape like clusters with some individual cocci and post division diplococci. All the mutant strains no longer exhibit this grape like clustering and only exist as individual cocci or post division diplococci.

The reason for this could be wide ranging from changes in the charge on the surface of the bacteria to changes in the type or amount of surface proteins. Given the mutations present, however, it is most likely that the mutation to Fibronectin-binding protein A (FnBPA) is the cause of the changes in cell aggregation. Fibronectin-binding protein A is a cell surface located protein that plays a role in the accumulation phase of biofilm formation. Multiple low affinity homophilic interactions between FnBPA A domains on neighbouring cells results in microscale cell aggregation. The mutation present in JN170, JN206 and JN207 likely impairs this intracellular interaction which results in cells not being able to effectively aggregate on the microscale.

Given this is a mutation present in all the mutant strains it is highly likely it provides some resistance to chelants.

6. Secondary Lytic Bacteriophage Proteins as Antibacterial Agents

6.1. Bacterial Cell Division

E. coli replicates by binary fission, this means the bacterium elongates and then splits in the centre creating two daughter cells. The *E. coli* cell cycle consists of 3 phases: the B, C and D periods.[99] The B period is the phase in the cell cycle between the conclusion of the previous cell replication and the beginning of DNA replication. The C period is the phase where the genetic material of the cell is replicated. The circular chromosome starts to unwind from being tightly packed so that proteins can access the DNA and begin to replicate it. At the same time, any plasmids that are present are also replicated by the same proteins. Once all the DNA has been replicated the D period begins; in this phase the two chromosomes and any plasmids migrate to opposite ends of the cell and the cell elongates. The cell then divides by a septum forming at the midpoint of the cell and the two parts separate forming the two new cells. At this point the cell cycle begins with the B period in each new cell. The B period is the only phase of the cell replication cycle that changes in speed and is dependent on nutrients and resources available to the cell so determines the replication rate of the bacteria.[100]

The septum that splits the cell in two is formed by the inward synthesis of peptidoglycan at the division site. This is controlled by a cell apparatus called the

divisome. The divisome consists primarily of the proteins FtsA and FtsZ. FtsZ is a tubulin homologue and FtsA is an actin homologue.

FtsZ contains an N-terminal GTPase domain, an interdomain cleft separating the N- and C-terminal domains, and a globular C-terminal domain followed by a disordered 'linker' region, a highly conserved C-terminal tail and a C-terminal variable region.[101] Comparable to tubulin, monomers of FtsZ undergo GTP-dependent head-to-tail polymerisation into filaments, with the C- terminal T7 loop of one subunit inserting itself into the N-terminal GTP-binding domain of another subunit, creating GTPase active site. Figure 6.1 shows the crystal structure of FtsZ and an FtsZ protofilament.

From the filaments of FtsZ formed by GTP binding, the protein GpsB attaches these chains together to form bundles.[102] Figure 6.2 shows the process of FtsZ polymerising into bundles and how the FtsZ bundles form the Z ring around the circumference of the cell.

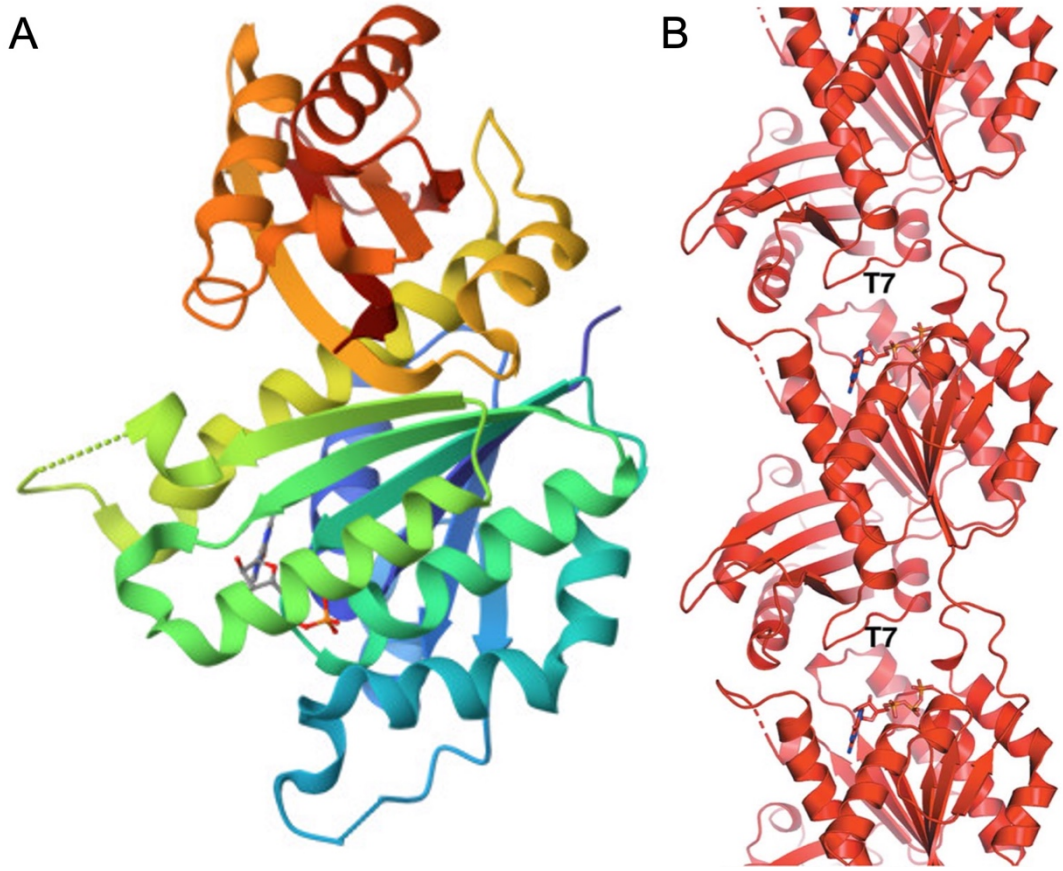

Figure 6.1: Crystal structures of FtsZ. A, monomeric FtsZ in its GDP bound form. B, FtsZ protofilament with labelled T7 loops in each subunit.[103]

These bundles are attached to the inner cell membrane by FtsA. This happens all the way round the circumference of the cell forming a Z ring. The Z ring then recruits peptidoglycan synthesising proteins which begin forming new peptidoglycan. The Z ring treadmills around the cell getting smaller as it moves round which constricts the cell forming the septum made of peptidoglycan so the two new cells can separate. Figure 6.3 shows how the Z ring containing FtsZ and FtsA treadmills around the cell to form a new peptidoglycan layer which constricts inwards.[104]

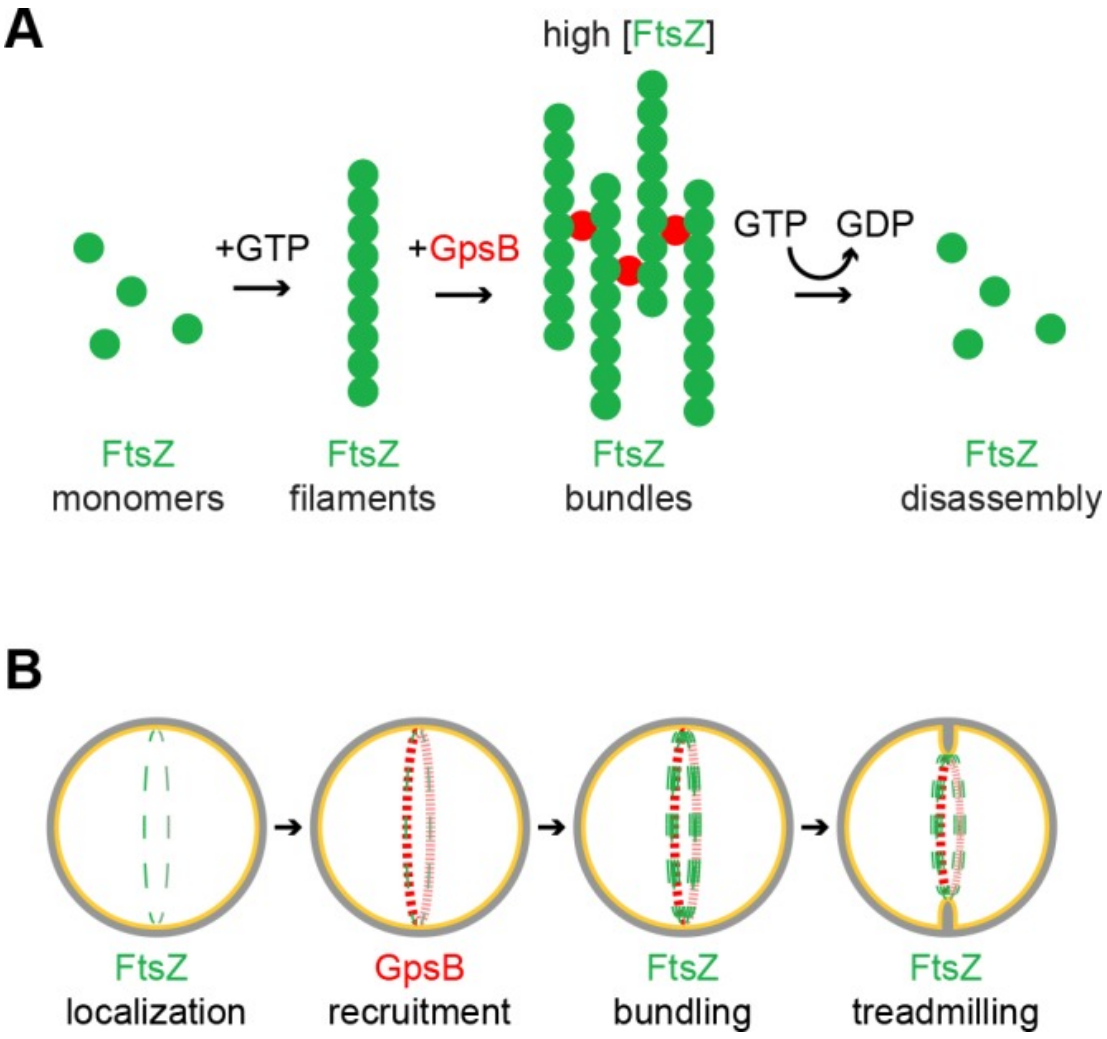

Figure 6.2: Formation of the FtsZ dividing ring by polymerisation of FtsZ monomers into filaments and subsequent bundles. A, Filamentation of FtsZ monomers in FtsZ filaments by GTP binding which are bundled by GpsB, the bundles are disassembled by GTP hydrolysis and the cycle repeats causing a treadmilling action. B, as A but in a cellular model showing the localisation around the circumference of a cell.[102]

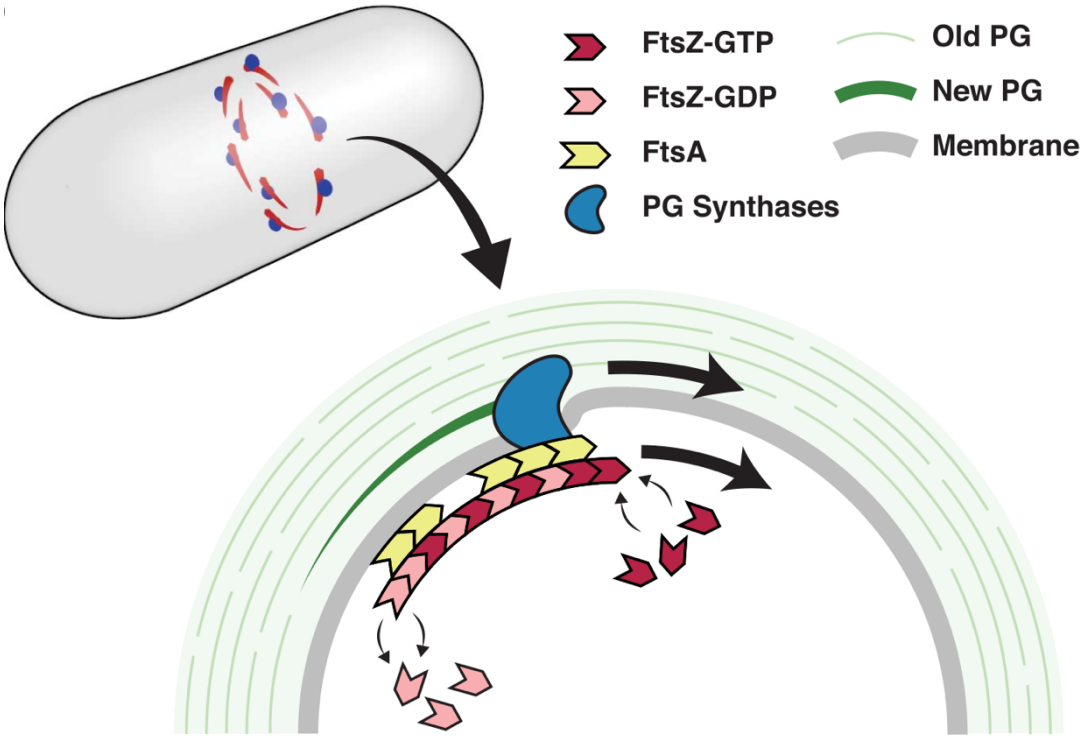

Figure 6.3: Treadmilling action of the FtsZ ring to constrict the cell and form the new septum from peptidoglycan.[104]

When developing novel antibacterial agents, understanding the mechanisms being disrupted offers great advantages; as such most antibacterial agents currently used target synthesis of nucleic acids, proteins or the cell wall as these mechanisms are well understood.[105] Despite extensive characterisation, bacterial cell division has only relatively recently been investigated as a target for antibacterial agents. FtsZ is essential for bacterial growth and viability, it has low homology with eukarytoic proteins (only 20% homology with human tubulin)[106] so targeting in would not affect human cellular processes and, importantly, its structure is highly conserved with 40-50% sequence identity across all bacterial species excluding the *Chlamydiaceae* family and *Ureaplasma urealyticum,* intracellular parasites, which lack FtsZ homologues.[107]

6.2. Kil proteins

FtsZ is already a target of some bacteriophages as part of their lytic cycle; bacteriophage λ has been shown to produce the protein Kil (named for host **k**illing by an **i**nduced **l**ambda prophage) which inhibits FtsZ and causes cell death.[108] The mechanism of cell death is radically different to the lysis usually induced by bacteriophages. In lysis induced by Kil the cell undergoes filamentation, loss of viability and eventual autolysis.[109] Upon expression of *kil* FtsZ rings undergo rapid ablation and through inhibition of *in vivo* FtsZ assembly via a ZipA-dependent mechanism but FtsZ expression levels are unaffected. λ Kil preferentially binds FtsZ-GDP monomers, disrupting FtsZ protofilaments and reducing GTPase activity, most likely in a sequestration mechanism.

Other bacteriophages have genes which encode proteins that have a similar mode of action or eventual outcome (cell lysis) as λ Kil. The phages Mu and Rac possess unrealted *kil* genes which encode proteins with similar killing effects. The prophage Qin has the genes *dicB* and *ydfD* which encode DicB and YdfD respectively which are likely to have a similar action to λ Kil.

Rac Kil is a functional analogue of λ Kil, it inhibits FtsZ action and results in cell lysis.[110] Although Mu Kil has the same name as λ Kil, it does not have a common mode of action and has very little similarity to other Kil protein from any other bacteriophage.[111] Qin DicB does not inhibit FtsZ formation, instead it inhibits the Min

system which prevents septum formation so the cells cannot divide effectively.[112] Finally, Qin YdfD is encoded immediately downstream of DicB but does not use the same mechanism to induce cell lysis; the precise mechanism is not fully understood.[113]

Table 6.1 shows the amino acid sequences for each of the proteins studied.

Protein	Uniprot Accession	Residues	Sequence
E. coli FtsZ	P0A9A6	383	MFEPMELTNDAVIKVIGVGGGGGNAVEHM VRERIEGVEFFAVNTDAQALRKTAVGQTIQI GSGITKGLGAGANPEVGRNAADEDRDALRA ALEGADMVFIAAGMGGGTGTGAAPVVAEV AKDLGILTVAVVTKPFNFEGKKRMAFAEQGI TELSKHVDSLITIPNDKLLKVLGRGISLLDAFG AANDVLKGAVQGIAELITRPGLMNVDFADV RTVMSEMGYAMMGSGVASGEDRAEEAAE MAISSPLLEDIDLSGARGVLVNITAGFDLRLD EFETVGNTIRAFASDNATVVIGTSLDPDMND ELRVTVVATGIGMDKRPEITLVTNKQVQQPV MDRYQQHGMAPLTQEQKPVAKVVNDNAP QTAKEPDYLDIPAFLRKQAD

Phage λ Kil	A0A140NA35	88	MPLQGGLLLAALPNLYLNESPVNYVTDGNALSTYLISQESQRMDQTLMAIQTKFTIATFIGDEKMFREAVDAYKKWILILKLRSSKSIH
Phage Mu Kil	E0J3Q2	75	MMARNIKMATDAQNWLQARGSHVNESYLGVARPILEITYPPVELVKNAVRIMEHKSGVARSVWTARLNGCQIIWR
Phage Rac Kil	B7MPU7	73	MIAHHFGTDEIPRQCVTPGDYVLHEGRTYIASANNIEKRKLYIRNFTTKTCITDCMIKVFIGRDGLPVKAASL
Prophage Qin DicB	A0A828UAX0	62	MKTLLPNVNTSEGCFEIGVTISNPVFTEDAINKRKQERELLNKICIVSMLARLRLMPKGCAQ
Prophage Qin YdfD	P29010	63	MNSAFVLVLTVFLVSGEPVDIAVSVHRTMQECMTAATEQKIPGNCYPVDKVIHQDNIEIPAGL

Table 6.1: Amino acid sequence of FtsZ and lytic phage proteins.

As shown earlier, the crystal structure of FtsZ has been solved but none of the lytic phage proteins have had their structures solved. The structures of the proteins have been predicted by AI using AlphaFold and are shown in figure 6.4.

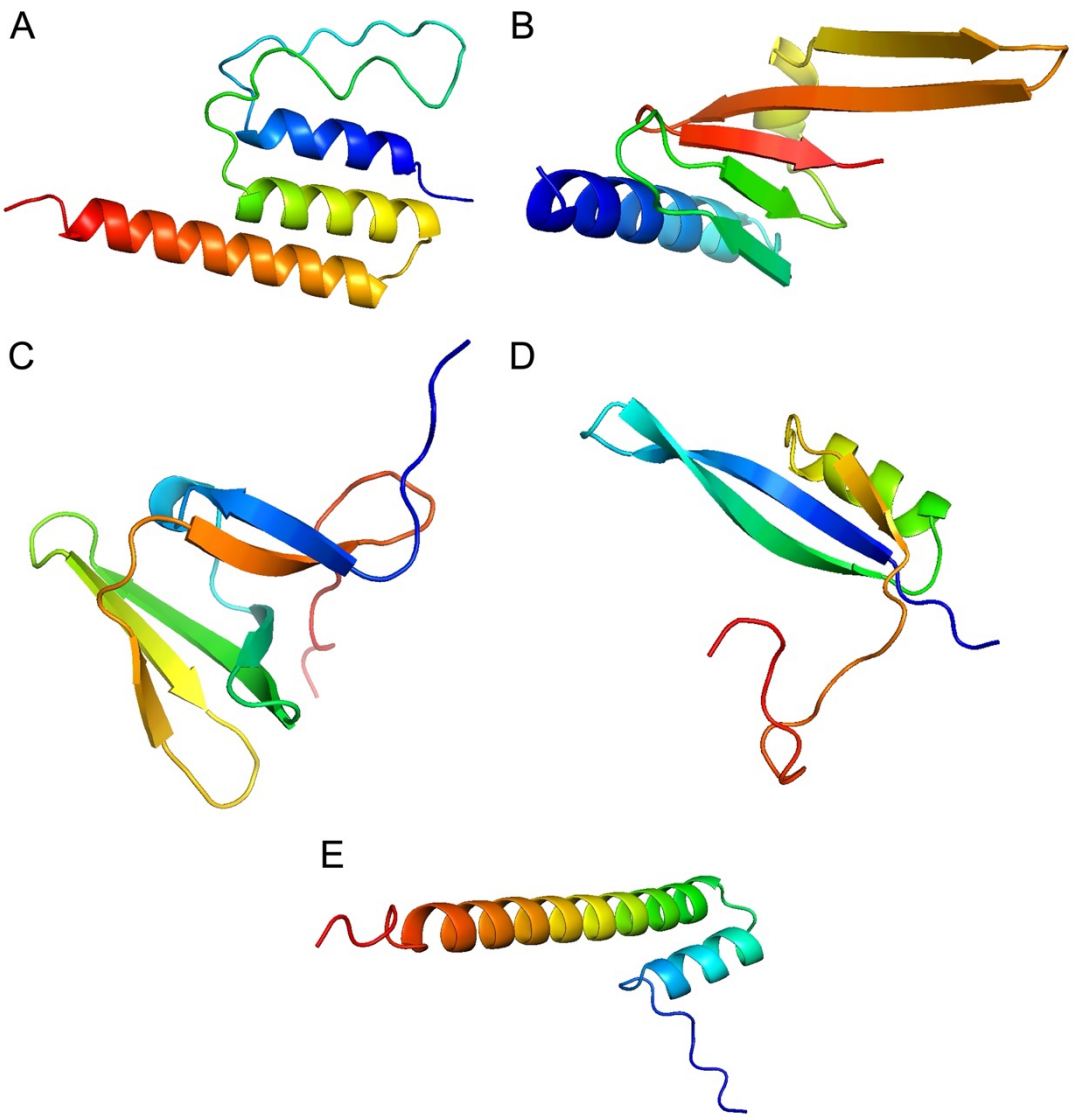

Figure 6.4: Predicted Structures of Bacteriophage Secondary Lytic Proteins. Structure of Phage λ Kil (A), Phage Mu Kil (B), Phage Rac Kil (C), Prophage Qin YdfD (D) and Prophage Qin DicB (E) as predicted by AlphaFold.[114,115] *Coloured as rainbow from N to C termini.*

6.3. Results and Discussion

6.3.1. Viability assays

BL21-AI *E. coli* were transformed with the plasmids listed in table 6.2 which had either ampicillin (Ap) or kanamycin (Km) resistance.

Shorthand Name	Vector	Inserted Gene	Antibiotic Resistance
16b	pET16b	N/A	Ap
22b	pET22b(+)	N/A	Ap
FtsZ	pET16b	*E. coli ftsZ*	Ap
λ	pET22b(+)	Phage λ *kil*	Ap
28a	pET28a(+)	N/A	Km
Mu	pET28a(+)	Phage Mu *kil*	Km
Rac	pET28a(+)	Phage Rac *kil*	Km
DicB	pET28a(+)	Prophage Qin *dicB*	Km
YdfD	pET28a(+)	Prophage Qin *ydfD*	Km

Table 6.2: Plasmids used to transform E. coli BL21-AI into phage protein expressing strains and control strains with no genes inserted and endogenous ftsZ inserted.

Viability assays were performed by serially diluting the transformed strains onto agar plates containing a corresponding antibiotic (uninduced) or a corresponding antibiotic, arabinose and IPTG (induced) as shown in figure 6.5.

The pET vectors do not have a toxic effect either in the induced or uninduced plates and overexpression of FtsZ also confers no toxic effects upon the cells. However, all

of the phage proteins do exhibit toxicity when they are overexpressed with Mu Kil and Qin DicB being the most toxic upon overexpression.

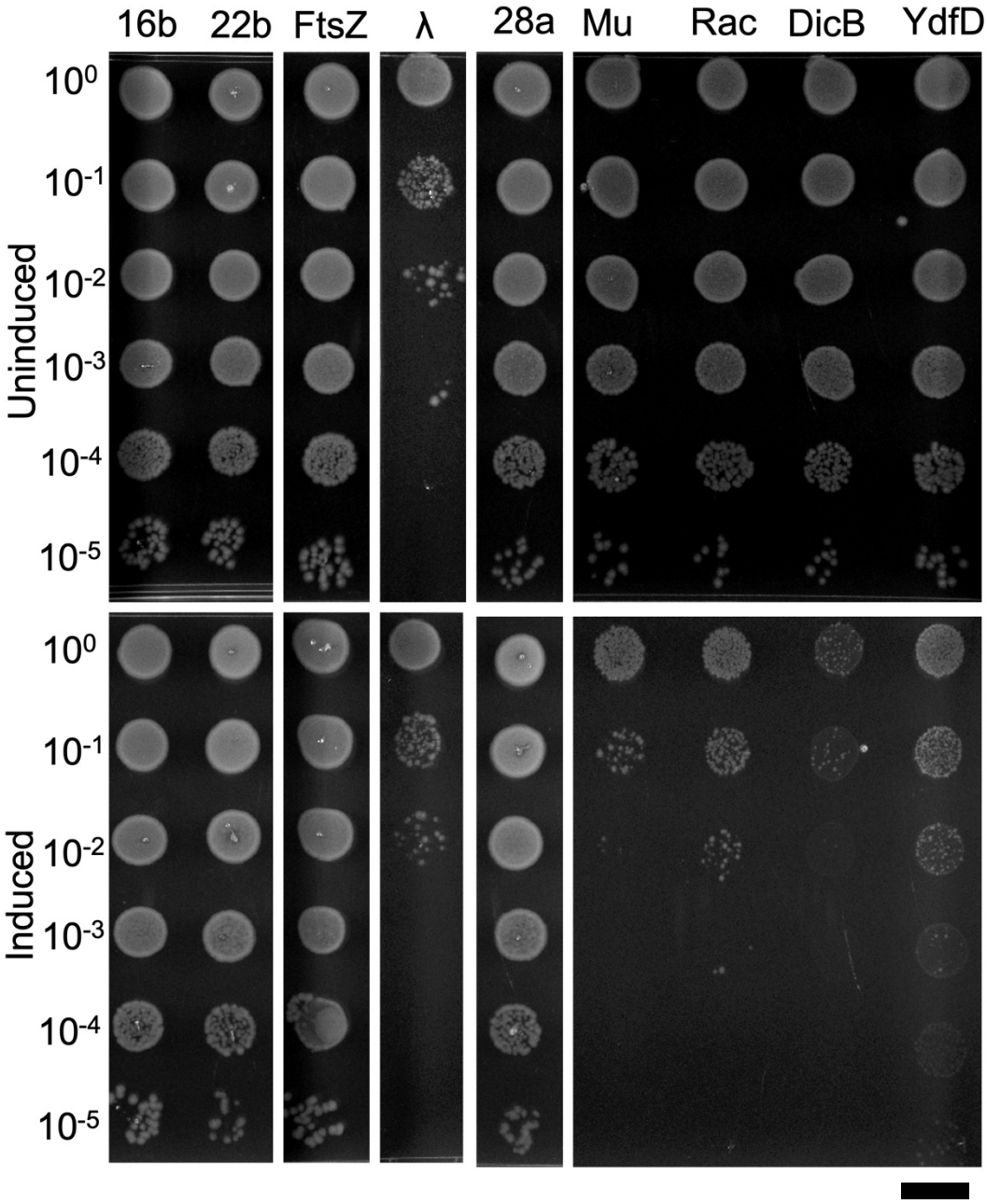

Figure 6.5: Viability assays of transformed E. coli BL21-AI. Top, uninduced agar plates with only the corresponding antibiotic added. Bottom, induced plate with the corresponding antibiotic, arabinose and IPTG added. Scale bar = 1 cm.

6.3.2. Effect of Bacteriophage Protein Overexpression on Bacterial Cell Morphology

Since the phage proteins affect the formation of a septum during cell division it was expected that cellular division itself would be affected. When bacterial cell division is affected the shape and size of the bacterial cell is typically also affected. The bacteria were imaged using a Live/Dead stain previously used to assess membrane damage when bacteria are exposed to chelants comprising SYTO9 and propidium iodide (PI).

This stain provides several benefits: firstly, it allows the visualisation of the bacteria to assess changes to size and shape upon induction of protein expression; secondly, since both stains (SYTO9 and PI) are nucleic acid stains it allows for assessment of changes in distribution of DNA throughout the cell that may be associated with phage protein activity; and finally since the stain that is visible changes when the membrane becomes compromised it allows for a correlation to be drawn between the extent of cell morphological changes and the point at which cells are no longer viable.

6.3.3. Effect of FtsZ Overexpression on Bacterial Cell Morphology

First it was essential to ensure the pET plasmids did not themselves induce any morphological changes in the cell and obtain a baseline. Figure 6.7 shows BL21-AI *E. coli* transformed with pET16b, pET22b(+) and pET28a(+) stained with Live/Dead stain. The images consist of a stitched tile scan of 5x5 images to image as many individual bacteria as possible. The experiments were repeated in triplicate with 3 separate

biological repeats and 3 sets of images taken for each biological repeat. The images shown are representative of the whole series.

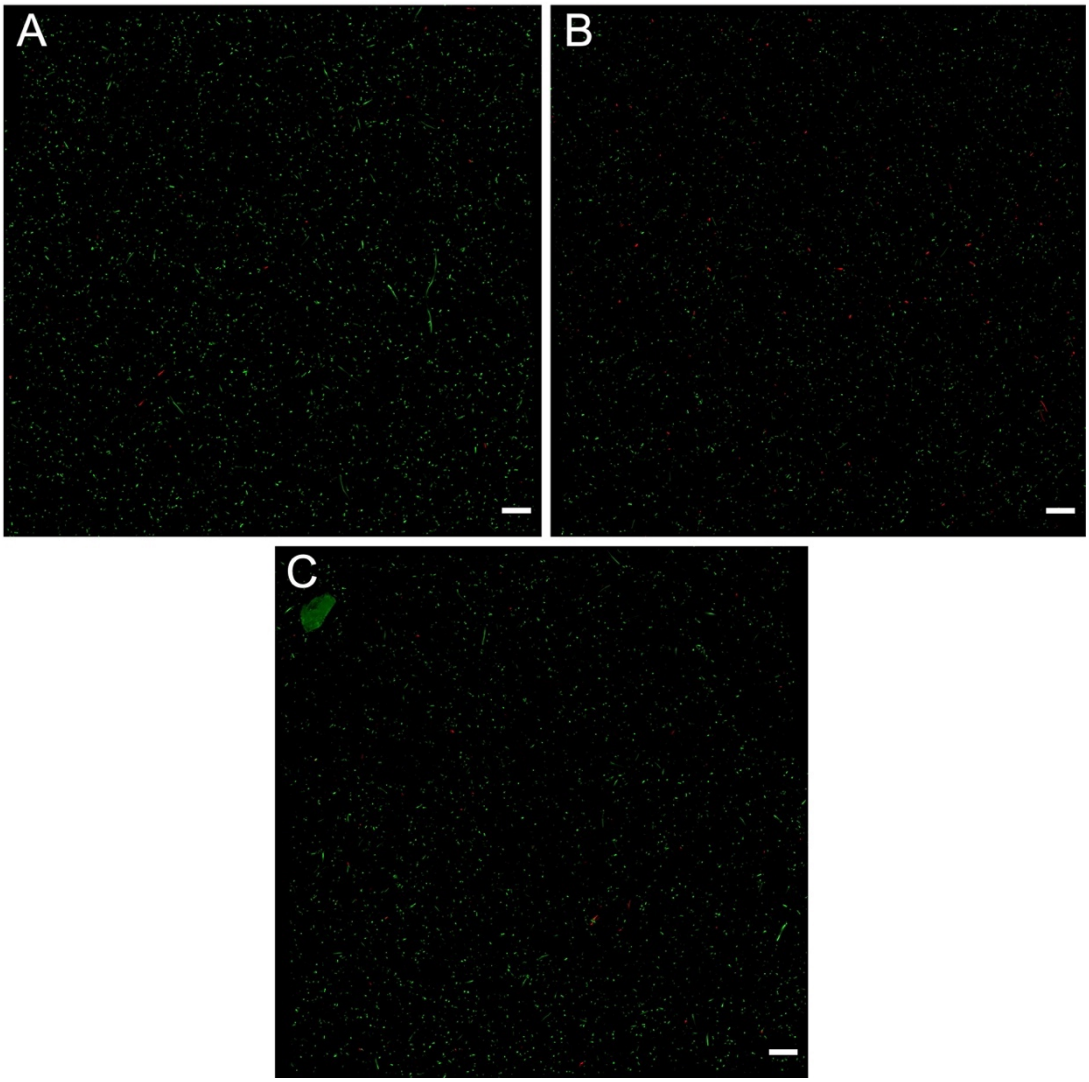

Figure 6.7: Live/Dead staining of E. coli BL21-AI transformed with pET plasmids. LSCM images of BL21-AI E. coli transformed with pET16b (A), pET22b(+) (B) and pET28a(+) (C) and stained with SYTO9 (green) and PI (red). SYTO9, λ_{ex} = 488 nm, λ_{em} = 500-520 nm. PI, λ_{ex} = 533 nm, λ_{em} = 550-650 nm. Scale bar = 25 µm.

Although some anomalous bacteria are present the majority of cells conform to the expected size and shape. BL21-AI has been observed to filament to a small degree, so these anomalous cells are not indicative of any toxicity.[116]

Before assessing the effect of the phage proteins the effect of overexpression of FtsZ was investigated. Figure 6.8 shows BL21-AI *E. coli* transformed with pET16b-FtsZ stained with Live/Dead stain with and without arabinose and IPTG added to induce expression of FtsZ.

Without induction of FtsZ transcription the bacteria show no morphological changes when compared to the control bacteria. Upon overexpression of the FtsZ there is some lengthening of the cells when compared to the control. There are also more dead bacteria as indicated by the ratio of red to green cells increasing.

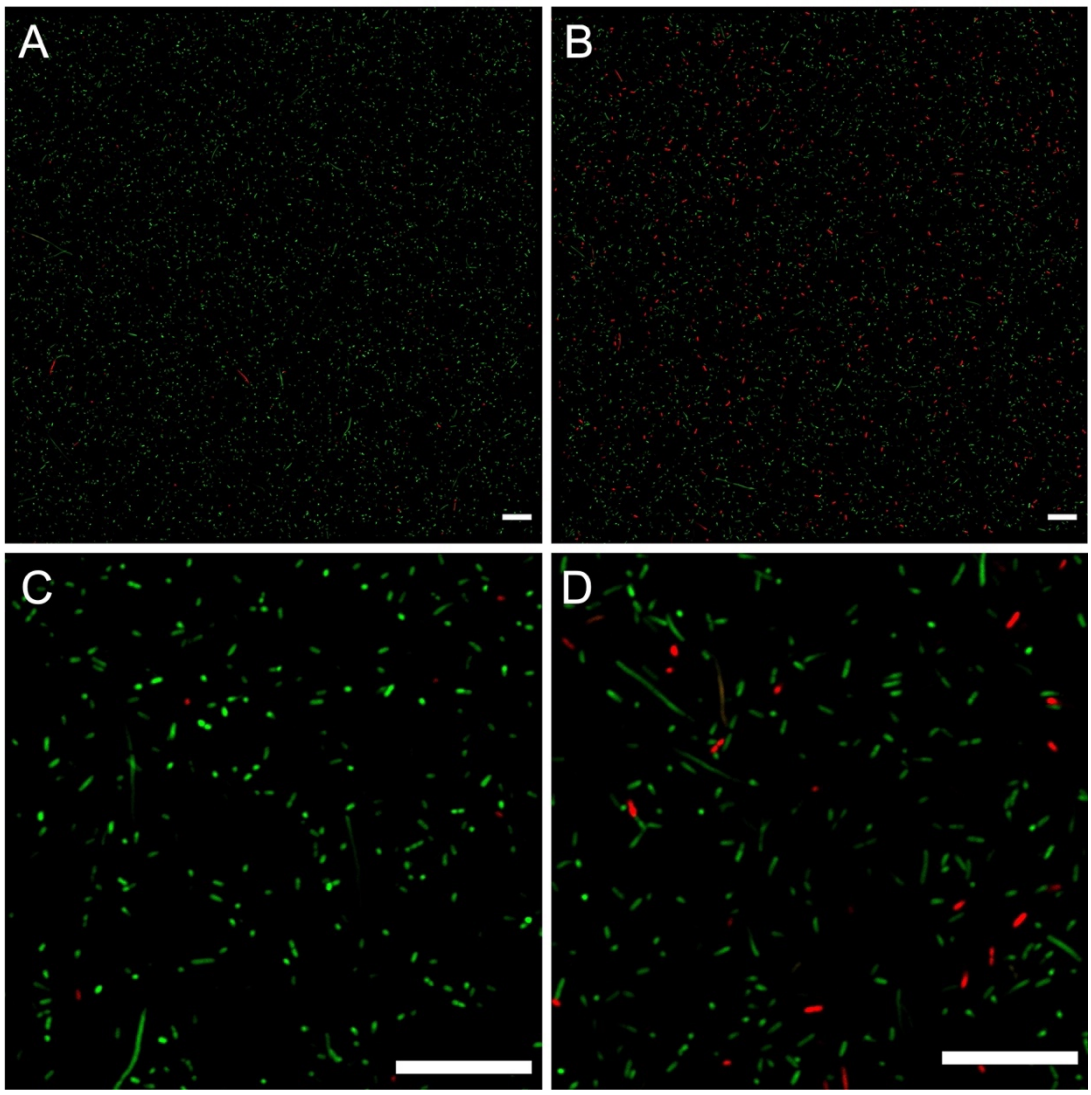

Figure 6.8: Live/Dead staining of E. coli BL21-AI transformed with pET16b-FtsZ. LSCM images of BL21-AI E. coli transformed with pET16b-FtsZ uninduced (tilescan) (A), induced (tilescan) (B), uninduced (single frame) (C) and induced (single frame) (D) and stained with SYTO9 (green) and PI (red). SYTO9, λ_{ex} = 488 nm, λ_{em} = 500-520 nm. PI, λ_{ex} = 533 nm, λ_{em} = 550-650 nm. Scale bar = 25 µm.

6.3.4. Effect of Bacteriophage Mu Kil Overexpression on Bacterial Cell Morphology

Figure 6.9 shows BL21-AI *E. coli* transformed with pET16b-Mu Kil stained with Live/Dead stain with and without arabinose and IPTG added to induce expression of Mu Kil.

Without induction of Mu Kil expression there is a slight effect on the morphology of the bacteria with cells being shorter than the control bacteria. This contrasts with the other Kil proteins that have been studied where cell lengthening is often observed. Given that Mu Kil has a very different structure to the Kil proteins from the other species, this is not surprising and the bactericidal effect of Mu Kil could still be due to FtsZ inhibition but through an alternative pathway to other Kil proteins.

Upon inducing overexpression of Mu Kil the effect on the morphology of the cells is enhanced even further. The individual bacteria lose their characteristic rod shape and instead appear more as a typical cocci bacterium.

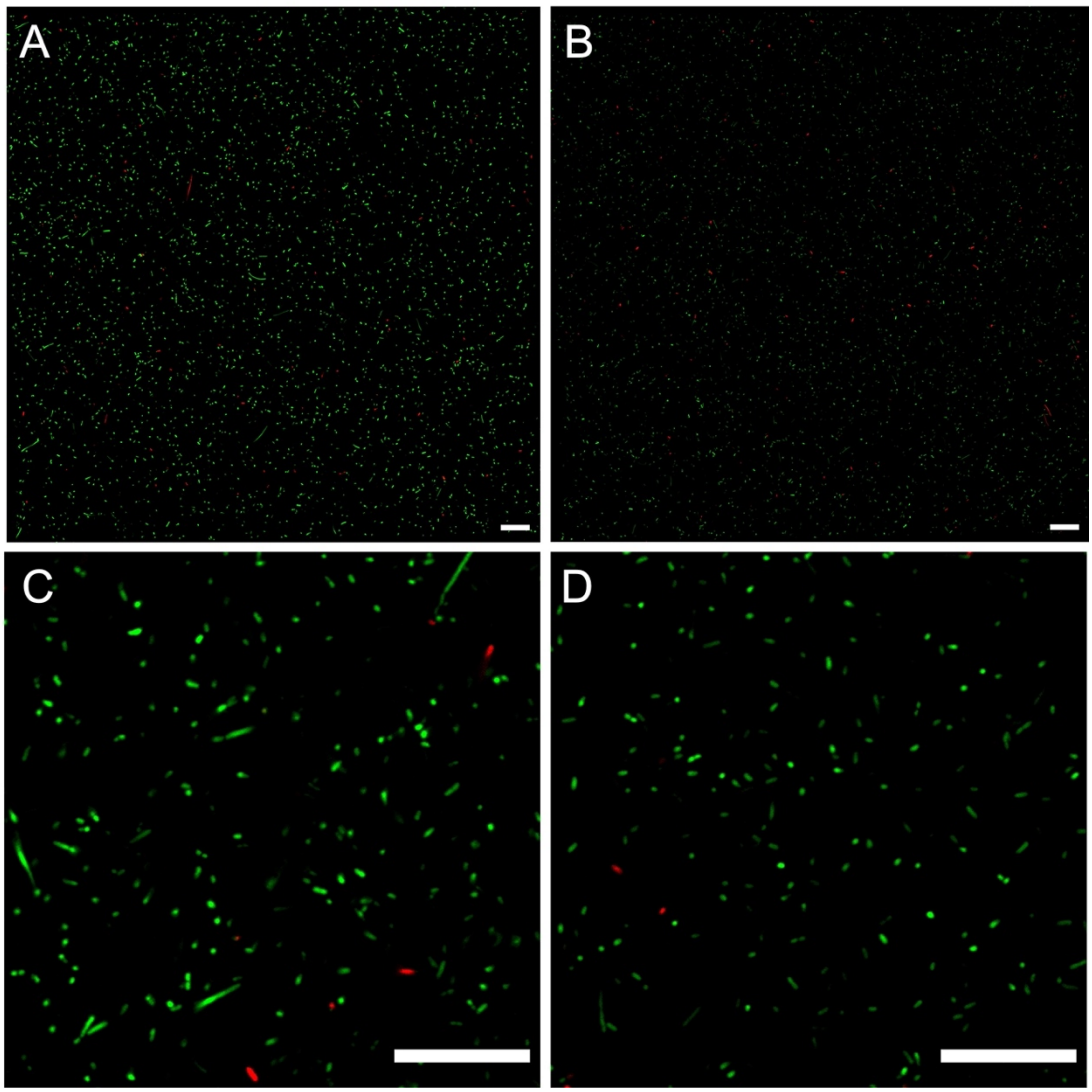

Figure 6.9: Live/Dead staining of E. coli BL21-AI transformed with pET16b-Mu Kil. LSCM images of BL21-AI E. coli transformed with pET16b-Mu Kil uninduced (tilescan) (A), induced (tilescan) (B), uninduced (single frame) (C) and induced (single frame) (D) and stained with SYTO9 (green) and PI (red). SYTO9, λ_{ex} = 488 nm, λ_{em} = 500-520 nm. PI, λ_{ex} = 533 nm, λ_{em} = 550-650 nm. Scale bar = 25 µm.

6.3.5. Effect of Bacteriophage Rac Kil Overexpression on Bacterial Cell Morphology

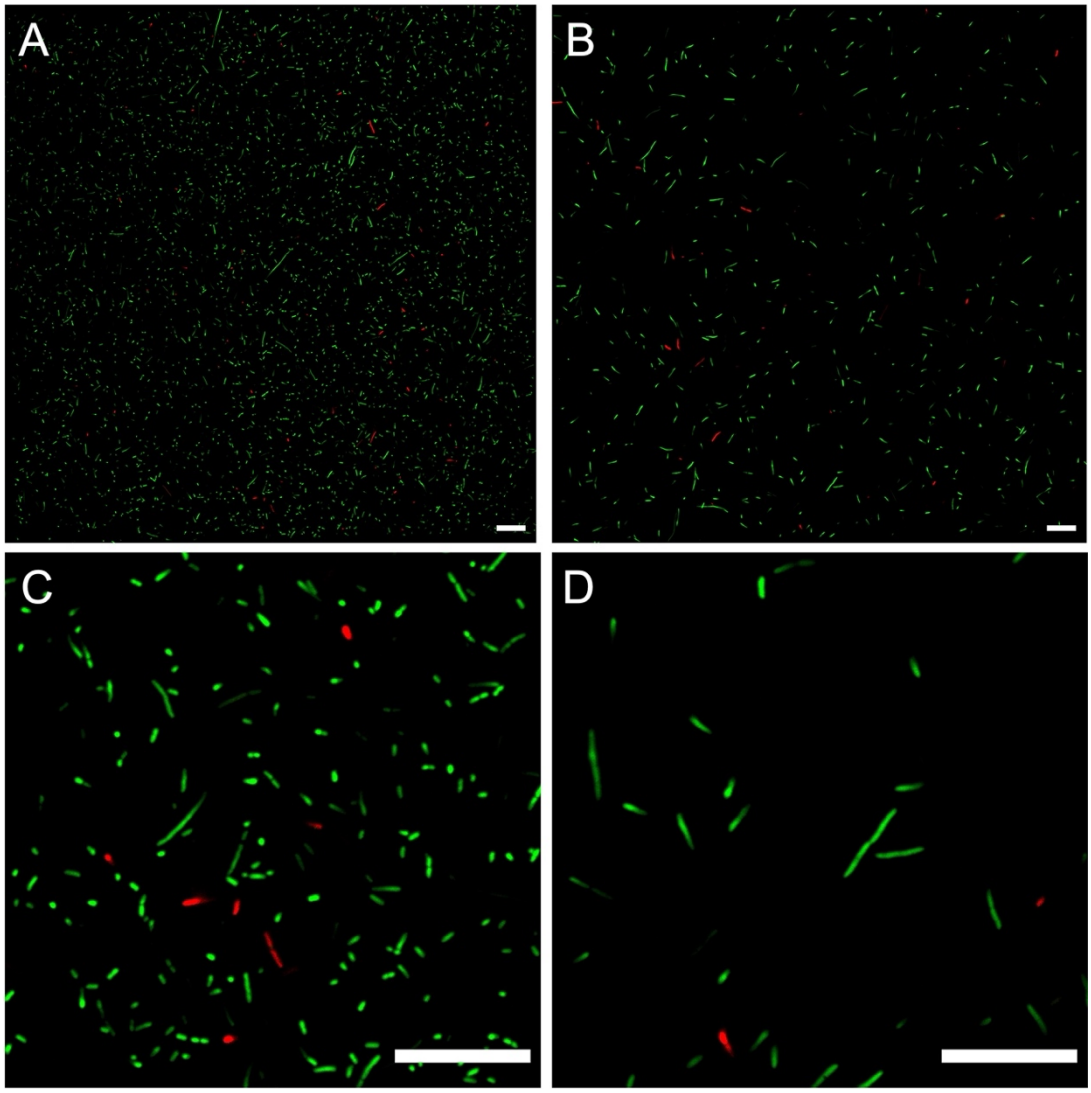

Figure 6.10: Live/Dead staining of E. coli BL21-AI transformed with pET16b-Rac Kil. LSCM images of BL21-AI E. coli transformed with pET16b-Rac Kil uninduced (tilescan) (A), induced (tilescan) (B), uninduced (single frame) (C) and induced (single frame) (D) and stained with SYTO9 (green) and PI (red). SYTO9, λ_{ex} = 488 nm, λ_{em} = 500-520 nm. PI, λ_{ex} = 533 nm, λ_{em} = 550-650 nm. Scale bar = 25 µm.

Figure 6.10 shows BL21-AI *E. coli* transformed with pET16b-Rac Kil stained with Live/Dead stain with and without arabinose and IPTG added to induce expression of Rac Kil.

Rac Kil causes *E. coli* to filament resulting in elongated bacteria that will eventually lose viability and die. Without induction of overexpression there are still some bacteria that have filamented and elongated, more so than in the control bacteria. Upon induction of overexpression, the amount of bacteria that are longer than the control bacteria has greatly increased with few bacteria that are normal length.

This effect can be explained by Rac Kil's inhibition of FtsZ. Since the divisome cannot form properly the bacteria cannot divide properly and continues growing along its axis resulting in filamented bacteria.

The fluorescence of SYTO9 is not equal along the length of the bacteria indicating there is an unequal distribution of DNA throughout the cell. This will be explored later in this chapter.

6.3.6. Effect of Prophage Qin DicB Overexpression on Bacterial Cell Morphology

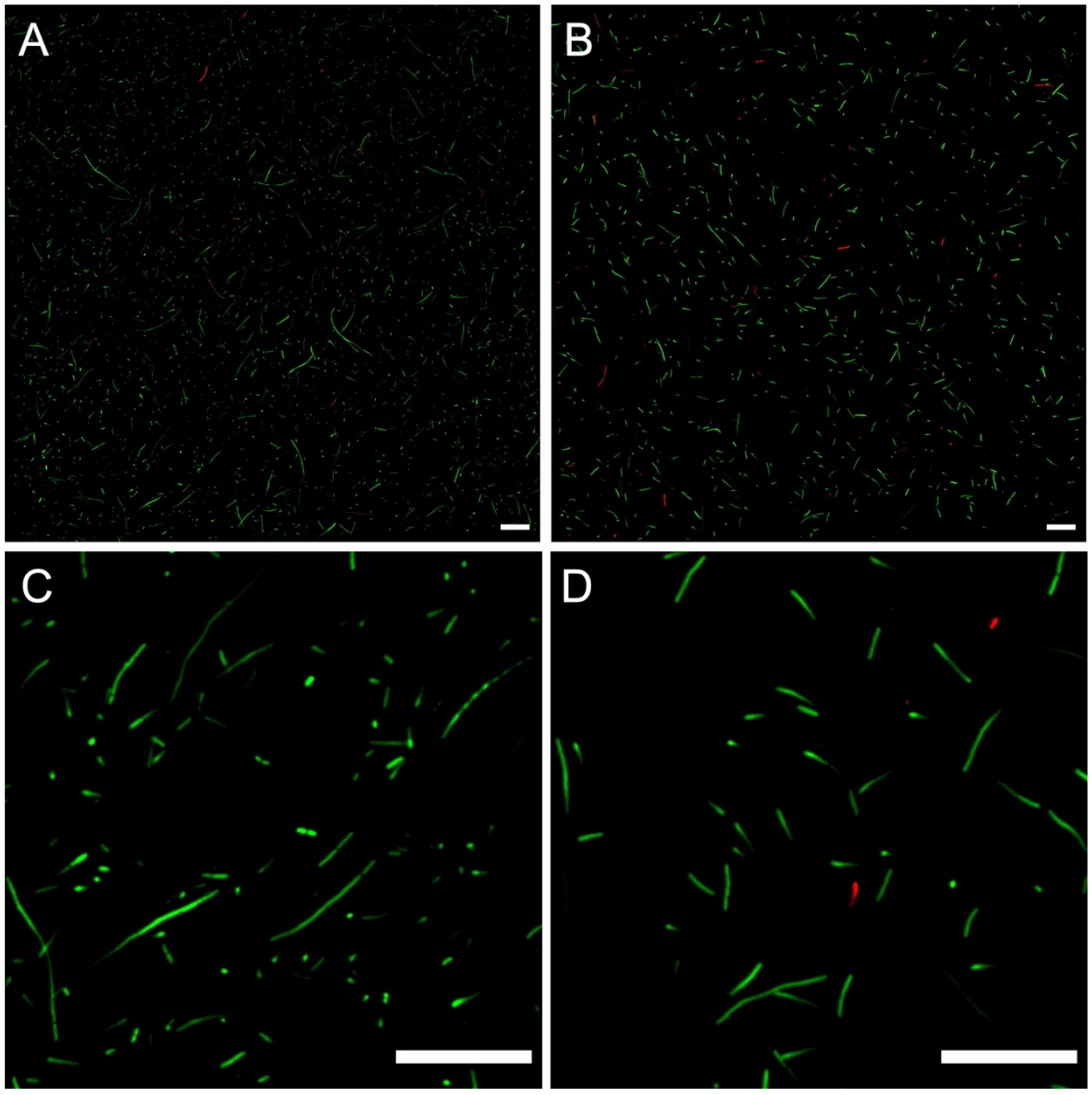

Figure 6.11: Live/Dead staining of E. coli BL21-AI transformed with pET16b-Qin DicB. LSCM images of BL21-AI E. coli transformed with pET16b-Qin DicB uninduced (tilescan) (A), induced (tilescan) (B), uninduced (single frame) (C) and induced (single frame) (D) and stained with SYTO9 (green) and PI (red). SYTO9, λ_{ex} = 488 nm, λ_{em} = 500-520 nm. PI, λ_{ex} = 533 nm, λ_{em} = 550-650 nm. Scale bar = 25 µm.

Figure 6.11 shows BL21-AI *E. coli* transformed with pET16b-Qin DicB stained with Live/Dead stain with and without arabinose and IPTG added to induce expression of Qin DicB.

Qin DicB affects the morphology greater than any other protein investigated. Without overexpression, the morphology of the cells is already affected greatly; some of the cells have filamented significantly with lengths of over 50 μm measured in some individual bacteria.

Upon overexpression this effect is exacerbated, and all of the bacteria are filamented with no cells of normal length. The largest cell measured during overexpression of DicB was over 60 μm. Of interest is the fact that there is no correlation between the length of the cell and cell death. Using this method to measure cell viability, the increased length does not result in reduced viability. It may be the case that the cells would eventually lose viability at this length but since the cells were imaged on a relatively short time frame after induction the cells retained viability and it is likely had they have been imaged later they would have not survived.

6.3.6. Effect of Prophage Qin YdfD Overexpression on Bacterial Cell Morphology

Figure 6.12 shows BL21-AI *E. coli* transformed with pET16b-Qin YdfD stained with Live/Dead stain with and without arabinose and IPTG added to induce expression of Qin YdfD.

Without overexpression of prophage Qin YdfD there is no change in morphology of the bacteria or in the apparent viability with the ratio of cells stained with SYTO9 or PI remaining constant when compared to the control bacteria.

However, upon induction of overexpression of prophage Qin YdfD there is a significant change to the bacteria. The morphology of the cells remains constant with most cells displaying normal dimensions with some cells showing some filamentation. The main change is the viability of the cells, more cells are now fluorescing with PI than SYTO9, indicating greater amounts of cell death. This suggests that prophage Qin YdfD does not act on the FtsZ ring in the same way as the other phage proteins do and its mechanisms of cell lysis is something else.

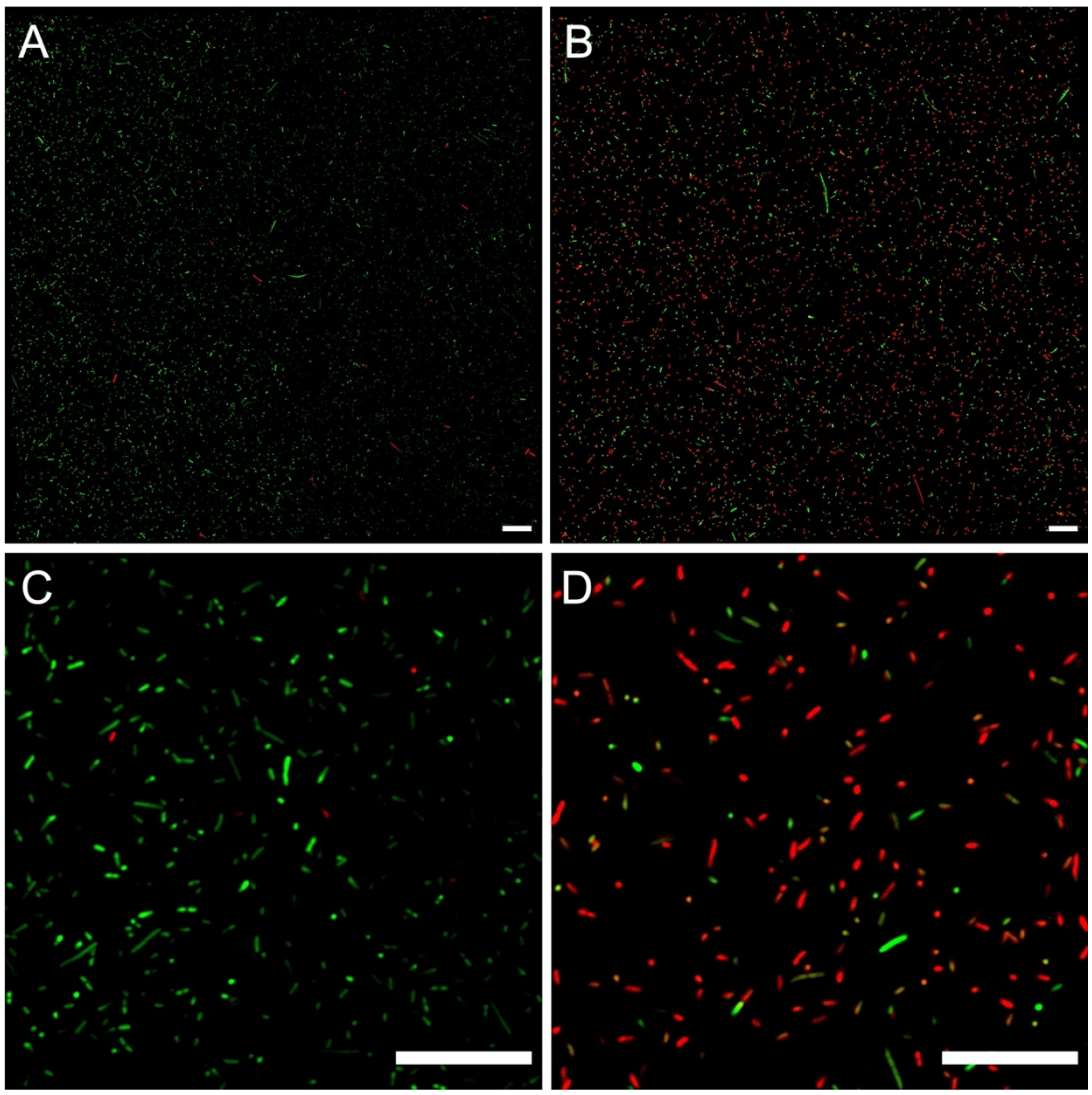

Figure 6.12: Live/Dead staining of E. coli BL21-AI transformed with pET16b-Qin YdfD. LSCM images of BL21-AI E. coli transformed with pET16b-Qin YdfD uninduced (tilescan) (A), induced (tilescan) (B), uninduced (single frame) (C) and induced (single frame) (D) and stained with SYTO9 (green) and PI (red). SYTO9, λ_{ex} = 488 nm, λ_{em} = 500-520 nm. PI, λ_{ex} = 533 nm, λ_{em} = 550-650 nm. Scale bar = 25 µm.

6.3.7. Effect of Bacteriophage Proteins on DNA Distribution Throughout the Cell

DNA should be evenly distributed throughout a healthy bacterium. Given the morphological changes observed with some of the bacteriophage lytic proteins, the distribution of DNA throughout an individual bacterium was assessed using LSCM.

The cells were stained with DAPI and imaged with induction of expression by arabinose and IPTG. The excitation wavelength for DAPI was 355 nm and emission was collected from 450-550 nm. Only Rac Kil, Qin DicB and Qin YdfD were imaged to assess the DNA distribution because the rounding effect of Mu Kil would not have generated useful DNA profiles due to cell compactionm

To analyse the distribution of DNA throughout the cell single representative cells that showed pathology (filamentation) and recoloured to allow easier viewing. The 8-bit gray value was then plotted along the long axis of the cell.

Figure 6.13 shows normal, healthy cells and the different states that they can show depending on their state in the division cycle.

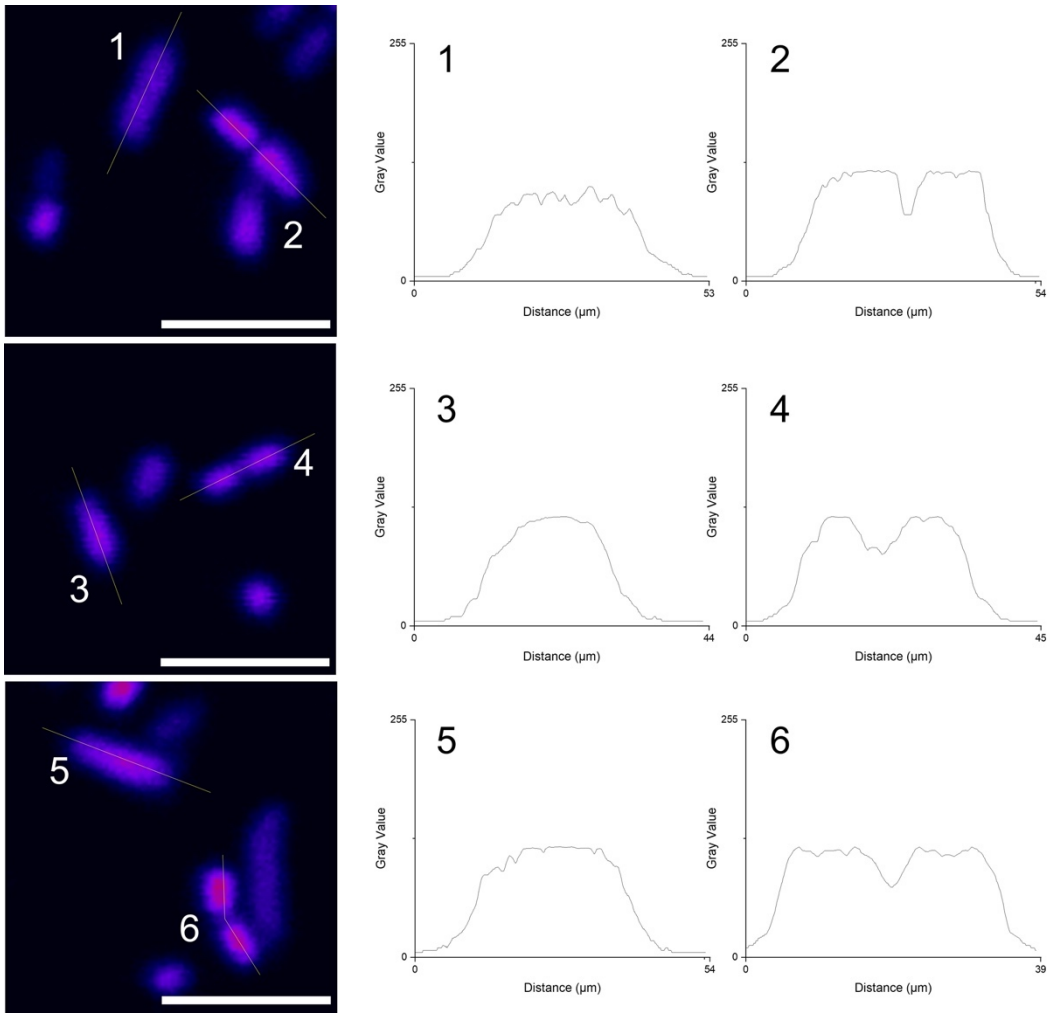

Figure 6.13: DNA distribution throughout static and dividing E. coli BL21-AI cells. Gray values are measured along the long axis of the cells as indicated by the yellow line. Cells are stained with DAPI, λ_{ex} = 355 nm, λ_{em} = 450-550 nm. Scale bar = 5 µm.

The cells labelled as 1, 3 and 5 are not currently dividing and show similar profiles of DAPI fluorescence intensity and, hence, the amount of DNA along the axis of the cell. The amount of DNA rises quickly at the poles of the cell and reaches a plateau in the central two thirds of the cell axis. This plateau has little variation indicating even distribution of DNA through the cell.

The cells labelled as 2, 4 and 6 are immediately post division so show a different profile of DNA distribution. Here the cells show the same profile on the edges of the cell axis with a steep rise to a plateau, but there is a cleft with a drop in DNA density where the dividing ring has formed and where the septum forms.

With these two normal profiles in mind Figures 6.14, 6.15 and 6.16 show pathogenic bacteria expressing the three phage proteins of interest and their DNA profiles along their axis.

Figure 6.14 shows the effect of phage Rap Kil on DNA distribution throughout the cell. Whilst Rap causes filamentation and eventual lysis of the bacteria it only has a mild effect on the distribution of DNA throughout the cell. The top image shows a cell that has filamented but has successfully divided, albeit much longer than what it should be. Here we see a profile similar to cells 2, 4 and 6 in figure 6.13 only extended due to the filamentation. The rise in gray value intensity is not as steep as in the healthy cells but this is probably due to the cell being longer, so the DNA is stretched further throughout the cell and not as compact. The middle image shows four cells attached at their poles. The individual cells are of a normal, healthy length but have not separated post-division, which is what they would usually do, giving the impression of a single, filamented cell. The DNA profile indicates that a proper septum has not formed at the half and quartile points of the cell as the reduction in gray values is not as intense in healthy cells. The bottom image is of two cells that have divided but remain attached at their poles. The cells are longer than they should be which indicates they have either divided late or have divided and have continued to grow

whilst still attached because they cannot separate fully. The distribution of DNA is much more variable than that of the healthy cells but as with the top image this could be due to the length of the cell and not a direct result of Rac Kil action.

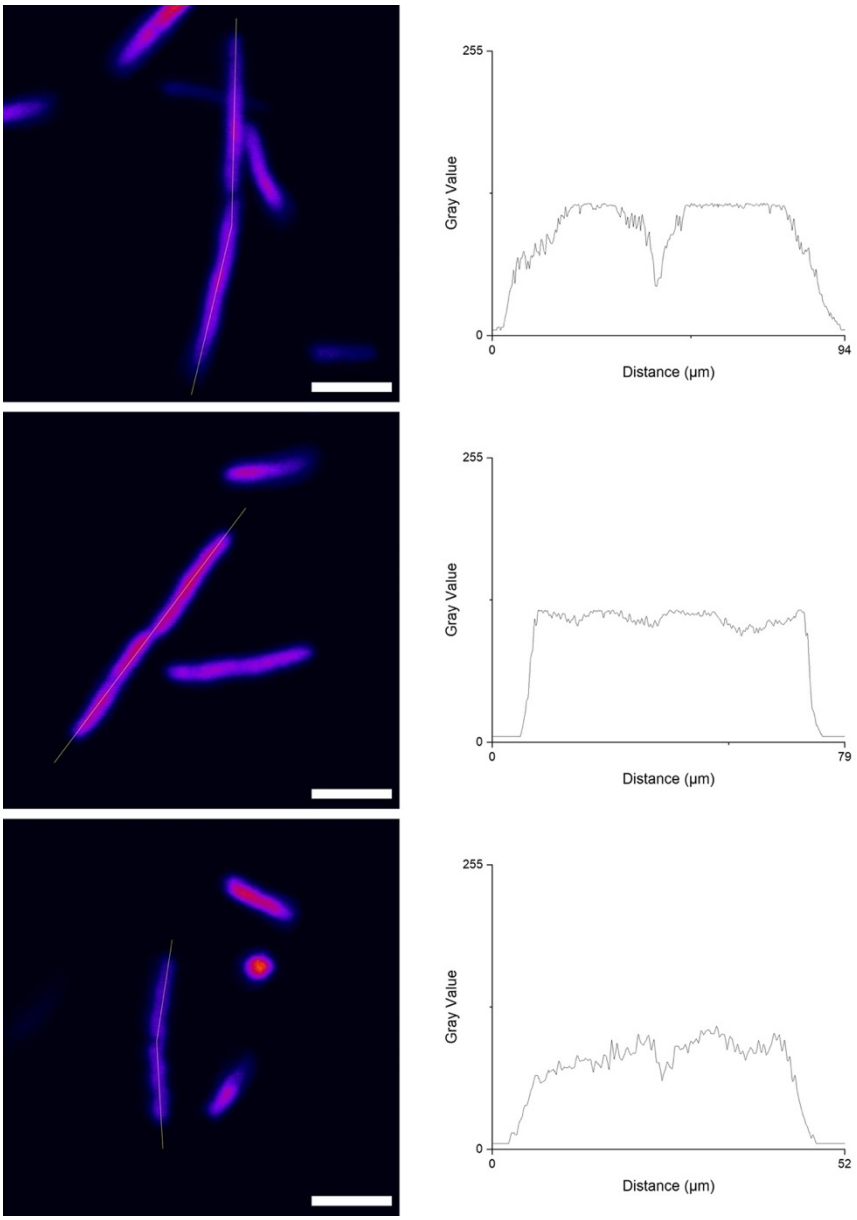

Figure 6.14: DNA distribution throughout pathogenic E. coli BL21-AI cells overexpressing phage Rac Kil. Gray values are measured along the long axis of the cells as indicated by the yellow line. Cells are stained with DAPI, λ_{ex} = 355 nm, λ_{em} = 450-550 nm. Scale bar = 5 µm.

Overall, Rac Kil does cause changes in the distribution of DNA throughout an individual bacterial cell, but the changes are consistent with a side effect of the filamentation and cell lengthening affecting the overall density of DNA. These results also show that not only do Rac Kil expressing cells filament, but they also cannot separate after division as effectively as healthy cells. This is likely due to poor septum formation resulting in two quasi separated cells that have some connection between them.

Overexpression of prophage Qin DicB causes similar filamentation to overexpression of phage Rac Kil and it causes similar effects on the distribution of DNA throughout the cell. Figure 6.15 shows the effect of Qin DicB overexpression on DNA distribution throughout individual bacteria.

The top image shows three cells attached at their axes, two of which are normal length and one which has filamented. These cells have not separated fully, likely due to improper septum formation. Apart from the improper separation the cells do show a normal distribution consisted with the healthy cells shown in figure 6.13 with a steep rise at the poles and a consistent plateau. The middle image shows a single cell which is approximately double the size of a healthy cell. The cell does, however, have a normal distribution of DNA with a steep rise in intensity at the poles and an even intensity throughout the bacterium, albeit longer than a typical bacterium.

The bottom image, however, shows a very abnormal bacterium with an atypical distribution of DNA throughout the bacterium. This bacterium has a relatively even

distribution of DNA that fades towards one end of the cell. This could be caused by the bacterium being out of the focal plane, however, the transmission image of this bacterium does not indicate this so suggests there is some malformity in the control of DNA distribution throughout the cell.

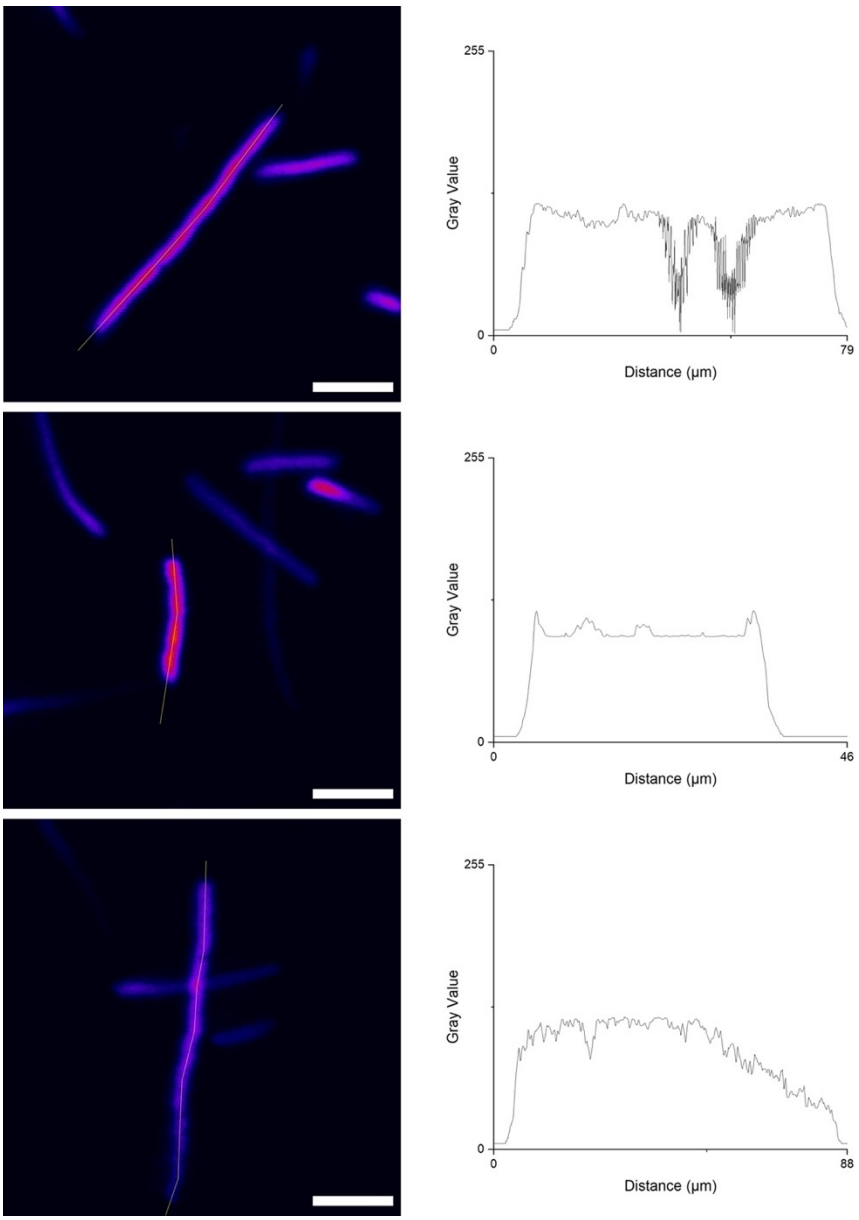

Figure 6.15: DNA distribution throughout pathogenic E. coli BL21-AI cells overexpressing prophage Qin DicB. Gray values are measured along the long axis of the cells as indicated by the yellow line. Cells are stained with DAPI, λ_{ex} = 355 nm, λ_{em} = 450-550 nm. Scale bar = 5 μm.

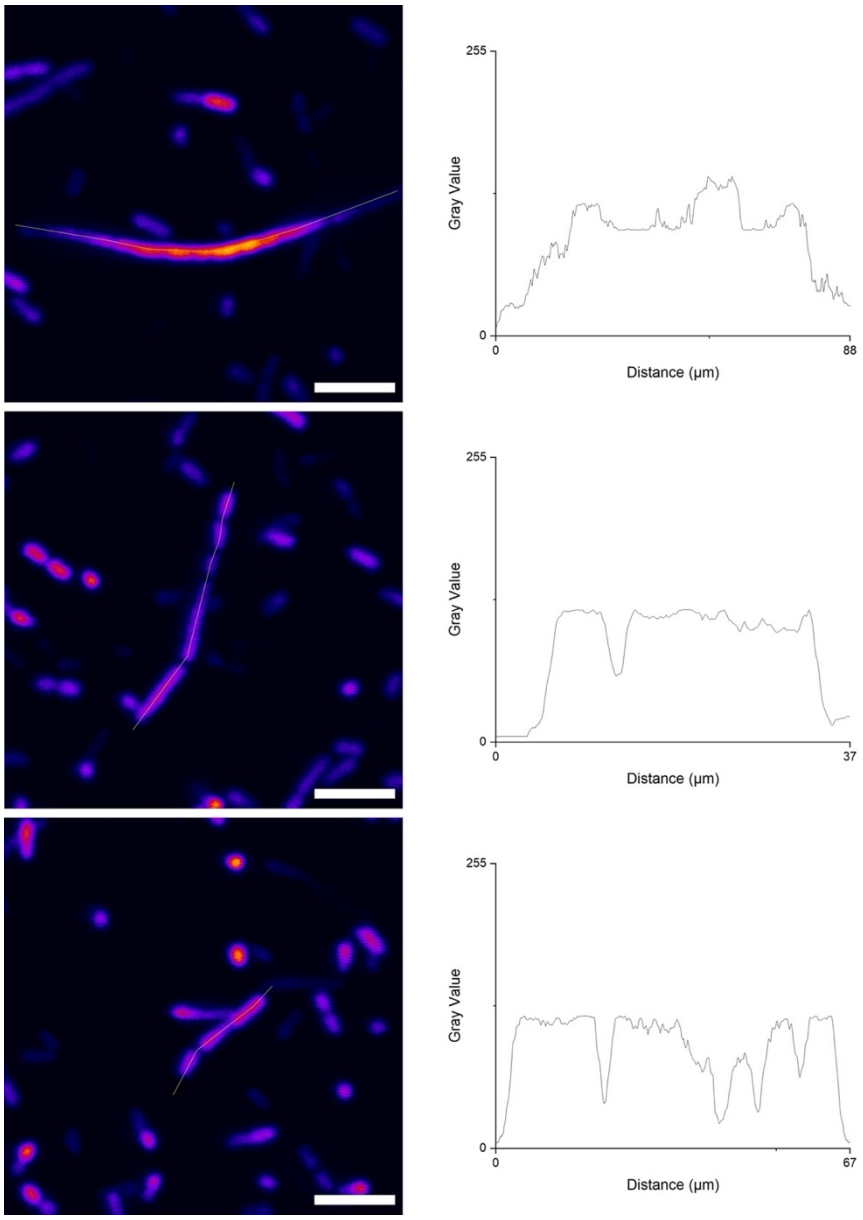

Figure 6.16: DNA distribution throughout pathogenic E. coli BL21-AI cells overexpressing prophage Qin YdfD. Gray values are measured along the long axis of the cells as indicated by the yellow line. Cells are stained with DAPI, λ_{ex} = 355 nm, λ_{em} = 450-550 nm. Scale bar = 5 µm.

Overexpression of prophage Qin YdfD results in very abnormal distribution of DNA throughout individual bacteria. All three of the bacteria shown in Figure 6.16 show abnormal distributions that do not conform to any of the distributions shown in Figure 6.13. The uppermost cell in Figure 6.16 shows a cell which has no uniformity

in the distribution in DNA throughout the cell. The cell does not have a typical sharp rise, plateau, and sharp fall; instead, the cell shows a gradual rise in intensity, a very variable intensity and gradual decline. This indicates the cell no longer has control over the distribution of DNA throughout the cell; the Min system of DNA control must have been disrupted.

The middle image in Figure 6.16 again shows abnormality in the distribution of DNA throughout the bacteria. In this case there are two possible explanations: from the intensity plot it appears the cell has no control over its distribution of DNA; however, upon observing the bacteria it appears that the "cell" has tried to divide but has not been successful in doing so and has several failed divisomes formed with several "individual cells" attached together. This pattern is, again, observed in the bottom image of Figure 6.16 where three uneven spaced bacteria are joined but have individual chromosomal intensities.

There are two possible explanations for the highly irregular distributions of DNA throughout bacteria overexpressing prophage Qin YdfD: improper division leading to partial divisomes separating separate chromosomes contained in cells of irregular length; or, an inhibition of the Min system which controls the distribution of DNA throughout the cell during division. Given there are two separate patterns displayed in the top, and the middle and bottom images, it is probably that prophage Qin YdfD causes both effects to be observed.

7. Ultra-high resolution 3D printing - micropatterning coverslips

7.1. Introduction

Given the effect Kil related bacteriophage proteins have on cell division, particularly the FtsZ ring generated during septum formation[117], it would be beneficial to examine the machinery of cell division in more detail. By attaching fluorescent proteins that can engage in Förster resonance energy transfer (FRET) to both FtsZ and the Kil related proteins any interaction between the two can be directly observed.[118] An example fluorescent protein pair would be cyan fluorescent protein (CFP) and yellow fluorescent protein (YFP), both of which are colour variants of green fluorescent protein (GFP).[118] When CFP is excited (λ_{max} = 435 nm) and in close proximity to YFP energy is transferred and the YFP fluoresces. The Förster radius, the distance between the two fluorophores where FRET is 50% effective, for a CFP-YFP pair is 5 nm.[119] This means that the two proteins with the CFP and YFP tags need to be very close for the FRET to occur and hence an interaction between the proteins can be inferred. Figure 7.1 shows a simplified spectrum of two ideal fluorophores which could undergo FRET. The energy that would be emitted from the donor is instead transferred to the acceptor which subsequently emits energy as a photon. Significant overlap between emission of the donor and absorbance of the acceptor is one of the criteria necessary for successful FRET.[120] Figure 7.2 shows a Jablonski diagram showing the change in energy levels of the donor and acceptor molecules during FRET.

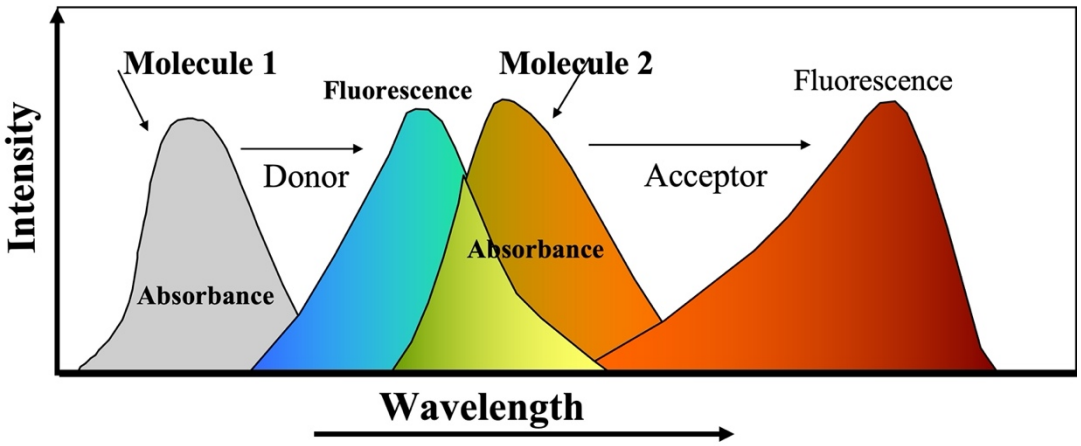

Figure 7.1: The spectral principle of FRET. The emission profile of the donor must overlap with the absorbance profile of the acceptor for energy to be transferred non radiatively.

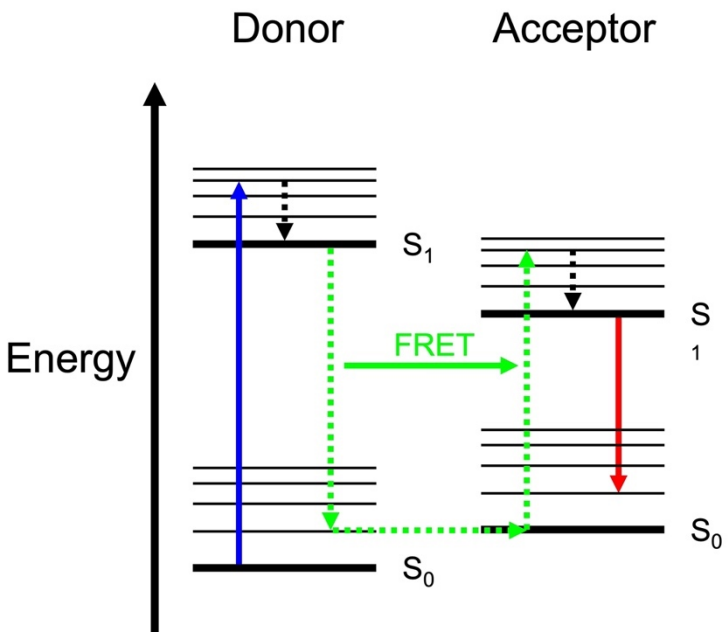

Figure 7.2: Jablonski diagram of FRET. After absorption and internal relaxation, energy is transferred from the donor to the acceptor which can emit a photon of light after internal relaxation.

Equation 7.1 shows the factors affecting the rate at which FRET can occur with ν_{DA} being the coulombic electronic coupling matrix, κ being the orientation factor, s the screening factor and J_{DA} being the overlap integral as already discussed above.

$$k_{FRET} = \frac{2\pi}{\hbar} \times |\nu_{DA}|^2 \times |\kappa^2| \times s^2 \times J_{DA} \qquad \textit{Equation 7.1}$$

Importantly in this case is the coulombic electronic coupling matrix which is defined in equation 7.2. This equation shows that the rate of FRET is proportional to the inverse sixth power of the distance between the donor and acceptor (R_{DA}) allowing the two fluorophores to be used as a molecular ruler.

$$\nu_{DA} = \frac{\mu_D \times \mu_D}{{R_{DA}}^3 \times (4\pi\varepsilon_0)} \qquad \textit{Equation 7.2}$$

To better visualise the cell division machinery that could be affected by the presence of bacteriophage proteins it would be beneficial to view the bacteria in a defined orientation. Figure 7.3 illustrates how the different orientations of a rod-shaped bacterium would result in two very different images being generated, each conveying different information about the condition of the cell division apparatus.

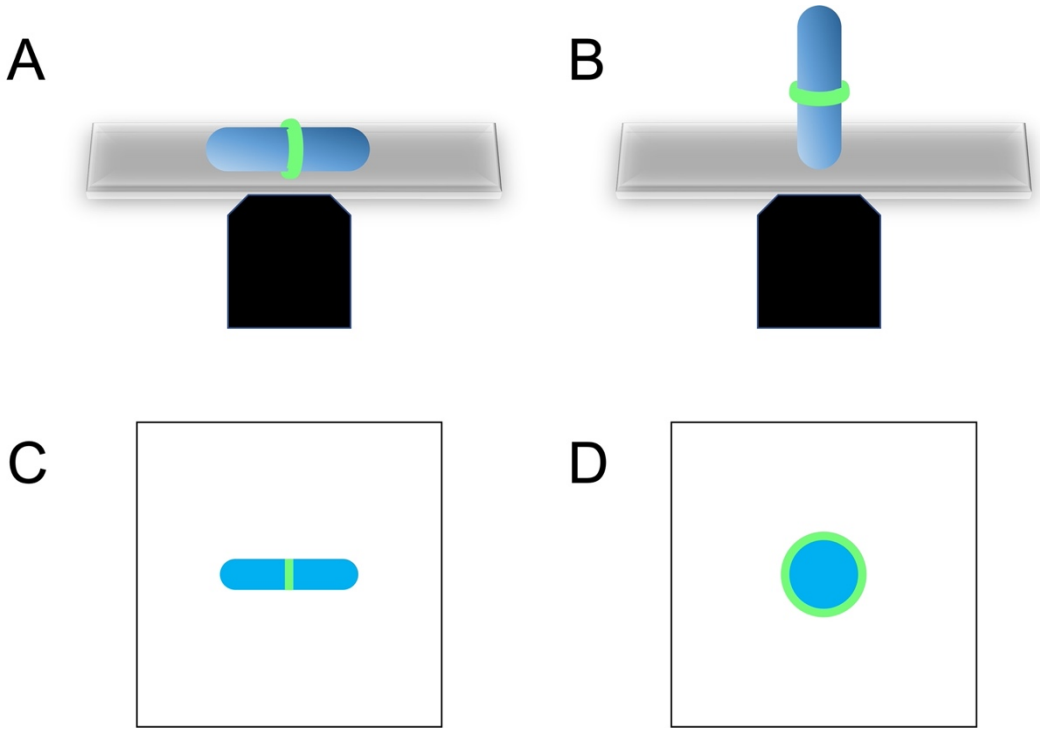

Figure 7.3: The effect of bacterial orientation on the quality of image produced. Orientation A, a side-on view, results in image C where the cell division machinery (green) can only be seen from one side which allows for the position of the cell division machinery along the length of the cell to be seen. Orientation B, a top-down view, results in image D where the entire cell division machinery can be seen as a cross section of the cell.

Visualising a bacterium with its longest axis parallel to the microscope objective, which is how a bacterium would naturally rest on a microscope slide, only allows for a portion of the cell division machinery to be observed because only one side of the bacteria is presented. This can be overcome using the optical sectioning capabilities of LSCM. The axial resolution of LSCM is much lower than the longitudinal and latitudinal resolution so by rotating the bacterium by 90°, so its longest axis is perpendicular to the microscope objective, the higher longitudinal and latitudinal resolution can be used to examine the cell division machinery instead of the lower

axial resolution. The highest possible lateral (x,y) resolution in a diffraction limited system is given by Abbe's equation:

$$d_{x,y} = \frac{\lambda}{2n \sin \theta} \qquad \textit{Equation 7.3}$$

Where λ is the wavelength of light, n is the refractive index of the material the light is travelling through and θ is the half angle of the spot the light converges on. Given the refractive index and spot size is fixed for any given microscope objective the equation can be simplified to:

$$d_{x,y} = \frac{\lambda}{2NA} \qquad \textit{Equation 7.4}$$

Where NA is the numerical aperture of an objective. This equation represents the shortest distance two point-source emitters of light can be resolved from one another at any given wavelength in the x and y (lateral) planes. To determine the shortest distance in the z plane a modified equation needs to be used:

$$d_z = \frac{\lambda n}{NA^2} \qquad \textit{Equation 7.5}$$

Which shows the axial resolution will always be lower than the lateral resolution in a diffraction limited system.

Since the cells were live during imaging a means of keeping the bacteria in this upright orientation had to be developed. There has been success in using patterned microscope coverslips to hold the bacteria in place during imaging.[121] This consisted of a series of holes on the surface of the coverslip into which the bacteria can slot and be imaged parallel to the microscope objective. The downside of this is that it uses electron-beam lithography and reactive ion-etching which are expensive and not readily available to all researchers, so a simpler more accessible technique was

developed. The proposed scaffolds and their working principle are depicted in figure 7.4.

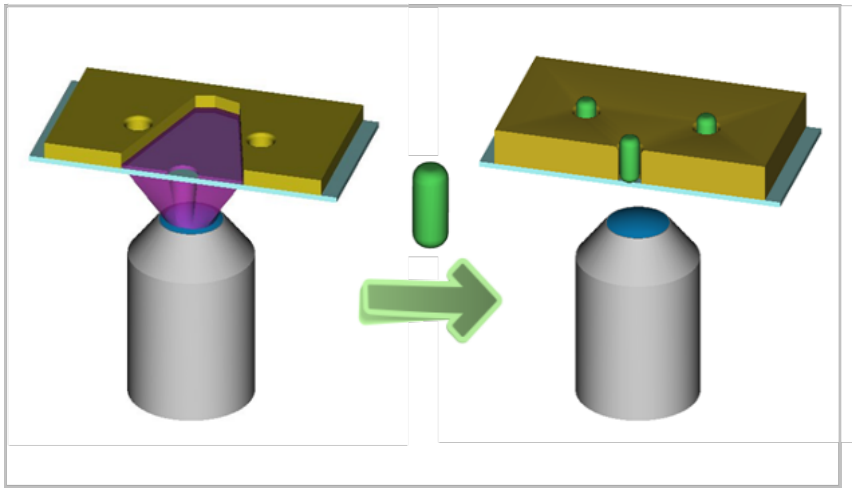

Figure 7.4: Left, principle of selective curing of UV curable resin using spatially patterned light. Right, proposed scaffold architecture with bacteria depicted as green rods slotted into the printed holes.

7.2. Optical Setup

To achieve micropatterning of the surface of coverslips to control the orientation of bacteria for imaging a simple optical setup was devised as depicted in figures 7.5 and 7.6 and the actual setup is shown in Figure 7.7.

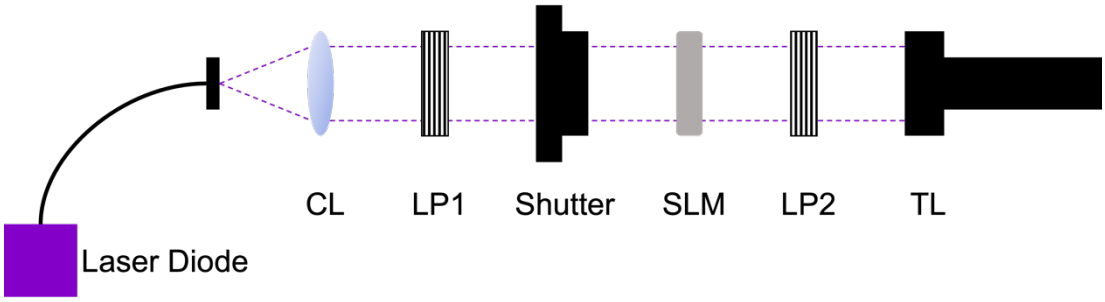

Figure 7.5: Pre microscope optical setup of printing setup. Coherent 405 nm light from the laser diode is focused into a fibre optic cable, once it emerges it is collimated by a collimating lens (CL). The light is polarised by a linear polarise (LP1) and passes through a shutter to block or allow the light to pass

through. The light passes through a spatial light modulator (SLM) which rotates the polarisation of some of the light passing through. The light passes through a second linear polariser (LP2) which is aligned orthogonally to LP1 which allows the light rotated by the SLM to pass through but blocks the rest. The light then passes through a tube lens (TL) and into the microscope.

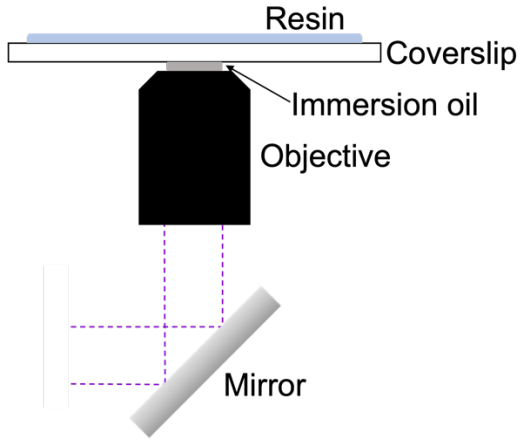

Figure 7.6: Internal microscope setup for printing apparatus. The light focused by the tube lens enters the microscope and is reflected by a dichroic mirror into the objective which focuses the image through the coverslip to the resin-coverslip interface to cure the resin where the light it projected but not where there is none present allowing for patterning of the surface of the coverslip.

Coherent monochromatic light with a wavelength of 405 nm was produced by a laser diode (Roithner Laser Technik, LD-405-200MGS) which was focused into a fibre optic cable (Ocean Optics, QP600-2-SR-BX) which transmitted it to the optical components. The light was collimated by a collimating lens (Thor Labs, LA1134) and was polarised by a linear polariser (Thor Labs, LPVISE100-A). A shutter was used to control when the light was transmitted further through the setup. The light then passed through a spatial light modulator (SLM) (Sony, LCX080AHJA, taken from a Hitachi CP-EX251N projector). This spatial light modulator was one of the three used by a projector to create an image and functions using the same working principle as an LCD display.

The SLM, shown in Figure 7.8 and its principle is shown in figure 7.9, is a transparent window consisting of a twisted nematic liquid crystal sandwiched between two glass substrates with transparent indium tin oxide on the surface. The glass substrate on one side has vertical ridges to align the liquid crystal to it and is split into pixels. Each pixel can individually apply a charge which travels through the liquid crystal to the conductive film on the other glass substrate which has horizontal ridges to align the liquid crystals. These orthogonal ridges mean the liquid crystal twists 90° from one side of the gap to the other. In pixels where no charge is applied (light pixels) the liquid crystals remain twisted 90° along the path and as linearly polarised light passes through the SLM it is rotated 90° meaning vertically aligned polarised light is now horizontally aligned. If a charge is applied (dark pixels) the liquid crystal in that pixel aligns along the electric field and the light is not rotated as it passes through the SLM so the vertically aligned polarised light remains as such. The SLM was controlled by connecting the projector to a desktop and treating it as a “third screen”.

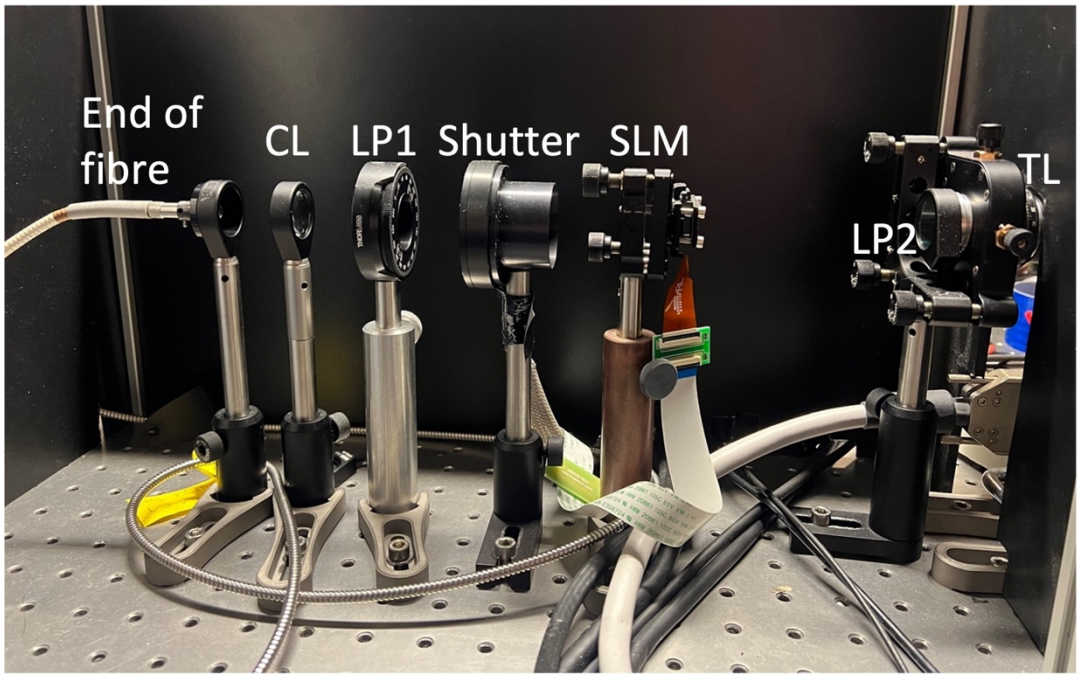

Figure 7.7: Photograph of printing apparatus with fibre on the left and microscope on the right. From the left, the end of the fibre from the laser diode, collimating lens (CL), first linear polariser (LP1), shutter, spatial light modulator (SLM), second linear polariser (LP2) and tube lens (TL) as the apparatus connect to the microscope.

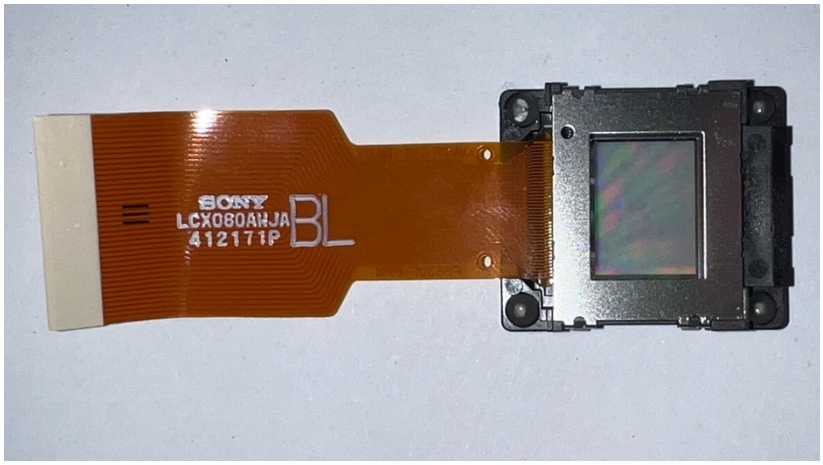

Figure 7.8: SLM used to generate patterned light. The small window on the right of the SLM is the liquid crystal panel and the ribbon cable on the left connects to the projector which is connected to a PC.

The light with varying rotations passed through a second linear polarised orthogonally aligned to the first linear polarised and only light that has been rotated 90° by the SLM can pass through resulting in an image being displayed. The light then passed through a tube lens (Thor Labs, TTL200MP) into the microscope (Leica, DMi8).

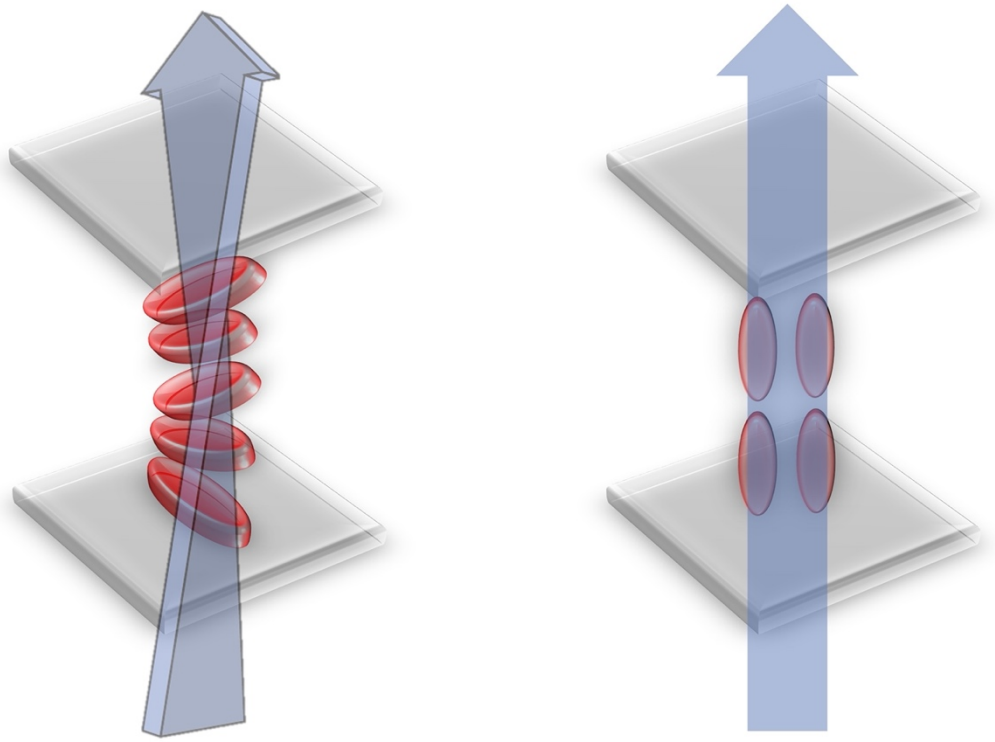

Figure 7.9: Principle of operation of the SLM to generate patterned light. The left shows the SLM in its rest mode with liquid crystals twisting 90° from one substrate to the other, this twists polarised light 90° resulting in a light pixel. When a voltage is applied the pixel changes to a dark pixel, right, and polarised light passes through unchanged.

Once in the microscope the light was reflected by a mirror into a 100x oil immersion objective (Leica, HC PL APO 100x/1,40 OIL CS2). The objective focused the light through immersion oil to the upper surface of the coverslip and the resin-coverslip interface. UV curable resin (Formlabs, RS-F2-GPCL-04) was evenly spread across the cover slip using a simple drop and smear technique, when exposed to 405 nm light

the resin polymerises and solidifies. The shutter was opened allowing the light to transmit and the image projected. In areas where the SLM had light pixels the transmitted light passed through all components and cured the resin in those areas but in areas with dark pixels the light could not pass through the second linear polariser and no resin was cured in those areas. This allowed for 3D patterns to be generated on the surface of the glass coverslip.

7.3. Printing Methodology

Two methods were used for creating scaffolds to align bacteria orthogonally to the cover slip surface using two different projected images shown in Figure 7.10A and 7.10B. Method one, using the projected image in figure 7.10A, printed a 3x3 square of the image onto the coverslip to generate many holes for the bacteria to slot into. The resulting scaffold is shown in figure 7.10C. Method one, using the projected image in figure 7.10B, traced a pattern with gaps to generate holes for the bacteria to slot into. The resulting scaffold is shown in figure 7.10D.

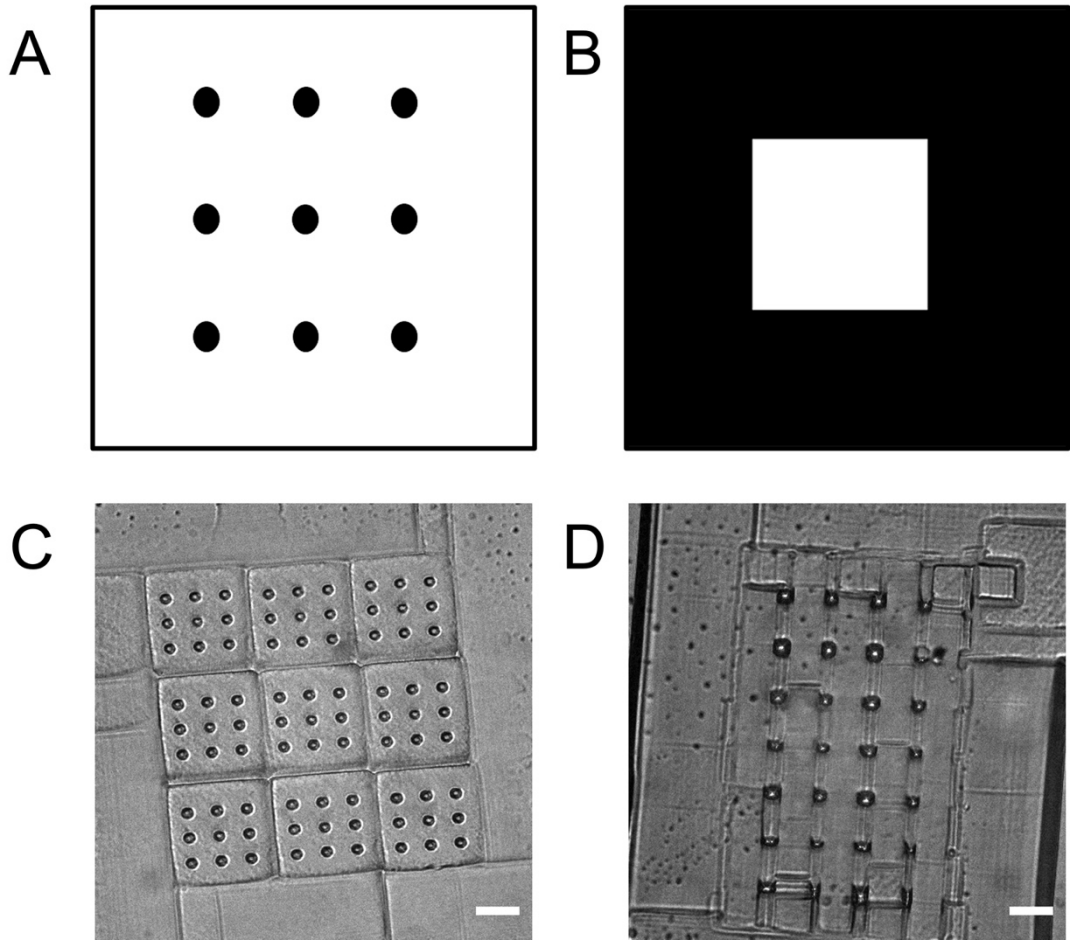

Figure 7.10: Images projected for micropatterning coverslips, and transmission microscopy of the resulting scaffolds generated. Image A was used to create scaffold C and image B was used to generate scaffold D. Scale bar = 25 µm.

Both methods produced vertical holes that could accommodate a single bacterium. The holes in the scaffold shown in figure 7.10C had an average diameter of 4.1 µm and the holes in the scaffold shown in figure 7.10D had ana average diameter of 5.4 µm. Given the typical diameter of a single *E. coli* bacterium is between 0.25-1 µm these holes would easily be able to accommodate a bacterium.[122] It was determined that the first method, projecting the image in figure 7.10A was far more reproducible than the alternative so it was the only method selected for experimental validation.

7.4. Validation

To ensure the holes printed were deep enough to accommodate a bacterium the resin used was doped with Rhodamine 6G, the excitation and emission spectra of which are shown in figure 7.11, so the 3D structure could be determined using LSCM. The inclusion of Rhodamine 6G did adversely affect the curing quality to a small degree but the scaffolds produced with it included were not visibly different to the scaffolds made without it.

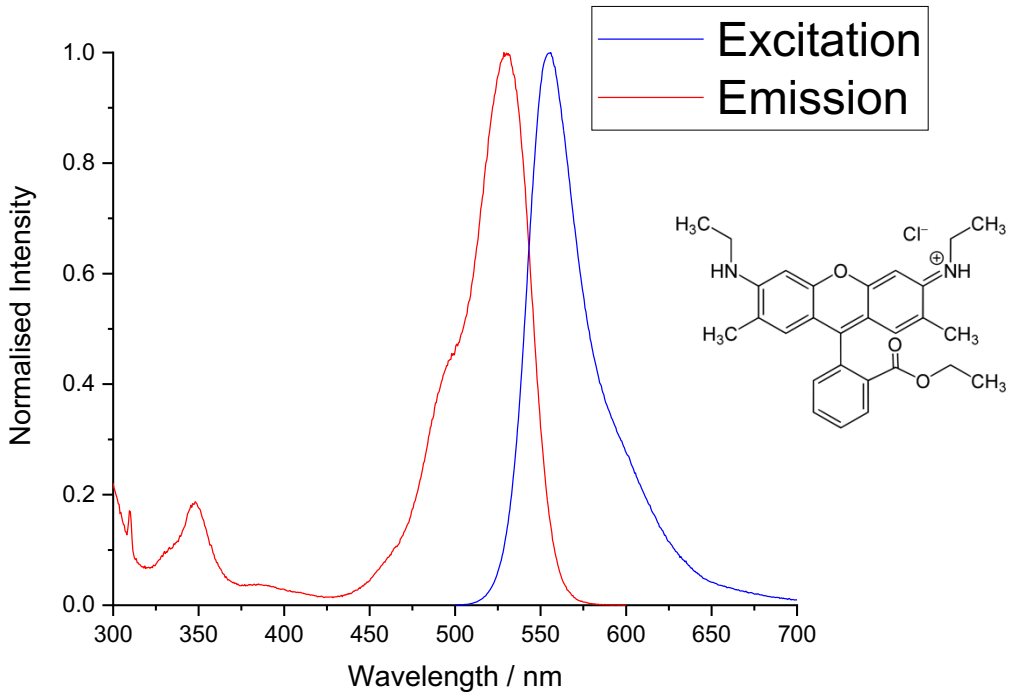

Figure 7.11: Excitation and emission spectra of Rhodamine 6G in ethanol. For the excitation spectrum (blue line) the λ_{em} = 620 nm. For the emission spectrum (red line) the λ_{ex} = 480 nm. Structure of Rhodamine 6G shown to the right.

Figure 7.12 shows a printed scaffold with Rhodamine 6G included. Figure 7.12A and 7.12B are the transmission image and fluorescence image respectively. The entire scaffold was imaged through multiple z slices using a confocal LSCM at 355 nm

excitation wavelength (Nd:YAG 3rd harmonic) x63 1.40 NA objective capable of 760nm axial resolution and 126 nm lateral resolution thanks to implementation of an auxiliary technique called PhMoNa[123] and were merged to give a 3D projection of the image. Figure 7.12C is the 3D projection viewed from above, figure 7.12D is the 3D projection viewed from the side and figure 7.12E is the 3D projection from below.

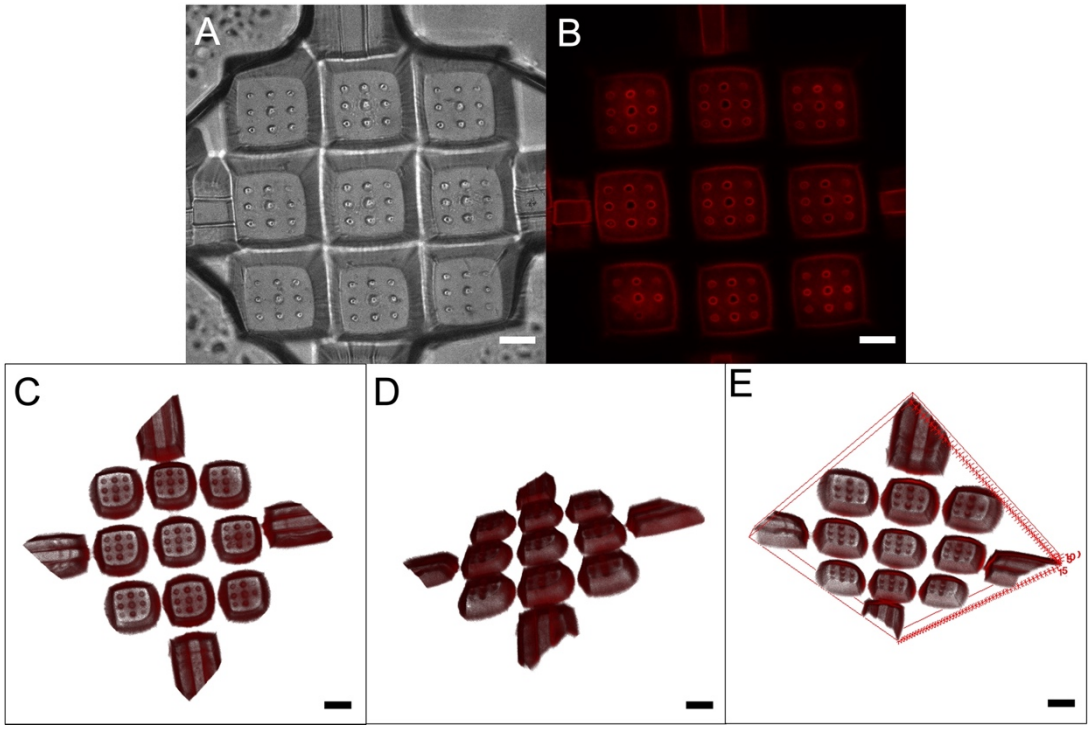

Figure 7.12: Printed scaffold with Rhodamine 6G included in the resin. A, Transmission image. B, fluorescence image of one slice roughly halfway through the scaffold's height. C,D,E, 3D projection of the full scaffold shown from above, the side and below respectively. Each z slice had a height of 0.79 µm giving a total height of the scaffold of 19.75 µm. Scale bar = 25 µm.

These images show that the holes printed are hollow and that channel continues to the bottom of the coverslip allowing enough room for a bacterium to be accommodated. To ensure holes were accessible and liquid, and by extension bacteria, could enter the holes and displace any air trapped in the cavity, Rhodamine

6G was added to LB media and imaged as with figure 7.13. Figure 7.13A and 7.13B are transmission and fluorescence images, respectively, while figure 7.13C is the 3D projection viewed from above and figure 7.13D the 3D projection viewed from below.

These results confirm the media can penetrate the holes and displace any air present. The LB media with Rhodamine 6G added does not reach the bottom of the holes, only reaching about half of the distance down the holes, however, given a typical *E. coli* bacterium is typically less than 1 µm this is not an issue because the media was able to penetrate at least 8 µm. This is significantly larger than the bacterium so could pose issues such as multiple bacteria entering each cavity. The thickness of the scaffold, and therefore the depth of the holes, was difficult to reduce below these sizes because it is dictated by the thickness of the UV-curable resin layer and even more so by the length of time the resin was exposed to the patterned UV light. The thickness of the resin layer cannot be reduced further because of the limitations of the simple drop and smear technique. The time the resin was exposed to the patterned light could not be reduced further as it was already the minimum period necessary to achieve full curing. Selective 3D ROI region of interest patterning using a confocal microscope with a 355 nm or 405 nm laser and a high precision automated piezo stage is a possible solution, but due to the extensive and tedious work this would require and the limited improvement it would provide this was not attempted.

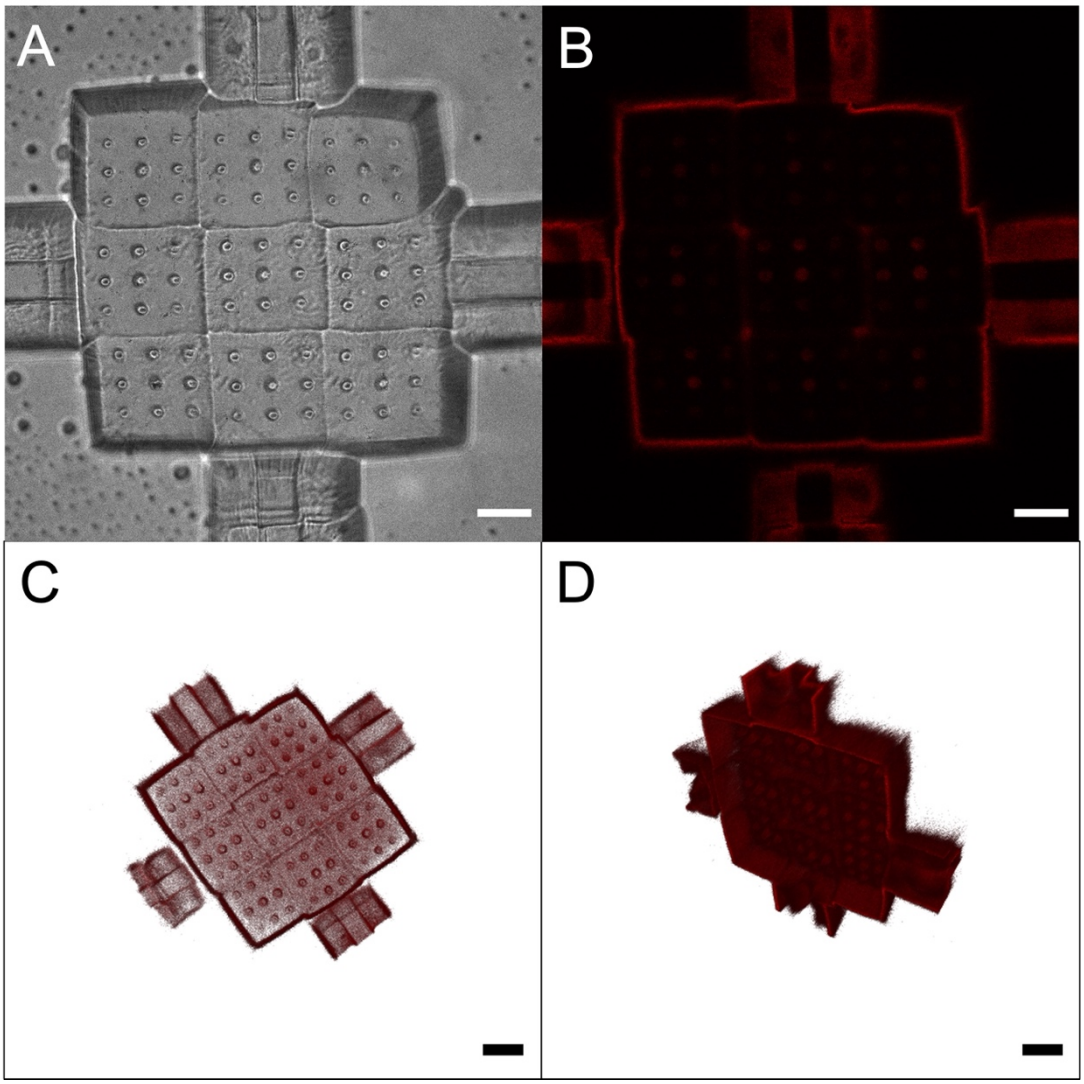

Figure 7.13: Printed scaffold with Rhodamine 6G added to LB media. A, Transmission image. B, fluorescence image of one slice roughly halfway through the scaffold's height. C,D, 3D projection of the full scaffold shown from above and below respectively. Each z slice had a height of 0.79 µm giving a total height of the scaffold of 18.17 µm. Scale bar = 25 µm.

To conclusively show these scaffolds can be used to capture bacteria and allow them to be imaged in different orientations, *E. coli* BL21-AI cells were stained with DAPI and applied to a concave well slide. A coverslip with a printed scaffold added and sealed. Figure 7.14 shows an image of one section of a 3x3 printed scaffold with bacteria successfully accommodated within the holes. Figure 7.14A shows one optical

section highlighting two holes containing bacterial cells with the scaffold stained with Rhodamine 6G, while Figure 7.14B shows a transmission image of the scaffold with one optical section of DAPI fluorescence overlayed.

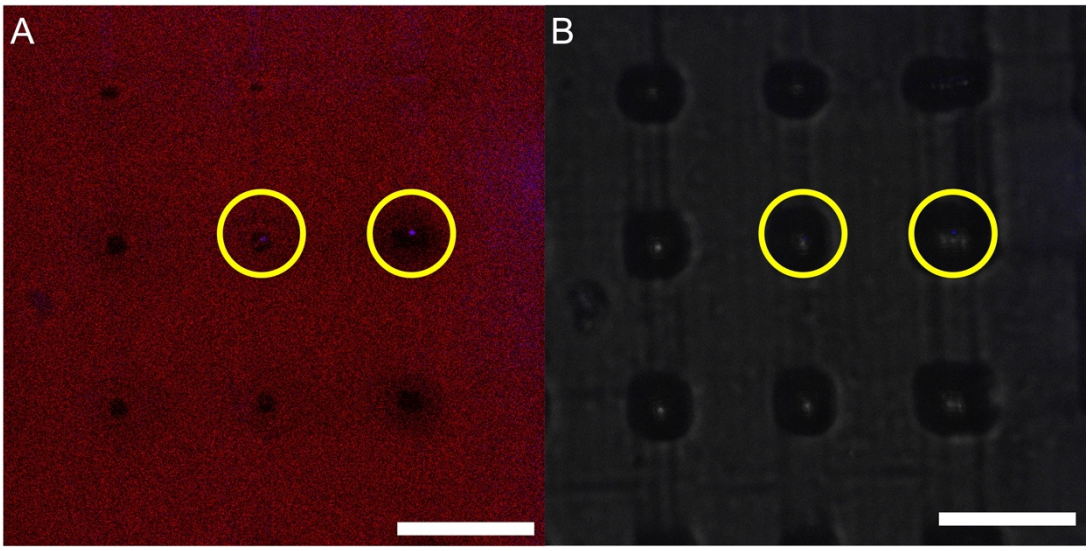

Figure 7.14: Printed scaffold with Rhodamine 6G added to resin and DAPI-stained E. coli BL21-AI added. A, fluorescence image of Rhodamine 6G, red, and DAPI stained bacteria, blue. B, transmission image with DAPI fluorescence from one optical section overlayed. The two holes circled with yellow are those with bacteria visible in the optical section. Scale bar = 25 µm.

Figure 7.15 shows a 3D projection of the DAPI fluorescence as shown in figure 7.14 showing that more than two bacteria are present in the 9 holes shown.

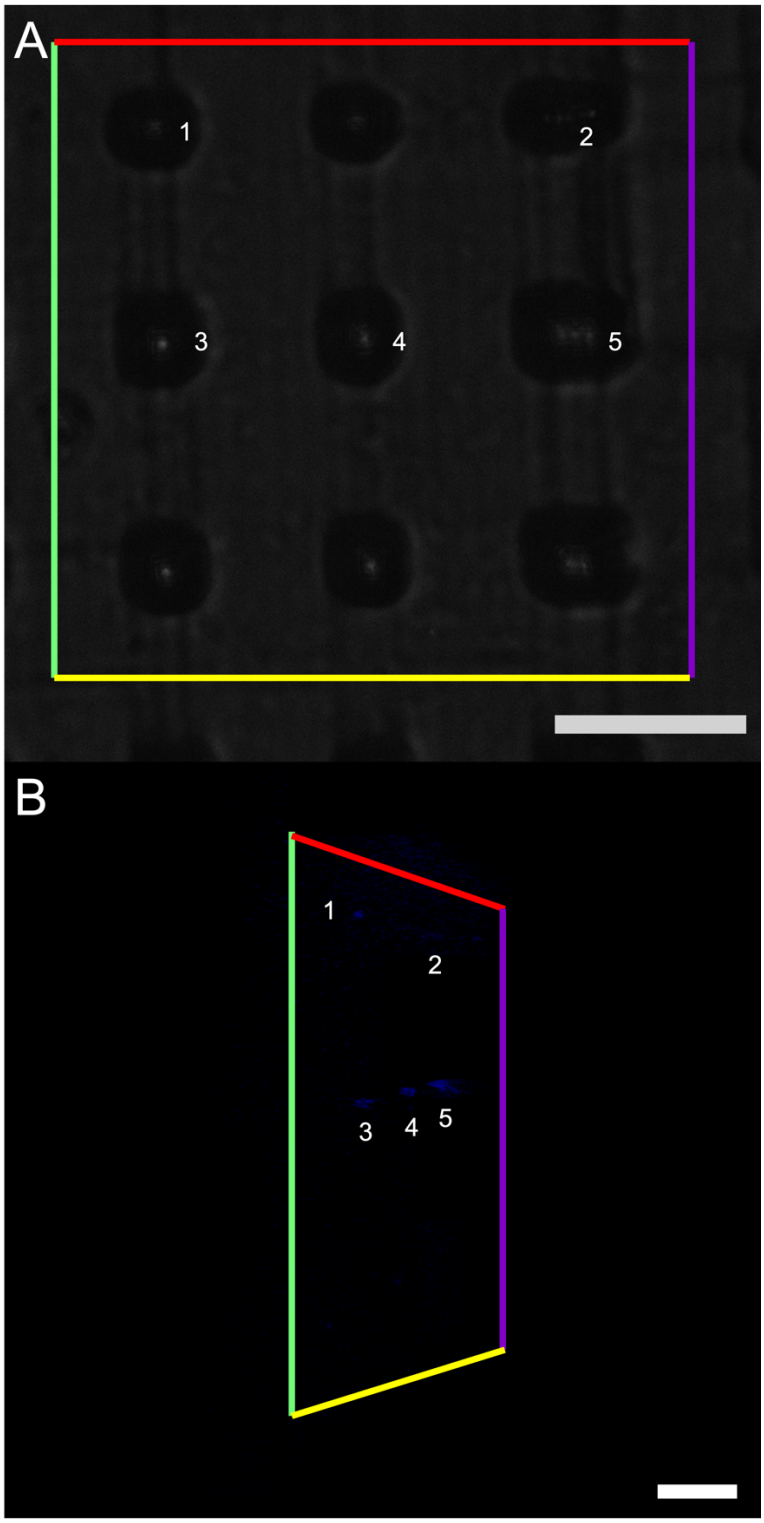

Figure 7.15: 3D projection of DAPI stained BL21-AI E. coli impregnated into printed scaffold. A, transmission image of the scaffold with a coloured border showing the orientation of the rotation in the 3D projection and the holes numbered corresponding to the five bacteria present in the whole scaffold. B, 3D projection of the DAPI fluorescence with the orientation denoted by the coloured border and the bacteria numbered to correspond to the holes in A. Scale bar = 25 µm.

This shows that five bacteria are present in this section of the scaffold and all of them have an orthogonal orientation to the objective improving the possible resolution. A total of 12 3x3 grid prints (of the kind shown in figure 7.10C) were tested with DAPI stained *E. coli* BL21-AI and all of them had bacteria appropriately inserted. The average number of bacteria present in each print was 38. None of the prints tested had more than one bacterium in each printed hole and all the bacteria were in the top of the hole with no cell lower than 5 µm.

7.5. Construction of CFP and YFP fusion plasmids

In order to exploit the micropatterned coverslips and investigate the interactions between bacteriophage proteins and the bacterial dividing ring, each protein needs to be fused to a fluorescent protein that allows for FRET to occur when the two proteins are in close proximity. Cyan fluorescent protein (CFP) and yellow fluorescent protein (YFP) were chosen for this.

The YFP and CFP need to be fused to the proteins of interest, so they are expressed together as one protein unit bonded together. To do this, the YFP and CFP genes need to be inserted into the plasmids containing the *ftsZ* and phage protein genes. The decision of whether to combine the FtsZ protein or phage proteins to either YFP or CFP is not arbitrary. The CFP unit transfers energy to the YFP unit. If the CFP is fused to the *ftsZ* gene, excitation of that protein will result in constant fluorescence of the FtsZ dividing ring and the phage proteins would fluoresce yellow when in proximity. In contrast, if the CFP is fused to the phage proteins, they would constantly fluoresce

and the FtsZ ring would only fluoresce (yellow) when the phage proteins are in proximity.

Each option is viable, but the strategy chosen was to fuse CFP to the FtsZ ring and YFP to the phage proteins. The reason for this is a practical one; in order to obtain useable images, the area of interest needs to be in focus on the microscope. It is easier to focus on the FtsZ ring if it is fluorescing and it would fluoresce consistently if the CFP is fused to it which wouldn't be the case if YFP was fused to it. Once in focus the detector can be tuned to emission wavelength range of YFP and images can be taken to see if there is any FRET.

7.6. Conclusions and Future Work

A minimal cost, accessible and reproducible technique for producing microscope coverslips with microscale patterning has been developed and validated. This allows for the alignment of individual bacteria and restricting them to have their long axis (in the case of rod-shaped bacteria) perpendicular to the coverslip resulting in increased microscopical resolution for the cross section of the bacteria.

This technique could also be used to design and manufacture any small microstructure onto glass coverslips for cell manipulation, not only in microbiology but in mammalian cell culture where precise control of cell orientation and growth pattern is imperative to allow effective visualisation of cells.

Future work would focus on completing construction of CFP-YFP fusions of phage proteins and FtsZ to allow visualisation of the interactions between the bacteriophage proteins and the FtsZ dividing ring.

8. Conclusions

This thesis has focused on two separate but related approaches to developing new antimicrobial agents to combat antimicrobial resistance. The first part of this thesis focussed on using chelating compounds to kill bacteria and/or reduce their viability and therefore their ability to multiply. The second part of this thesis focussed bacteriophage proteins that are analogues of endogenous bacterial proteins that are involved in cell division and the affect that they have on bacterial division and morphology when they are overexpressed in bacteria.

Chelants are widely used in many industries to prevent microbial growth including the pharmaceutical, food and cosmetic industries; despite their widespread use the mechanism of action is not well understood. Traditional theory holds that their mechanism of action is mostly through metal ion sequestration causing starvation of these essential trace elements for bacterial survival. However, in this thesis, it has been shown that this is not the only mechanism of action and two alternative modes of growth inhibition have been proposed. Six chelants were tested on three species of bacteria. The chelants (EDTA, DTPMP, caprylhydroxamic acid, fusaric acid, tropolone and hinokitiol) are of commercial interest to be used as bacteriostatic and/or bactericidal agents in various commercial products. The species investigated (*E. coli, S. marcescens and S. aureus)* are all potentilly pathogenic and model organisms so provide a solid grounding for future work.

In chapter 3 of this thesis, it was shown that for some chelants there is a degree of membrane damage to bacteria upon exposure. EDTA was shown to cause damage to both the inner and outer membrane of *E. coli* but not in the other two species tested. DTPMP caused damage to the outer and inner membranes of both *E. coli* and *S. marcescens* as well as damage to the membrane of *S. aureus.* Caprylhydroxamic acid damaged both membranes in both *E. coli* and *S. marcescens* but had no effect on the membrane of *S. aureus*. Fusaric acid damage only the inner membrane of *E. coli* but had no effect on its outer peptidoglycan composed outer membrane. The structurally similar tropolone and hinokitiol did not appear to have a significant effect on the membranes of any of the species tested. The damage caused to the membranes by chelants is hypothesised to be due to sequestration of metal ions essential to membrane structure.

In chapter 4 the redox environment of bacteria exposed to chelants was investigated. This was done because trace metal ions are essential for redox reactions that take place inside bacteria so disruption of the availability of metal ions could cause changes in the redox environment. All the chelants tested, except for caprylhydroxamic acid, were found to cause a decrease in the intracellular oxidative capacity of the bacteria upon exposure. For EDTA, DTPMP and fusaric acid it is proposed that this is due to a reduced availability of iron and manganese to the bacteria that are essential for normal cell redox functions. In tropolone and hinokitiol there is some evidence to suggest that they work intracellularly and directly reduce the oxidative capacity, acting directly as antioxidants rather than chelants. For caprylhydroxamic acid, the oxidative action in the bacteria is dramatically increased,

possibly by being positioned in the membrane (given its surfactant like structure) and providing more metal ions to the individual cell causing an overload of metal and damaging the cell through excess oxidation of vital cell components.

In chapter 5 strains of *S. aureus* that had developed resistance to chelants were investigated, in particular changes to their morphology. The strains were exposed to either EDTA or DTPMP and their genome sequenced to determine the mutations that allowed them to develop resistance. Many of these mutations were related to membrane synthesis and regulation. The morphology, including size and shape and intercellular interaction of these strains were investigated and it was found that for most of the strains there was a contraction in cell size and the cells did not cluster as much as the wild type strain. There was an increase in cell surface negativity which could explain the decreased intercellular interactions and a change in cell wall thickness to decrease chelant uptake explain the decrease in cell size.

In chapter 6 bacteriophage proteins were investigated and the effect overexpression of these proteins in *E. coli*. All the proteins caused drastic cell lengthening and filamentation because they mimic and disrupt the proteins that facilitate cell division. This is the cause of cell death when these proteins are expressed because the cell is no longer able to regulate its processes effectively. Additionally the proteins disrupt the proteins that fold the bacteria DNA causing an abnormal distribution of DNA throughout the cell potentially making it harder for the bacteria to express proteins effectively.

9. References

1. Kardos, N. & Demain, A. L. Penicillin: the medicine with the greatest impact on therapeutic outcomes. *Appl Microbiol Biotechnol* **92**, 677–687 (2011).
2. Schatz, A., Bugle, E. & Waksman, S. A. Streptomycin, a Substance Exhibiting Antibiotic Activity Against Gram-Positive and Gram-Negative Bacteria.* . *Exp Biol Med* **55**, 66–69 (1944).
3. Cassini, A. *et al.* Attributable deaths and disability-adjusted life-years caused by infections with antibiotic-resistant bacteria in the EU and the European Economic Area in 2015: a population-level modelling analysis. *Lancet Infect Dis* **19**, 56–66 (2019).
4. Gould, K. Antibiotics: from prehistory to the present day. *Journal of Antimicrobial Chemotherapy* **71**, 572–575 (2016).
5. Aminov, R. I. A Brief History of the Antibiotic Era: Lessons Learned and Challenges for the Future. *Front Microbiol* **1**, (2010).
6. Darby, E. M. *et al.* Molecular mechanisms of antibiotic resistance revisited. *Nat Rev Microbiol* **21**, 280–295 (2023).
7. Walsh, C. Molecular mechanisms that confer antibacterial drug resistance. *Nature* **406**, 775–781 (2000).
8. Haq, I. U., Chaudhry, W. N., Akhtar, M. N., Andleeb, S. & Qadri, I. Bacteriophages and their implications on future biotechnology: a review. *Virol J* **9**, 9 (2012).
9. Padilla-Sanchez, V. Structural Model of Bacteriophage T4. *WikiJournal of Science* **4**, 5 (2021).

10. Fiers, W. *et al.* Complete nucleotide sequence of bacteriophage MS2 RNA: primary and secondary structure of the replicase gene. *Nature* **260**, 500–507 (1976).

11. Al-Shayeb, B. *et al.* Clades of huge phages from across Earth's ecosystems. *Nature* **578**, 425–431 (2020).

12. Fauquet, C. M. Taxonomy, Classification and Nomenclature of Viruses. in *Encyclopedia of Virology* 9–23 (Elsevier, 2008). doi:10.1016/B978-012374410-4.00509-4.

13. Wommack, K. E. & Colwell, R. R. Virioplankton: Viruses in Aquatic Ecosystems. *Microbiology and Molecular Biology Reviews* **64**, 69–114 (2000).

14. Weigel, C. & Seitz, H. Bacteriophage replication modules. *FEMS Microbiol Rev* **30**, 321–381 (2006).

15. Yannone, S. M., Hartung, S., Menon, A. L., Adams, M. W. & Tainer, J. A. Metals in biology: defining metalloproteomes. *Curr Opin Biotechnol* **23**, 89–95 (2012).

16. Waldron, K. J. & Robinson, N. J. How do bacterial cells ensure that metalloproteins get the correct metal? *Nat Rev Microbiol* **7**, 25–35 (2009).

17. Waldron, K. J., Rutherford, J. C., Ford, D. & Robinson, N. J. Metalloproteins and metal sensing. *Nature* **460**, 823–830 (2009).

18. Andreini, C., Bertini, I., Cavallaro, G., Holliday, G. L. & Thornton, J. M. Metal ions in biological catalysis: from enzyme databases to general principles. *JBIC Journal of Biological Inorganic Chemistry* **13**, 1205–1218 (2008).

19. Hood, M. I. & Skaar, E. P. Nutritional immunity: transition metals at the pathogen–host interface. *Nat Rev Microbiol* **10**, 525–537 (2012).

20. Imlay, J. A. The Mismetallation of Enzymes during Oxidative Stress. *Journal of Biological Chemistry* **289**, 28121–28128 (2014).

21. Koppenol, W. H. The centennial of the Fenton reaction. *Free Radic Biol Med* **15**, 645–651 (1993).

22. Sánchez, P., Gálvez, N., Colacio, E., Miñones, E. & Domínguez-Vera, J. M. Catechol releases iron(iii) from ferritin by direct chelation without iron(ii) production. *Dalton Trans.* 811–813 (2005).

23. Paterson, J. R. *et al.* Insights into the Antibacterial Mechanism of Action of Chelating Agents by Selective Deprivation of Iron, Manganese, and Zinc. *Appl Environ Microbiol* **88**, (2022).

24. Tenover, F. C. Mechanisms of Antimicrobial Resistance in Bacteria. *Am J Med* **119**, S3–S10 (2006).

25. Founou, R. C., Founou, L. L. & Essack, S. Y. Clinical and economic impact of antibiotic resistance in developing countries: A systematic review and meta-analysis. *PLoS One* **12**, e0189621 (2017).

26. Muramatsu, I., Murakami, M., Yoneda, T. & Hagitani, A. The Formylation of Amino Acids with Acetic Formic Anhydride. *Bull Chem Soc Jpn* **38**, 244–246 (1965).

27. Schindler, M. & Osborn, M. J. Interaction of divalent cations and polymyxin B with lipopolysaccharide. *Biochemistry* **18**, 4425–4430 (1979).

28. Crutcher, F. K. *et al.* Microbial Resistance Mechanisms to the Antibiotic and Phytotoxin Fusaric Acid. *J Chem Ecol* **43**, 996–1006 (2017).

29. Jain, S. Can EDTA Change MRSA into MSSA? A Future Prospective! *JOURNAL OF CLINICAL AND DIAGNOSTIC RESEARCH* **10**, DC22–DC25 (2016).

30. Smith, S. W. The Role of Chelation in the Treatment of Other Metal Poisonings. *Journal of Medical Toxicology* **9**, 355–369 (2013).

31. Alakomi, H.-L., Saarela, M. & Helander, I. M. Effect of EDTA on Salmonella enterica serovar Typhimurium involves a component not assignable to lipopolysaccharide release. *Microbiology (N Y)* **149**, 2015–2021 (2003).

32. Beecroft, M. *Antimicrobial Chelators and their Mechanism of Action Antimicrobial Chelators and their Mechanism of Action*. http://etheses.dur.ac.uk/12933/ (2019).

33. Paterson, J. *Characterisation of the mode of action of chelating agents against Gram-negative and Gram-positive bacteria*. http://etheses.dur.ac.uk/14340/ (2021).

34. Rott, E., Steinmetz, H. & Metzger, J. W. Organophosphonates: A review on environmental relevance, biodegradability and removal in wastewater treatment plants. *Science of The Total Environment* **615**, 1176–1191 (2018).

35. Drzyzga, D., Forlani, G., Vermander, J., Kafarski, P. & Lipok, J. Biodegradation of the aminopolyphosphonate DTPMP by the cyanobacterium *A nabaena variabilis* proceeds via a C-P lyase-independent pathway. *Environ Microbiol* **19**, 1065–1076 (2017).

36. Cardiano, P. *et al.* On the complexation of metal cations with “pure” diethylenetriamine-N,N,N’,N’’,N’’-pentakis(methylenephosphonic) acid. *New Journal of Chemistry* **41**, 4065–4075 (2017).

37. Oakes, J. & van Kralingen, C. G. Spectroscopic studies of transition-metal ion complexes of diethylenetriaminepenta-acetic acid and

diethylenetriaminepenta-methylphosphonic acid. *Journal of the Chemical Society, Dalton Transactions* 1133 (1984).

38. Alam, M. A. Methods for Hydroxamic Acid Synthesis. *Curr Org Chem* **23**, 978–993 (2019).

39. Bellotti, D. & Remelli, M. Deferoxamine B: A Natural, Excellent and Versatile Metal Chelator. *Molecules* **26**, 3255 (2021).

40. Bacon, C. W., Porter, J. K., Norred, W. P. & Leslie, J. F. Production of fusaric acid by Fusarium species. *Appl Environ Microbiol* **62**, 4039–4043 (1996).

41. Stipanovic, R. D., Puckhaber, L. S., Liu, J. & Bell, A. A. Phytotoxicity of fusaric acid and analogs to cotton. *Toxicon* **57**, 176–178 (2011).

42. Bacon, C. W., Hinton, D. M. & Hinton, A. Growth-inhibiting effects of concentrations of fusaric acid on the growth of Bacillus mojavensis and other biocontrol Bacillus species. *J Appl Microbiol* **100**, 185–194 (2006).

43. Hai, Y., Chen, M., Huang, A. & Tang, Y. Biosynthesis of Mycotoxin Fusaric Acid and Application of a PLP-Dependent Enzyme for Chemoenzymatic Synthesis of Substituted <scp>l</scp> -Pipecolic Acids. *J Am Chem Soc* **142**, 19668–19677 (2020).

44. Ghag, S. B., Shekhawat, U. K. S. & Ganapathi, T. R. Petunia Floral Defensins with Unique Prodomains as Novel Candidates for Development of Fusarium Wilt Resistance in Transgenic Banana Plants. *PLoS One* **7**, e39557 (2012).

45. Ruiz, J. A., Bernar, E. M. & Jung, K. Production of Siderophores Increases Resistance to Fusaric Acid in Pseudomonas protegens Pf-5. *PLoS One* **10**, e0117040 (2015).

46. Trust, T. J. Antibacterial Activity of Tropolone. *Antimicrob Agents Chemother* **7**, 500–506 (1975).

47. Diouf, P. N. *et al.* Influence of Tropolone on *Poria placenta* Wood Degradation. *Appl Environ Microbiol* **68**, 4377–4382 (2002).

48. Jacobsen, J. A., Major Jourden, J. L., Miller, M. T. & Cohen, S. M. To bind zinc or not to bind zinc: An examination of innovative approaches to improved metalloproteinase inhibition. *Biochimica et Biophysica Acta (BBA) - Molecular Cell Research* **1803**, 72–94 (2010).

49. Bryant, B. E., Fernelius, W. C. & Douglas, B. E. Formation Constants of Metal Complexes of Tropolone and Its Derivatives. I. Tropolone [1]. *J Am Chem Soc* **75**, 3784–3786 (1953).

50. Park, J., Lee, H.-H., Jung, H. & Seo, Y.-S. Transcriptome analysis to understand the effects of the toxoflavin and tropolone produced by phytopathogenic Burkholderia on Escherichia coli. *Journal of Microbiology* **57**, 781–794 (2019).

51. Fullagar, J. L. *et al.* Antagonism of a zinc metalloprotease using a unique metal-chelating scaffold: tropolones as inhibitors of P. aeruginosa elastase. *Chemical Communications* **49**, 3197 (2013).

52. Nakano, K. *et al.* Discovery and characterization of natural tropolones as inhibitors of the antibacterial target CapF from Staphylococcus aureus. *Sci Rep* **5**, 15337 (2015).

53. Coombs, R. W. & Trust, T. J. The effect of light on the antibacterial activity of β-thujaplicin. *Can J Microbiol* **19**, 1177–1180 (1973).

54. Neopane, P., Nepal, H. P., Shrestha, R., Uehara, O. & Abiko, Y. In vitro biofilm formation by Staphylococcus aureus isolated from wounds of

hospital-admitted patients and their association with antimicrobial resistance. *Int J Gen Med* **Volume 11**, 25–32 (2018).

55. MORITA, Y. *et al.* The Mechanism of the Bactericidal Activity of Hinokitiol. *Biocontrol Sci* **12**, 101–110 (2007).

56. Lyczko, K., Lyczko, M. & Starosta, W. *catena* -Poly[(μ 3 -2-hydroxy-4-isopropylcyclohepta-2,4,6-trien-1-onato)(μ 2 -2-hydroxy-4-isopropylcyclohepta-2,4,6-trien-1-onato)lead(II)]. *Acta Crystallogr Sect E Struct Rep Online* **66**, m1395–m1396 (2010).

57. Wollman, A. J. M., Nudd, R., Hedlund, E. G. & Leake, M. C. From animaculum to single molecules: 300 years of the light microscope. *Open Biology* vol. 5 Preprint at https://doi.org/10.1098/rsob.150019 (2015).

58. Hooke, R. *Micrographia : or, Some physiological descriptions of minute bodies made by magnifying glasses. With observations and inquiries thereupon / By R. Hooke*. (Printed by Jo. Martyn and Ja. Allestry, printers to the Royal Society, and are to be sold at their shop at the Bell in St. Paul's Churchyard, 1665).

59. US3013467.

60. Pal, R. Phase modulation nanoscopy: a simple approach to enhanced optical resolution. *Faraday Discuss* **177**, 507–515 (2015).

61. Schindelin, J. *et al.* Fiji: an open-source platform for biological-image analysis. *Nat Methods* **9**, 676–682 (2012).

62. Coico, R. Gram Staining. *Curr Protoc Microbiol* **00**, A.3C.1-A.3C.2 (2006).

63. Huang, K. C., Mukhopadhyay, R., Wen, B., Gitai, Z. & Wingreen, N. S. Cell shape and cell-wall organization in Gram-negative bacteria. *Proceedings of the National Academy of Sciences* **105**, 19282–19287 (2008).

64. Miller, S. I. Antibiotic Resistance and Regulation of the Gram-Negative Bacterial Outer Membrane Barrier by Host Innate Immune Molecules. *mBio* **7**, e01541-16 (2016).

65. Delcour, A. H. Outer membrane permeability and antibiotic resistance. *Biochimica et Biophysica Acta (BBA) - Proteins and Proteomics* **1794**, 808–816 (2009).

66. Choi, U. & Lee, C.-R. Distinct Roles of Outer Membrane Porins in Antibiotic Resistance and Membrane Integrity in Escherichia coli. *Front Microbiol* **10**, (2019).

67. Helander, I. M. & Mattila-Sandholm, T. Fluorometric assessment of Gram-negative bacterial permeabilization. *J Appl Microbiol* **88**, 213–219 (2000).

68. US5436134.

69. Stocks, S. M. Mechanism and use of the commercially available viability stain,BacLight. *Cytometry* **61A**, 189–195 (2004).

70. Stiefel, P., Schmidt-Emrich, S., Maniura-Weber, K. & Ren, Q. Critical aspects of using bacterial cell viability assays with the fluorophores SYTO9 and propidium iodide. *BMC Microbiol* **15**, (2015).

71. Santos, T. M. A. *et al.* Small Molecule Chelators Reveal That Iron Starvation Inhibits Late Stages of Bacterial Cytokinesis. *ACS Chem Biol* **13**, 235–246 (2018).

72. Angerer, A., Klupp, B. & Braun, V. Iron transport systems of Serratia marcescens. *J Bacteriol* **174**, 1378–1387 (1992).

73. Friedman, D. B. *et al.* Staphylococcus aureus Redirects Central Metabolism to Increase Iron Availability. *PLoS Pathog* **2**, e87 (2006).

74. Pishchany, G., Haley, K. P. & Skaar, E. P. Staphylococcus aureus Growth using Human Hemoglobin as an Iron Source. *Journal of Visualized Experiments* (2013).

75. Kahn, V. & Andrawis, A. *Pnnted m Great Bntam INHIBITION OF MUSHROOM TYROSINASE BY TROPOLONE**. vol. 24 (1985).

76. Fullagar, J. L. *et al.* Antagonism of a zinc metalloprotease using a unique metal-chelating scaffold: tropolones as inhibitors of P. aeruginosa elastase. *Chemical Communications* **49**, 3197 (2013).

77. Nieva-Gomez, D. & Gennis, R. B. Affinity of intact Escherichia coli for hydrophobic membrane probes is a function of the physiological state of the cells. *Proceedings of the National Academy of Sciences* **74**, 1811–1815 (1977).

78. Nieva-Gomez, D., Konisky, J. & Gennis, R. B. Membrane changes in Escherichia coli induced by colicin Ia and agents known to disrupt energy transduction. *Biochemistry* **15**, 2747–2753 (1976).

79. Helgerson, S. L. & Cramer, W. A. *Changes in Escherichia coli Cell Envelope Structure and the Sites of Fluorescence Probe Binding Caused by Carbonyl Cyanide p-Trifluoromethoxyphenylhydrazonet*.

80. Sedgwick, E. G. & Bragg, P. D. The fluorescence intensity of the lipophilic probe N-phenyl-1-naphthylamine responds to the oxidation-reduction state of purified Escherichia coli cytochrome o incorporated into phospholipid vesicles. *FEBS Lett* **229**, 127–130 (1988).

81. Helgerson, S. L. & Cramer, W. A. *Changes in E. Coli Cell Envelope Structure Caused by Uncouplers of Active Transport and Colicin E l*. *Journal of Supramolecular Structure* vol. 5 (1976).

82. Morita1, Y. *The Mechanism of the Bactericidal Activity of Hinokitiol*. *Biocontrol Science* vol. 12 (2007).

83. Paiva, C. N. & Bozza, M. T. Are Reactive Oxygen Species Always Detrimental to Pathogens? *Antioxid Redox Signal* **20**, 1000–1037 (2014).

84. Zhao, X. & Drlica, K. Reactive oxygen species and the bacterial response to lethal stress. *Curr Opin Microbiol* **21**, 1–6 (2014).

85. Fasnacht, M. & Polacek, N. Oxidative Stress in Bacteria and the Central Dogma of Molecular Biology. *Front Mol Biosci* **8**, (2021).

86. Waggoner, B. T., Wade, T. & Pato, M. L. Identification of the bacteriophage D108 kil gene and of the second region of sequence nonhomology with bacteriophage Mu. *Gene* **62**, 111–119 (1988).

87. Kim, H. & Xue, X. Detection of Total Reactive Oxygen Species in Adherent Cells by 2',7'-Dichlorodihydrofluorescein Diacetate Staining. *Journal of Visualized Experiments* e60682 (2020).

88. Gomes, A., Fernandes, E. & Lima, J. L. F. C. Fluorescence probes used for detection of reactive oxygen species. *J Biochem Biophys Methods* **65**, 45–80 (2005).

89. Wang, H. & Joseph, J. A. Quantifying cellular oxidative stress by dichlorofluorescein assay using microplate reader11Mention of a trade name, proprietary product, or specific equipment does not constitute a guarantee by the United States Department of Agriculture and does not imply its approval to the exclusion of other products that may be suitable. *Free Radic Biol Med* **27**, 612–616 (1999).

90. Halliwell, B. & Whiteman, M. Measuring reactive species and oxidative damage *in vivo* and in cell culture: how should you do it and what do the results mean? *Br J Pharmacol* **142**, 231–255 (2004).

91. Keston, A. S. & Brandt, R. The fluorometric analysis of ultramicro quantities of hydrogen peroxide. *Anal Biochem* **11**, 1–5 (1965).

92. Tarpey, M. M., Wink, D. A. & Grisham, M. B. Methods for detection of reactive metabolites of oxygen and nitrogen: in vitro and in vivo considerations. *American Journal of Physiology-Regulatory, Integrative and Comparative Physiology* **286**, R431–R444 (2004).

93. Myhre, O., Andersen, J. M., Aarnes, H. & Fonnum, F. Evaluation of the probes 2',7'-dichlorofluorescin diacetate, luminol, and lucigenin as indicators of reactive species formation. *Biochem Pharmacol* **65**, 1575–1582 (2003).

94. LeBel, C. P., Ischiropoulos, H. & Bondy, S. C. Evaluation of the probe 2',7'-dichlorofluorescin as an indicator of reactive oxygen species formation and oxidative stress. *Chem Res Toxicol* **5**, 227–231 (1992).

95. Qin, Y., Lu, M. & Gong, X. Dihydrorhodamine 123 is superior to 2,7-dichlorodihydrofluorescein diacetate and dihydrorhodamine 6G in detecting intracellular hydrogen peroxide in tumor cells. *Cell Biol Int* **32**, 224–228 (2008).

96. Pauson, P. L. Tropones and Tropolones. *Chem Rev* **55**, 9–136 (1955).

97. Zhao, J. & Liu, X. Electron microscopic methods (TEM, SEM and energy dispersal spectroscopy). in *Reference Module in Earth Systems and Environmental Sciences* (Elsevier, 2022).

98. Singh, M. *et al.* Complete Genome Sequence of the Drug-Naive Classical Staphylococcus aureus Strain FDA209P. *Genome Announc* **3**, (2015).

99. Wang, J. D. & Levin, P. A. Metabolism, cell growth and the bacterial cell cycle. *Nat Rev Microbiol* **7**, 822–827 (2009).

100. Gerdes, K., Møller-Jensen, J., Ebersbach, G., Kruse, T. & Nordström, K. Bacterial Mitotic Machineries. *Cell* **116**, 359–366 (2004).

101. Silber, N., Matos de Opitz, C. L., Mayer, C. & Sass, P. Cell division protein FtsZ: from structure and mechanism to antibiotic target. *Future Microbiol* **15**, 801–831 (2020).

102. Eswara, P. J. *et al.* An essential Staphylococcus aureus cell division protein directly regulates FtsZ dynamics. *Elife* **7**, (2018).

103. Schumacher, M. A., Ohashi, T., Corbin, L. & Erickson, H. P. High-resolution crystal structures of *Escherichia coli* FtsZ bound to GDP and GTP. *Acta Crystallogr F Struct Biol Commun* **76**, 94–102 (2020).

104. Bisson-Filho, A. W. *et al.* Treadmilling by FtsZ filaments drives peptidoglycan synthesis and bacterial cell division. *Science (1979)* **355**, 739–743 (2017).

105. Lock, R. L. & Harry, E. J. Cell-division inhibitors: new insights for future antibiotics. *Nat Rev Drug Discov* **7**, 324–338 (2008).

106. Han, H. *et al.* Recent progress of bacterial FtsZ inhibitors with a focus on peptides. *FEBS J* **288**, 1091–1106 (2021).

107. Kusuma, K. D., Payne, M., Ung, A. T., Bottomley, A. L. & Harry, E. J. FtsZ as an Antibacterial Target: Status and Guidelines for Progressing This Avenue. *ACS Infect Dis* **5**, 1279–1294 (2019).

108. Haeusser, D. P. *et al.* The Kil Peptide of Bacteriophage λ Blocks Escherichia coli Cytokinesis via ZipA-Dependent Inhibition of FtsZ Assembly. *PLoS Genet* **10**, e1004217 (2014).

109. Greer, H. The kil gene of bacteriophage lambda. *Virology* **66**, 589–604 (1975).

110. Conter, A., Bouché, J. P. & Dassain, M. Identification of a new inhibitor of essential division gene ftsZ as the kil gene of defective prophage Rac. *J Bacteriol* **178**, 5100–5104 (1996).

111. Waggoner, B. T., Sultana, K., Symondsa, N., Karlok, M. A. & Pato, M. L. Identification of the bacteriophage Mu kil gene. *Virology* **173**, 378–389 (1989).

112. de Boer, P. A., Crossley, R. E. & Rothfield, L. I. Central role for the Escherichia coli minC gene product in two different cell division-inhibition systems. *Proceedings of the National Academy of Sciences* **87**, 1129–1133 (1990).

113. Masuda, H., Awano, N. & Inouye, M. *ydfD* encodes a novel lytic protein in *Escherichia coli*. *FEMS Microbiol Lett* **363**, fnw039 (2016).

114. Jumper, J. *et al.* Highly accurate protein structure prediction with AlphaFold. *Nature* **596**, 583–589 (2021).

115. Varadi, M. *et al.* AlphaFold Protein Structure Database: massively expanding the structural coverage of protein-sequence space with high-accuracy models. *Nucleic Acids Res* **50**, D439–D444 (2022).

116. Wang, L. *et al.* Filamentation initiated by Cas2 and its association with the acquisition process in cells. *Int J Oral Sci* **11**, 29 (2019).

117. Haeusser, D. P. *et al.* The Kil Peptide of Bacteriophage λ Blocks Escherichia coli Cytokinesis via ZipA-Dependent Inhibition of FtsZ Assembly. *PLoS Genet* **10**, e1004217 (2014).

118. Bajar, B., Wang, E., Zhang, S., Lin, M. & Chu, J. A Guide to Fluorescent Protein FRET Pairs. *Sensors* **16**, 1488 (2016).

119. Felber, L. M. *et al.* Evaluation of the CFP-substrate-YFP system for protease studies: advantages and limitations. *Biotechniques* **36**, 878–885 (2004).

120. Sekar, R. B. & Periasamy, A. Fluorescence resonance energy transfer (FRET) microscopy imaging of live cell protein localizations. *J Cell Biol* **160**, 629–633 (2003).

121. Bisson-Filho, A. W. *et al.* Treadmilling by FtsZ filaments drives peptidoglycan synthesis and bacterial cell division. *Science (1979)* **355**, 739–743 (2017).

122. Gu, H. *et al.* How Escherichia coli lands and forms cell clusters on a surface: a new role of surface topography. *Sci Rep* **6**, 29516 (2016).

123. Pal, R. Phase modulation nanoscopy: a simple approach to enhanced optical resolution. *Faraday Discuss* **177**, 507–515 (2015).